Cenozoic climate changes: A review based on time series analysis of marine benthic δ^{18}O records

Manfred Mudelsee,[1,2] Torsten Bickert,[3] Caroline H. Lear,[4] and Gerrit Lohmann[1]

T. Bickert, MARUM – Center for Marine Environmental Sciences, University of Bremen, PO Box 330 440, 28359 Bremen, Germany.

C. H. Lear, School of Earth and Ocean Sciences, Cardiff University, Main Building, Park Place, Cardiff CF10 3YE, UK.

G. Lohmann, Alfred Wegener Institute Helmholtz Centre for Polar and Marine Research, Bussestrasse 24, 27570 Bremerhaven, Germany.

M. Mudelsee, Alfred Wegener Institute Helmholtz Centre for Polar and Marine Research, Bussestrasse 24, 27570 Bremerhaven, Germany; and Climate Risk Analysis, Kreuzstraße 27, Heckenbeck, 37581 Bad Gandersheim, Germany. (mudelsee@climate-risk-analysis.com)

[1]Alfred Wegener Institute Helmholtz
Centre for Polar and Marine Research,
Bremerhaven, Germany.

This article has been accepted for publication and undergone full peer review but has not been through the copyediting, typesetting, pagination and proofreading process, which may lead to differences between this version and the Version of Record. Please cite this article as doi: 10.1002/2013RG000440

The climate during the Cenozoic era changed in several steps from ice-free poles and warm conditions to ice-covered poles and cold conditions. Since the 1950s, a body of information on ice-volume and temperature changes has been built up predominantly on the basis of measurements of the oxygen isotopic composition of shells of benthic foraminifera collected from marine sediment cores. The statistical methodology of time series analysis has also evolved, allowing more information to be extracted from these records. Here we provide a comprehensive view of Cenozoic climate evolution by means of a coherent and systematic application of time-series analytical tools to each record from a compilation spanning the interval from 4 to 61 Myr ago. We quantitatively describe several prominent features of the oxygen isotope record, taking into account the various sources of uncertainty (including measurement, proxy noise, and dating errors). The estimated transition times and amplitudes allow us to assess causal climatological–tectonic influences on the

[2]Climate Risk Analysis, Heckenbeck, Bad Gandersheim, Germany.

[3]MARUM – Center for Marine Environmental Sciences, University of Bremen, Bremen, Germany.

[4]School of Earth and Ocean Sciences, Cardiff University, Cardiff, UK.

following known features of the Cenozoic oxygen isotopic record: Paleocene–Eocene Thermal Maximum, Eocene–Oligocene Transition, Oligocene–Miocene Boundary, and the Middle Miocene Climate Optimum. We further describe and causally interpret the following features: Paleocene–Eocene warming trend; the two-step, long-term Eocene cooling; and the changes within the most recent interval (Miocene–Pliocene). We review the scope and methods of constructing Cenozoic stacks of benthic oxygen isotope records and present two new latitudinal stacks, which capture besides global ice volume also bottom-water temperatures at low (less than 30°) and high latitudes. This review concludes with an identification of future directions for data collection, statistical method development, and climate modeling.

1. Introduction

Although life changed dramatically at the end of the Cretaceous period/Mesozoic era [*Stanley*, 1989] around 65 Myr ago [*Gradstein et al.*, 2004], global climate during the beginning of the Cenozoic era continued in the warm mode that had persisted before [*Press and Siever*, 1986]. The early Cenozoic was characterized by higher global temperatures than today, smaller temperature gradients between low and high latitudes, an almost complete absence of continental ice, and levels of atmospheric carbon dioxide concentration perhaps as high as 1500 parts per million by volume (ppmv) [*Zachos et al.*, 2001a, and references therein]. Since then the variables describing the Earth's atmosphere, that is, the climate system in its original sense, and also those describing the hydrosphere and the cryosphere, experienced substantial changes. The long-term climate change during the Cenozoic corresponds at first order to a cooling, which drove Earth from a state without ice caps to one with two poles glaciated [*Fischer*, 1981].

To a second, more detailed order the overall Cenozoic climate trend can be considered as a succession of smaller changes: more gradual transitions, such as the cooling during the Eocene epoch [*Broecker*, 1995; *Seibold and Berger*, 1996], which is roughly the interval [34 Ma; 56 Ma] [*Gradstein et al.*, 2004], and more abrupt, event-like changes, such as the Eocene–Oligocene Transition (EOT) [*Miller et al.*, 1987, 1991], roughly 34 Myr ago. This succession of long- and short-term climate transitions was not a monotonic series of cooling; warming also occurred [*Kennett*, 1982; *Cronin*, 2010].

Achieving a comprehensive understanding of the driving actions and reactions requires an assessment of both long-term causal influences, such as tectonic changes [*Crowley*

and Burke, 1998], and short-term causes, such as changes in atmospheric greenhouse-gas concentrations at the Paleocene/Eocene Thermal Maximum (PETM) event [*DeConto et al.*, 2012], about 56 Myr ago, or at the Miocene/Pliocene boundary, about 5 Myr ago. This is the dynamical approach, which takes the timescales of changes into account. It is the basis for obtaining insight into Cenozoic climate physics, its various processes, and their interactions that led to the recorded climate history.

Quantitative analysis of climate data should take all uncertainties into account in order to obtain results with realistic error bars [*Mudelsee*, 2010] and hence allow more rigorous testing of scientific hypotheses [*Popper*, 1935]. The quantitative statistical approach helps also with testing and comparing paleoclimate model variants [*Saltzman*, 2002; *Schmidt et al.*, 2014], for stimulating new model developments.

Several books or book chapters exist on Cenozoic climate changes. *Kennett* [1982] offers a marine perspective, while *Crowley and North* [1991] focus on the development of computer models of Cenozoic climate. *Broecker* [1995] and *Seibold and Berger* [1996] consider basic ideas and conceptual models. *Crowley and Burke* [1998] deal with the slow, tectonic causal actions, and *Cronin* [2010] gives a recent overview of the various empirical findings. Various review articles are concerned with certain points regarding Cenozoic climate changes, such as sea level and continental margin erosion [*Miller et al.*, 1987], modeling onset of glaciation [*Crowley and North*, 1990], plateau uplift [*Ruddiman and Kutzbach*, 1990; *Ruddiman et al.*, 1997], the "snow gun hypothesis" [*Prentice and Matthews*, 1991], changes in Antarctica [*Ehrmann et al.*, 1992; *Shevenell and Kennett*, 2007] and South America [*Le Roux*, 2012a, b], changes in the Pacific [*Lyle et al.*, 2008],

the carbon cycle [*Zachos et al.*, 2008], and deep-sea temperatures and global ice volume [*Lear et al.*, 2000]. Marine sediment cores represent the climate archive most commonly used in the studies described above, with oxygen isotope measurements being the climate proxy variable predominantly considered, indicating changes in global ice volume and ocean water temperature.

However, there are up to date a limited number of studies that include a rigorous statistical treatment of these data, although the benefits of this approach have long been acknowledged. *Shackleton* [1982, p. 199 therein] demonstrates the "feasibility of gathering a data base for examining climatic variability without [the] usual bias toward the recent" and the considerable timescale uncertainties, which, at the time of writing, were seldom better than 1 Myr. More recently, *Zachos et al.* [2001a] focused on the periodic and anomalous components of variability over the early Cenozoic portion, for which they compiled a large data set, and *Cramer et al.* [2009], concerned with ocean overturning since the late Cretaceous, used an even larger data set and employed advanced statistical bootstrap simulation methods to obtain climate trend estimates with error bars.

It is desirable to have a curve representing global climate over the Cenozoic since this gives orientation and allows records of regional climate to be put into context. It also facilitates comparison with output from conceptual and higher-resolved global climate models [*Crowley and North*, 1990, 1991; *Zhisheng et al.*, 2001; *DeConto and Pollard*, 2003; *Nisancioglu et al.*, 2003], which are constructed to test hypotheses about Cenozoic climate mechanisms. For achieving this objective, stacks of foraminiferal oxygen isotope records were constructed from a multitude of marine sediment cores, with the rationale that

regional temperature variations are attenuated and a global signal, representing global ice volume and temperature, emerges. (In paleoclimatology, a stack is a summary curve made from several individual curves by means of an averaging procedure.) Of particular relevance for stack construction has been usage of shells of benthic dwelling foraminifera [*Miller et al.*, 1987; *Prentice and Matthews*, 1988], although tropical, planktic foraminifera have also been used [*Prentice and Matthews*, 1988]. An important step has been the construction of Zachos et al.'s stack of benthic oxygen isotopes [*Zachos et al.*, 2001a], which is based on data compiled from more than 40 marine drilling sites. This record (Figure 1) shows Cenozoic climate evolution at high precision, owing to the large number of sites. However, due to the uneven spatial and temporal distribution of the individual data, even that stack may not be free of bias [*Zachos et al.*, 2001a, 2008]. A more recent benthic oxygen isotope stack [*Cramer et al.*, 2009] is based on an even larger and more recent data compilation. A principal interpretative challenge arises from the time-dependent mixing of the ice-volume and temperature signals in the oxygen isotope values. This is evidently less problematic for the earlier part of the Cenozoic, prior to about 34 Myr ago, when only small [*Miller et al.*, 1987; *Zachos et al.*, 2001a; *Tripati et al.*, 2008] or no ice sheets are thought to have existed (Figure 1), but it is more problematic for the later part. Attempts [*Lear et al.*, 2000; *Cramer et al.*, 2011] have been made to reconcile both signal contributions by means of other records, such as the Mg/Ca elemental ratio as a proxy for temperature, or sea level as an equivalent for ice volume, but those corrections, currently based on a sparse data set, may introduce considerable new uncertainties.

Another recent line of development regards methods of statistical time series analysis, developed, adapted, and tested by one of us [*Mudelsee*, 2010]. These methods are specifically tailored to meet the analytical needs of climatologists, who are concerned with quantifying climate transitions and constructing composites, and who wish to provide estimation results with realistic error bars. To appreciate the statistical approach, consider the task of quantifying a climate transition. A statistical regression model comprises a trend component ("signal"), corresponding to the "true" climate change, and a noise component, summarizing the unknown influences. For oxygen isotope records, the trend may correspond to a long-term ice-volume change, and the noise may correspond to short-term influences, such as diagenesis, local water temperature fluctuations, measurement error, and so forth. While the statistical approach would correctly extract the trend component, another approach could incorrectly look just on the extreme values and infer a too large climate-transition amplitude. This overestimation would thus result from wrongly interpreting noise effects. In the present review, we employ our methods of climate time series analysis [*Mudelsee*, 2010] and utilize the recent, large data compilation of marine benthic oxygen isotope records [*Cramer et al.*, 2009]. We put our analysis into context with existing results and overviews. This "quantitative re-analysis review" is aimed at advancing the quantitative and causal understanding of Cenozoic climate changes.

Within the database, we distinguish between low and high latitudes to accommodate bottom-water temperature differences contained in benthic foraminiferal oxygen isotope records. In the quantitative analytical approach, we are confronted with various sources of uncertainty (measurement, proxy) and also the "challenging properties" of real-world

paleoclimatic time series: non-normal distributional shape, autocorrelation (also called persistence or serial dependence), and uneven time spacing. We meet these challenges by performing computing-intensive bootstrap simulations [*Mudelsee*, 2010]. We further take into account another uncertainty source, dating errors and uncertain timescales. The bootstrap approach is employed for enhancing two time series procedures. First, with parametric regression we fit change-point models [*Mudelsee*, 2000, 2009] to the records. This yields change-point times and amplitudes of changes with realistic error bars. Such knowledge is indispensible for assessing causes of Cenozoic climate transitions. We compare our transition parameter estimates with those from previous papers. Second, with nonparametric regression [*Mudelsee et al.*, 2012] we smooth the pooled data set to obtain stacks that are not parametrically restricted. The resulting two stacks (low and high latitudes) with uncertainty band are compared with the existing benthic stack [*Zachos et al.*, 2001a, 2008], for which no uncertainty band has been published. We note two caveats. First, although our stacks are based on a larger data set [*Cramer et al.*, 2009] than Zachos et al.'s stack, the uneven spatio-temporal data distribution may introduce bias also in our stacks. Second, our approach of comparing low with high latitudes may yield biased results for time intervals of strong latitudinal dependent evolutionary processes.

The presented work on quantifying transitions and events in Cenozoic climate evolution draws on previously identified features, such as the glaciation at the EOT, or the PETM, but it also suggests features that have to the best of our knowledge not yet been explicitly named and/or quantified in the literature (Figure 1).

In this review we first describe the data material (section 2), thereby heavily relying on the extensive work carried out by the compilers [*Cramer et al.*, 2009]. We list the employed seafloor drilling sites, introduce the notation for oxygen isotopes, and evaluate the precision of the timescales. The time series analysis methods (section 3) comprise the parametric regression models and stack construction via nonparametric regression. This section also explains in two parts the error analytical methods. In section 4, where we discuss the results, we first consider the statistical estimates (section 4.1), going from older to younger epochs. We start in the middle of the Paleocene, at 61 Ma, and end in the Pliocene, at 4 Ma. For older time intervals, the database becomes too sparse to allow meaningful application of the advanced time series methods. For younger time intervals, which include the major part of the Northern Hemisphere Glaciation (NHG), the abundance of material and the achieved temporal resolution of records is a magnitude better than for the [4 Ma; 61 Ma] interval; our quantitative statistical approach has already been applied to the [2 Ma; 4 Ma] interval and used for assessing causal explanations of the NHG [*Mudelsee and Raymo*, 2005]. In section 4.1, for each individual climate transition and event we also compare our own estimation results with previous results from the literature and assess the causal explanations brought forward. Section 4.3 presents the new oxygen isotope stacks. We conclude this review by summarizing the essential results and causal interpretations of the Cenozoic climate evolution (section 5). Therein, we further identify future research directions for studying Cenozoic climate changes regarding the sampling of data, the adaptation of statistical analytical tools, and the formulation of climate models.

2. Data

Scientific drilling into the ocean floor [*Deep Sea Drilling Project*, 1969–1986; *Ocean Drilling Program*, 1986–2004, 1988–2007; *Integrated Ocean Drilling Program*, 2005ff., see also the publications from the successor International Ocean Discovery Program] has over the past four decades led to an impressive climate archive of marine sediment cores. *Cramer et al.* [2009] tapped this archive to produce a large database (34,479 data entries) of Cenozoic δ^{18}O records. In this review, we employ their database, perform some initial data checks, and select the records suitable for our purpose of time series analysis.

The checks and preliminary modifications of the database [*Cramer et al.*, 2009, auxiliary material 2008pa001683-ds01.txt therein] consist in removing missing values (time given but not δ^{18}O), testing for strictly monotonically increasing time values (per record), and averaging δ^{18}O values for which identical time values exist. Since the statistical time series analysis methods (section 3) are applied on a site-by-site basis for each transition, a certain minimum sampling density is required. On the other hand, it is preferable to maximize the number of records analyzed to achieve a fuller spatial (global) coverage. Table 1 shows our database for the low latitudes, and Table 2 for the high latitudes. We solved this dilemma problem by setting the minimum sample size per record to 17.

These data sets accompany this review as auxiliary material for helping the readers who wish to replicate the results.

2.1. Seafloor Drilling Sites

The employed low-latitude sites amount to 16, they cover the oceanic area reasonably well; the high-latitude sites amount to 32, they show a better coverage. The division

between low and high latitudes at 30°N and 30°S is not followed strictly since geographical positions changed during the Cenozoic. For example, the position of ODP Site 1209 moved from south of 30°N during the recorded interval [37.7 Ma; 60.5 Ma] to north of 30°N at present; hence we considered ODP 1209 as indicative of low latitudes. *Cramer et al.* [2009, Figure 1 therein] show the paleogeographic positions of many sites.

2.2. Oxygen Isotopes

Oxygen isotopic composition is usually expressed in delta notation [*Bradley*, 1999]:

$$\delta^{18}\mathrm{O} = 1000‰ \cdot \left(R_{\mathrm{Sample}} - R_{\mathrm{Standard}}\right) / R_{\mathrm{Standard}} \,, \tag{1}$$

where R is the number ratio of ^{18}O to ^{16}O isotopes and the index refers to the sample or a standard; for the employed database, VPDB is the standard material against which the sample is compared. Vital effects can produce δ^{18}O offsets in different foraminiferal genera and species; this was corrected for [*Cramer et al.*, 2009] by adjusting [*Shackleton and Hall*, 1984] isotope values to a common genus (*Cibicidoides*). Diagenetic effects on the δ^{18}O value of shells of benthic foraminifera are thought to be small [*Edgar et al.*, 2013].

2.3. Dating and Timescale Construction

The timescales of the originally published δ^{18}O records used bio- and magnetostratigraphic events identified in the sediment records. Since the assumed age values for those events have been updated over the years, *Cramer et al.* [2009] adjusted the dates by linear interpolation to two currently accepted Cenozoic timescales; in this review we employ their adjustment to the *Gradstein et al.* [2004] timescale. *Cramer et al.* [2009] then readjusted age models for the middle to late Eocene portions, between approximately 40 and

34 Ma, by linear interpolation. It should therefore be kept in mind that agreement of estimated middle to late Eocene transition times among records may be partly due to that readjustment.

On the basis of the adjustments to the common timescale [*Gradstein et al.*, 2004] and the readjustment for the middle to late Eocene, *Cramer et al.* [2011] concluded that the relative precision of dates (i.e., among records) is less than $s_{\mathrm{date}} = 0.1$ Myr. We use that s_{date} value in a conservative approach to including timescale errors in the statistical estimations. The absolute precision of dates (i.e., with respect to true time) may be larger.

All of the analyzed records (Tables 1 and 2) have an average time spacing or resolution of better than 900 kyr; several records have an average resolution of a few tens of kyr. However, none of the records covers the whole interval [4 Ma; 61 Ma]. Many records exhibit large hiatuses, that is, data gaps for which no meaningful statistical analysis can be performed. Tables 1 and 2 give not only the average, but also the maximum time spacing. If the maximum is clearly larger than the average (e.g., for DSDP 525), then this may indicate the presence of larger gaps.

3. Time Series Analysis Methods

Following the convention in the statistical analysis of time series [*Priestley*, 1981; *von Storch and Zwiers*, 1999], we denote the measured values (δ^{18}O) of a record as $x(i)$ and the measured time values (ages) as $t(i)$. The index i runs from 1 to n (sample size), and we denote this measured sample as $\{t(i), x(i)\}_{i=1}^{n}$. From this level of measured values, statistical science [*Priestley*, 1981; *Wasserman*, 2004] distinguishes the level of the process, $\{T(i), X(i)\}_{i=1}^{n}$, that generated the sample. The task of statistical inference is to guess

the properties of the process on basis of the sample. The type of inference employed for this review is regression estimation, where we estimate the trend, that is, the long-term systematic relationship between time, $T(i)$, and climate, $X(i)$. The convention uses the "hat notation" for distinguishing between the true, but unknown trend parameter (e.g., the slope, β_1, in a linear model) and its estimate (slope estimate, $\widehat{\beta}_1$).

First we give the motivation for and the concepts of the regression models we employ to quantify Cenozoic climate trends (section 3.1). Then we explain how we determined the uncertainties (1-σ errors) associated with the estimations (section 3.2), the typical size of the deviation between true value (β_1) and estimate ($\widehat{\beta}_1$). The mathematical algorithms of the presented regression models [*Mudelsee*, 2010] contain more details (e.g., on numerical tools). The uncertainty-determination methods have been tested by means of Monte Carlo experiments [*Mudelsee*, 2010], where one generates many artificial series with known (prescribed) properties and studies how well the estimation method infers what has been prescribed.

Whereas regression models are applied to each of the 48 original, unsmoothed δ^{18}O time series (section 2) separately, the stacking procedure provides synoptic views. We examine both the high and the low latitudes. We detail methods of stack construction (section 3.3) and the determination of the related uncertainties.

Fortran source codes of the implemented statistical algorithms accompany this review and give further details for the readers wishing to replicate the results.

3.1. Regression Models

Trend is a climate property of genuine interest. The linear regression (section 3.1.1) is a simple model. It serves for estimating the rather monotonic climate changes during the interval from 4 to 10 Myr ago. Change-point regressions (sections 3.1.2 and 3.1.3), on the other hand, are able to model transitions of climate such as the Cenozoic glaciation steps.

3.1.1. Linear Regression

The linear regression [*Montgomery and Peck*, 1992; *von Storch and Zwiers*, 1999] employs a straight-line model (Figure 2a),

$$X(i) = X_{\mathrm{lin}}(i) + S \cdot X_{\mathrm{noise}}(i), \tag{2}$$

$$X_{\mathrm{lin}}(i) = \beta_0 + \beta_1 \cdot T(i). \tag{3}$$

The noise component, $X_{\mathrm{noise}}(i)$, is a stationary random process with mean zero and standard deviation unity. Its use is required since data $\{t(i), x(i)\}_{i=1}^{n}$ do not exactly fall on the straight line. The standard deviation, S, scales the noise; it measures the variability (climate, proxy uncertainty, and measurement error) around the trend.

Ordinary least squares (OLS) yields a straightforward estimation of regression parameters. The estimators $\widehat{\beta}_0$ and $\widehat{\beta}_1$ minimize the sum of squares of differences between data and model,

$$SSQ_{\mathrm{lin}}(\beta_0, \beta_1) = \sum_{i=1}^{n} \left[x(i) - x_{\mathrm{lin}}(i)\right]^2, \tag{4}$$

where $x_{\mathrm{lin}}(i)$ is given by $X_{\mathrm{lin}}(i)$ with $t(i)$ plugged in for $T(i)$ ("sample version"). The solutions $\widehat{\beta}_0$ and $\widehat{\beta}_1$ can be found in textbooks [*Montgomery and Peck*, 1992; *von Storch and Zwiers*, 1999; *Mudelsee*, 2010].

3.1.2. Ramp Regression

The ramp regression [*Mudelsee*, 2000] employs a nonlinear model with two change-points (Figure 2b),

$$X(i) = X_{\mathrm{ramp}}(i) + S \cdot X_{\mathrm{noise}}(i), \tag{5}$$

$$X_{\mathrm{ramp}}(i) = \begin{cases} x1 & \text{for } T(i) \le t1, \\ x1 + [T(i) - t1](x2 - x1)/(t2 - t1) & \text{for } t1 < T(i) \le t2, \\ x2 & \text{for } T(i) > t2. \end{cases} \tag{6}$$

This is the most straightforward parametric approach for analyzing climate-change questions such as: when did the transition start (answer: $t2$), when did it end ($t1$), and what was the amplitude of the change ($x2 - x1$)?

An OLS fit criterion minimizes

$$SSQ_{\mathrm{ramp}}(t1, x1, t2, x2) = \sum_{i=1}^{n} \left[x(i) - x_{\mathrm{ramp}}(i)\right]^2, \tag{7}$$

where $x_{\mathrm{ramp}}(i)$ is the sample version of $X_{\mathrm{ramp}}(i)$. If $\widehat{t1}$ and $\widehat{t2}$ were known, then the solutions $\widehat{x1}$ and $\widehat{x2}$ followed directly from analytical minimization of SSQ_{ramp} [*Mudelsee*, 2000]. Since $\widehat{t1}$ and $\widehat{t2}$ are unknown, one uses a brute-force search over all combinations of $\widehat{t1}$ and $\widehat{t2}$ from the set $\{t(i)\}_{i=1}^{n}$ [*Mudelsee*, 2000]; for the data sizes encountered (section 2), such minimization costs are insignificant.

3.1.3. Break Regression

The break regression [*Mudelsee*, 2009] employs a nonlinear model with one change-point (Figure 2c),

$$X(i) = X_{\mathrm{break}}(i) + S \cdot X_{\mathrm{noise}}(i), \tag{8}$$

$$X_{\mathrm{break}}(i) = \begin{cases} x1 + [T(i) - t1](x2 - x1)/(t2 - t1) & \text{for } T(i) \le t2, \\ x2 + [T(i) - t2](x3 - x2)/(t3 - t2) & \text{for } T(i) > t2. \end{cases} \tag{9}$$

An alternative formulation would comprise the four parameters $t2$, $x2$, $\beta_1 = (x2-x1)/(t2-t1)$ and $\beta_2 = (x3-x2)/(t3-t2)$. The break can be useful for describing a change in linear trend at one point $(t2, x2)$, from slope β_1 to β_2.

An OLS fit criterion minimizes

$$SSQ_{\text{break}}(x1, t2, x2, x3) = \sum_{i=1}^{n} \left[x(i) - x_{\text{break}}(i)\right]^2, \tag{10}$$

where $x_{\text{break}}(i)$ is the sample version of $X_{\text{break}}(i)$. Analogous to the ramp: if $\widehat{t2}$ were known, then the solutions $\widehat{x1}$, $\widehat{x2}$, and $\widehat{x3}$ followed directly from analytical minimization [*Mudelsee*, 2009]. One uses a brute-force search over all $\widehat{t2}$ from $\{t(i)\}_{i=1}^{n}$ [*Mudelsee*, 2009].

3.2. Uncertainties I

The nonzero noise component introduces uncertainty to the estimation. For simple forms of the noise component, such as a normal distributional shape and absent autocorrelation, and additionally simple estimation problems, such as the linear regression, the estimation uncertainty can be analytically determined from the curvature of the SSQ function [*Montgomery and Peck*, 1992]. However, climate noise is usually more complex, regarding the shape and also the autocorrelation [*von Storch and Zwiers*, 1999; *Mudelsee*, 2010], and the change-point estimation problems encountered here (ramp, break) are more complex than the linear model. An additional source of uncertainty comes from dating errors (section 2.3). The complexities shift the uncertainty determination toward analytical intractability. This situation requires usage of computational tools of uncertainty estimation, that is, bootstrap resampling, which we explain in section 3.2.1. We also show how to combine a number of estimates with (bootstrap-determined) error bars into a weighted mean to obtain a summary estimate (section 3.2.2).

3.2.1. Bootstrap Resampling

The bootstrap computational approach [*Efron and Tibshirani*, 1993] resamples randomly, with replacement, from the regression residuals,

$$e(i) = x(i) - \widehat{x}_{\mathrm{fit}}(i), \qquad i = 1, \ldots, n. \tag{11}$$

$\widehat{x}_{\mathrm{fit}}(i)$ denotes the fitted regressions: $\widehat{x}_{\mathrm{lin}}(i)$, $\widehat{x}_{\mathrm{ramp}}(i)$, or $\widehat{x}_{\mathrm{break}}(i)$. This random sample is written as $\{e^*(i)\}_{i=1}^{n}$. The resample is formed as

$$x^*(i) = \widehat{x}_{\mathrm{fit}}(i) + e^*(i), \qquad i = 1, \ldots, n. \tag{12}$$

The estimation (linear, ramp, or break) is repeated on the resample, yielding new estimates (e.g., $\widehat{t2}^*$). The procedure resampling–estimation is repeated until $B = 400$ copies (of $\widehat{t2}^*$) are available. The bootstrap standard error is the standard deviation over the B copies; it serves to measure the estimation uncertainty [*Efron and Tibshirani*, 1993].

3.2.1.1. Non-normal Distributions

Not all climate variables follow the theoretically tractable situation of normal shape. Resampling from the data (residuals) preserves the distributional shape in the resample. Using the bootstrap is therefore more robust than assuming a specific distributional shape [*Efron*, 1979].

3.2.1.2. Autocorrelation

No climate variable follows the theoretically simple situation of absent autocorrelation. Instead, climate shows persistence, it "memorizes" past values over a range of timescales [*Gilman et al.*, 1963; *Hasselmann*, 1976; *Briskin and Harrell*, 1980; *Wunsch*, 2003; *Mudelsee*, 2010]. To preserve autocorrelation in the resample requires not resampling point-wise from the residuals but instead doing this differently, for example, block-wise

[*Künsch*, 1989]. The blocks should be long enough to capture the climate variable's persistence time [*Mudelsee*, 2002]; see also section 3.3.1.1. The employed block-length selector [*Mudelsee*, 2010, equation (3.28) therein] considers also the data size, n; more data points allow to use longer blocks.

3.2.2. Weighted Mean

The climate transitions are recorded by a number, m, of benthic δ^{18}O records (section 4). This means that m transition-time estimates are available, for example, $\{\widehat{t2}(j)\}_{j=1}^{m}$. Henceforth in this section 3.2.2, for brevity we omit to write the index j, and we illustrate the concept using $\widehat{t2}$.

Also m bootstrap standard errors, $s_{\widehat{t2}}$, are available. Estimates and standard errors can be accurately combined in a summary estimate, the weighted mean [*Birge*, 1932; *Bevington and Robinson*, 1992],

$$\langle\widehat{t2}\rangle = \left[\sum \widehat{t2}\,/(s_{\widehat{t2}})^2\right] \Big/ \left[\sum 1\,/(s_{\widehat{t2}})^2\right]. \tag{13}$$

The sums are over $j = 1, \ldots, m$.

The internal error of the weighted mean is given by

$$s_{\mathrm{int},\langle\widehat{t2}\rangle} = 1 \Big/ \left[\sum 1\,/(s_{\widehat{t2}})^2\right]^{1/2}. \tag{14}$$

The external error of the weighted mean is given by

$$s_{\mathrm{ext},\langle\widehat{t2}\rangle} = \left\{\sum \left[\left(\widehat{t2} - \langle\widehat{t2}\rangle\right) \Big/ s_{\widehat{t2}}\right]^2\right\}^{1/2} \Big/ \left\{(m-1)\left[\sum 1\,/(s_{\widehat{t2}})^2\right]\right\}^{1/2}. \tag{15}$$

The internal error measures via the average statistical error from the individual bootstrap standard errors. The external error measures via the spread of the individual estimates. A deviation between internal and external errors indicates violated assumptions; a smaller

external error may point to overestimated individual standard errors, and a larger external error may point to hidden systematic influences that are not included in the individual standard errors. We report both internal and external errors and, adopting a conservative approach [*Birge*, 1932], we consider the maximum of both for interpretation of results (section 4).

3.2.2.1. Dating-Errors Effects

Due to dating uncertainties, the timescales of the records are not exact but exhibit a random error component with a standard deviation of $s_{\mathrm{date}} = 0.1$ Myr (section 2.3). This timescale uncertainty is taken into account by means of a correction of the internal/external error values of averaged transition parameters that involve time.

For the change-point times start ($t2$) and end ($t1$) of the ramp model (Figure 2b), the correction (e.g., for $\widehat{t2}$) is via error propagation:

$$s'_{\widehat{t2}} = \left[(s_{\widehat{t2}})^2 + (s_{\mathrm{date}})^2 \right]^{1/2}, \tag{16}$$

where the prime denotes the correction. The corrected individual errors ($s'_{\widehat{t2}}$) enter then the weighted averaging.

The correction is applied also to the midpoint, $(\widehat{t1} + \widehat{t2})/2$, of the ramp (Figure 2b) and the change-point time, $\widehat{t2}$, of the break (Figure 2c). However, it is not applied to the duration, $\widehat{t2} - \widehat{t1}$, of the ramp. This is because one may expect a strong correlation of the dating-errors effects on $\widehat{t1}$ and $\widehat{t2}$: If $\widehat{t2}$ has to be shifted to earlier ages, then also $\widehat{t1}$; and vice versa. (Relative dates are more accurate than absolute dates.)

Amplitude estimates are hardly affected by dating errors (no correction). Regarding estimates of the slope (i.e., amplitude/duration), we assume that the amplitude-error

dominates the slope-error and that dating-error effects via the duration are negligible (no correction).

3.3. Stack Construction

For building the stacks of benthic δ^{18}O across the Cenozoic (4 to 61 Ma), we pool the data points, following various predecessors in stack construction [*Imbrie et al.*, 1984; *Martinson et al.*, 1987; *Zachos et al.*, 2001a; *Lisiecki and Raymo*, 2005]. The pooling is done into two groups, the high latitudes with 32 records (pooled data size, $n = 6360$) and the low latitudes with 16 records ($n = 8706$). The two data pools are analyzed by means of nonparametric regression (section 3.3.1), also denoted as smoothing, which yields the benthic δ^{18}O stacks. The stacks are the deterministic long-term trends, the short-term noise components are smoothed away. Uncertainty bands around the stacks are constructed using a specific adaptation of bootstrap resampling and taking dating errors into account (section 3.3.1.1). An alternative procedure of stack construction, not explored here and, to the best of our knowledge, neither in previous work, would consist in smoothing records individually and then averaging them.

3.3.1. Nonparametric Regression

Instead of identifying the trend component, X_{trend}, with a specific linear (X_{lin}) or change-point function ($X_{\mathrm{ramp}}, X_{\mathrm{break}}$) with parameters to be estimated, the smoothing method estimates the trend at a time point T' by, loosely speaking, averaging the data points $X(i)$ within a neighborhood around T'. (A simple example is the running mean, where the points inside a window are averaged and the window runs along the time axis.) Better estimation properties than of the running mean can be achieved by replacing the

non-smooth weighting window (points inside receive constant, positive weight and points outside zero weight) by a smooth kernel function, K. We base the estimation on the kernel estimator after *Gasser and Müller* [1979, 1984]

$$\widehat{X}_{\text{trend}}(T) = h^{-1} \sum_{i=1}^{n} \left[\int_{s(i-1)}^{s(i)} K\left(\frac{T-y}{h}\right) dy \right] X(i), \tag{17}$$

where K is a parabola (with negative curvature); h is the bandwidth; and the sequence s satisfies $T(i-1) \le s(i-1) \le T(i)$, we take $s(i-1) = [T(i-1) + T(i)]/2$ with $s(0) = 4$ Ma and $s(n) = 61$ Ma.

We further perform the smoothing in an adaptive manner by allowing for time-dependent bandwidth, $h(T)$. This has the advantage that (1) the uneven time spacing and (2) heteroscedasticity or time-dependent variance can be taken into account. For example, a smaller spacing (higher resolution) or a reduced variance of the noise around the trend enables a smaller bandwidth to be used and hence finer details to be resolved. A bandwidth optimized in that manner yields more accurate trend estimates than non-optimized smoothing. Determination of $h(T)$ is done iteratively [*Brockmann et al.*, 1993; *Herrmann*, 1997]: assume variance, calculate trend, estimate variance by means of the regression residuals, re-calculate trend, and so forth. The optimized bandwidths vary between about 0.5 and 2.0 Myr (Figure 3).

3.3.1.1. Uncertainties II

Construction of an uncertainty band around the nonparametric trend estimate is, analogously to parametric estimation (section 3.2), based on the residuals,

$$e(i) = x(i) - \widehat{x}_{\text{trend}}(i), \qquad i = 1, \ldots, n, \tag{18}$$

where $\widehat{x}_{\mathrm{trend}}(i)$ is the fitted nonparametric regression (equation (17)) at time point $T = t(i)$. In the following part of this section we refer to the index $i = 1, \ldots, n$ and the data size, n, in a "record-wise" manner, since estimation of persistence, resampling, and timescale simulation is performed for each record separately.

A simple model of red-noise persistence of climatic fluctuations for discrete time and uneven spacing is the AR(1) process, $X_{\mathrm{noise}}(i) = \exp\{-[T(i) - T(i-1)]/\tau\} \cdot X_{\mathrm{noise}}(i-1)$ plus a random innovation. The persistence time, τ, can be estimated from data by numerical minimization of a least-squares cost function [*Mudelsee*, 2002]. For each record, the persistence model is fitted to the kernel regression residuals. The resulting persistence-time values (Table 3) are in the order of a few kyr to a few tens of kyr. Climatological interpretation is deferred to section 4.2. We note that for uncertainty-band construction the bootstrap resampling adopts a persistence time of $\tau = 41$ kyr because Cenozoic climate noise may show signs of Milankovitch's obliquity variations, which act on this timescale [*Berger*, 1978]. The value of 41 kyr is somewhere on the upper limit of estimates (Table 3). The effective data size is the number of statistically independent data points. It determines the size of the estimation error; the smaller the effective data size, the larger is the estimation error. In the case of AR(1) serial dependence, the effective data size is less than the sample size; the larger the AR(1) persistence time, the smaller is the effective data size [*Mudelsee*, 2010, Chapter 2 therein]. Adopting the upper limit of the persistence time thus means calculating with the lower limit of the effective data size, which leads to error bars on the upper limit. It is therefore unlikely that the error bars and the constructed uncertainty bands are too narrow. We call this approach conservative.

Uncertainty-band construction of stacks uses pooled resamples, $\{t^*(i), x^*(i)\}_{i=1}^n$, on which kernel estimation is repeated. Resampling the oxygen isotope values, that is, generating $x^*(i)$, is done record-wise via a parametric AR(1) persistence model. The algorithm, denoted as autoregressive bootstrap or ARB resampling [*Mudelsee*, 2010, Chapter 3 therein], is built upon the idea to (1) calculate the white-noise residuals, $e(i) - \exp\{-[t(i) - t(i-1)]/\tau\} \cdot e(i-1)$, (2) scale them to variance unity by dividing by $(1 - \exp\{-2[t(i) - t(i-1)]/\tau\})^{1/2}$, (3) resample point-by-point with replacement from the scaled white-noise residuals, and (4) "add the redness" as an inverse of step (1).

Resampling the time values, that is, generating $t^*(i)$, is done record-wise via a simple parametric timescale model. We overtake the reported age error of 0.1 Myr (section 2.3), plug it as standard deviation into a Gaussian (normal) random number generator, and shift by that random amount all time points of a record simultaneously. Different records, and different copies of a record's resample, have independent timescale errors, but one resample of a record has completely dependent timescale errors. This solution, dictated by the absence of more advanced timescale models from, for example, Bayesian methods [*Buck and Millard*, 2004] or frequentist tools used in speleothem dating [*Scholz and Hoffmann*, 2011], is a conservative uncertainty approach since the simultaneous, completely dependent time shift should generate a higher timescale variability for the time points of the pools compared to using less dependent errors from more advanced models.

The procedure of record-wise ARB resampling with timescale errors (Figure 4) and re-estimating the nonparametric kernel regression on the resamples (adopting each time the optimized bandwidths from Figure 3) is repeated until $B = 400$ copies of simulated

nonparametric trends are available. For each of the time points T (discretized over the 4–61 Ma interval with a spacing of 1 kyr), the standard deviation over the B copies is determined. The resulting pointwise, standard error uncertainty band is, owing to the twofold conservative approach taken, very likely not an underestimation of the full uncertainties (measurement, proxy, and dating) influencing the estimation.

4. Results and Discussion

4.1. Cenozoic Climate Transitions and Events

4.1.1. Paleocene–Eocene

Although the Cenozoic witnessed to first order a cooling, the transition from a greenhouse to an icehouse climate, its earliest phase saw a warming trend. This began in the middle of the Paleocene and culminated in the Early Eocene Climatic Optimum (EECO). This climatic warming has been recognized in previous work [*Miller et al.*, 1987; *Shackleton et al.*, 1984; *Kennett and Stott*, 1990]; we call it Paleocene–Eocene Trend (PE-Trend). Superimposed on the PE-Trend were short-term warmings termed hyperthermals [*Zachos et al.*, 2008; *Sexton et al.*, 2011]. The most prominent of those events was the PETM [*Kennett and Stott*, 1991].

4.1.1.1. Climate Transition PE-Trend

Seven records allow quantification of the PE-Trend transition (Figure 5, Table 4). The warming set in ∼57.5 Ma. Within error bars low and high latitudes were coeval. The end was ∼54.5 Ma (low latitudes) and ∼53.5 Ma (high latitudes), but those two estimates do not strongly deviate statistically from each other. The δ^{18}O amplitude was 0.6 to 0.7 ‰, indistinguishable for low and high (southern) latitudes.

The decrease in benthic δ^{18}O should be interpreted as a warming (of bottom waters) since for that time the existing ice volume (and its changes) was negligible. How much did it warm?

We re-estimated the calibration ratio between temperature and δ^{18}O changes from the classic paper by *Epstein et al.* [1953]. We analyzed the laboratory-generated data given in Table 7 of that paper with linear least-squares regression (section 3.1.1) and bootstrap error bars (section 3.2). The result is 4.3 ± 0.1 °C per ‰. In addition to the statistical bootstrap uncertainty, there is systematic uncertainty stemming from violations of (1) the assumed linear form (*Epstein et al.* [1953] adopted a parabolic form and determined a small second-order term) and (2) the actualism that must inevitably be assumed when applying calibration formula to paleoclimatic problems. We therefore conservatively calculate hereinafter the temperatures with a larger uncertainty, 4.3 ± 0.4 °C per ‰. This value accommodates also the ratio of 3.9 °C per ‰, which *Zachos et al.* [2001a] employed for the ice-free ocean (Figure 1), the ratio of 4.5 °C per ‰, which *Barras et al.* [2010] determined on cultured benthic foraminiferal calcite, and the ratio of 4.6 °C per ‰, which *Marchitto et al.* [2014, equations (5) to (7) therein], presented based on core top benthic foraminifera measurements.

Adopting the above calibration transforms the δ^{18}O decrease into a warming of 2.9 ± 0.4 °C. This gradual warming during PE-Trend led to the EECO [*Zachos et al.*, 2001a], the warmest longer phase during the entire Cenozoic. The warming did not change the equator–South Pole bottom-water temperature gradient (no data are available on the equator–North Pole gradient at that time). *Kennett and Stott* [1990] obtained a larger

PE-Trend estimate (∼5 °C warming) on basis of data from ODP 690. The deviation of their result from ours (Table 4) might be ascribed in part to differences in age models used, but it also likely reflects the existence of a hiatus in the ODP 690 record ∼52 Ma, and the scatter of between-records results (larger external errors).

4.1.1.2. Climate Event PETM

Eight benthic δ^{18}O records have high enough temporal resolution to allow us to quantify the PETM (Figure 6, Table 5). We statistically model the PETM as a peak event, consisting of an earlier warming start, which peaked at a certain time, and a cooling trend; the warming and cooling changes need not necessarily have the same amplitude (Figure 6).

The five high-latitude records, four from the Southern Hemisphere (DSDP 525, DSDP 527, ODP 689, and ODP 690) and one from the Northern Hemisphere (ODP 1051), show a remarkable agreement in amplitudes: a warming of 1.21 ± 0.11 ‰ or 5.2 ± 0.7 °C and a cooling of 0.96 ± 0.06 ‰ or 4.1 ± 0.5 °C. They also agree in peak timing (55.76 Ma), although this agreement may be partly due to bringing them onto the common timescale [*Gradstein et al.*, 2004]. The systematic error for each of these estimates is not considerably larger than the statistical error (Table 5). Two of the three low-latitude records (DSDP 577 and ODP 865) agree well with the high-latitude results regarding peak timing; the third low-latitude record (ODP 1209) has a slightly later age estimate for the PETM peak (56.7 Ma). This likely reflects a combination of the lower temporal resolution of the ODP 1209 record (0.24 Myr at around the time of the PETM) and the ODP 1209 age model lacking magnetostratigraphy [*Dutton et al.*, 2005].

On the other hand, the three low-latitude records exhibit on average smaller temperature amplitudes than their high-latitude counterparts (a warming of 0.54 ± 0.17 ‰ or 2.3 ± 0.8 °C followed by a cooling of 0.46 ± 0.12 ‰ or 2.0 ± 0.6 °C). The deviating result from DSDP 577 has little weight due to large estimation uncertainty.

Previous work by others on the timing of the PETM peak refl ects also the preference for certain age models [*Cronin*, 2010]. Published dates include 57.33 Ma [*Kennett and Stott*, 1991] (who, however, acknowledged in their paper that this estimate would be revised) and 54.95 Ma [*Zachos et al.*, 2001a]. A recent chronology [*Westerhold et al.*, 2007], based on countable eccentricity cycles of 405 kyr period in deep-ocean sedimentary records from the Walvis Ridge, suggests a PETM peak timing of either 55.53 or 55.93 Ma (depending on the currently undecided counting solution)—our estimate of 55.76 Ma would perfectly fit into the middle.

Previous work by others on the amplitude of the PETM deep-water temperature signal can be compared with our results (Table 5). *Kennett and Stott* [1991] analyzed the same isotope data (ODP 690) as us and found an amplitude of around 2 ‰ or 8.6 °C, which we think is too high. *Kennett and Stott* [1991] further noted that the cooling amplitude was smaller by ∼1 to 2 °C (equivalent to 0.2 to 0.3 ‰) than the warming amplitude of the PETM, with which we agree. *Zachos et al.* [2001a, 2008] analyzed δ^{18}O records from DSDP 525, DSDP 527, ODP 690, and ODP 865 and found a PETM amplitude of more than 5 °C. *Tripati and Elderfield* [2005] measured via Mg/Ca paleothermometry the bottom-water temperatures across the PETM from Sites DSDP 527, ODP 865, and ODP 1209, using three different foraminifera genera (yielding different estimates). Their finding

of a PETM amplitude of 4 to 5 °C warming agrees with our finding (Table 5) for the high latitudes. They also detected a PETM warming of similar magnitude for the low-latitude site of ODP 865, while we detect via δ^{18}O an amplitude of 0.87 ± 0.25 ‰ or 3.7 ± 1.1 °C—which is very compatible. However, for ODP 1209 we find a PETM warming of only 0.48 ± 0.04 ‰ or 2.1 ± 0.3 °C—which is clearly smaller than 4 to 5 °C. An explanation could be that the lower temporal resolution of the ODP 1209 δ^{18}O record at the PETM (Figure 6) did not sample the extreme PETM values.

Regarding polar temperature amplification, it is mathematically possible to calculate a polar amplification factor of deep-water amplitudes from the statistical results (Table 5). The warming at the beginning of the PETM yields a factor of

$$(1.21 \pm 0.11)/(0.54 \pm 0.17) \approx 2.2 \pm 0.7,$$

and the cooling at the end of the PETM yields a factor of

$$(0.96 \pm 0.06)/(0.46 \pm 0.12) \approx 2.1 \pm 0.6,$$

which is indistinguishable from the factor for the beginning (note that in a conservative approach we have used the larger systematic error bars). This calculation suggests that amplification did occur. However, if the result from ODP 1209 is ignored (because of too low resolution and missed extremes), then there is no evidence for polar deep-water temperature amplification. In addition, the "climatological uncertainties" of the estimated amplification factors are likely larger than the statistical uncertainties since the representativeness of the selected low- and high-latitude records for the respective geographical regions is limited.

The duration of the warming phase of the PETM, and also of its cooling or "recovery" phase, is an important climate-dynamical parameter. Since the duration may be rather short, as we shall see, the PETM parameters amplitude and duration may contain information about fast climate feedbacks and short-term climate sensitivity, which could help to put the current anthropogenically induced greenhouse-gas emissions into a quantitative climatic context [*Sexton et al.*, 2011; *DeConto et al.*, 2012; *PALAEOSENS Project Members*, 2012; *Masson-Delmotte et al.*, 2013; *Zeebe and Zachos*, 2013]. Since different compartments in the climate system are characterized by their specific response timescales, we focus here on previous literature that describes changes in the temperature of the deep ocean.

Our results on the durations of the PETM warming and cooling phases (Table 5) are—rightly—dominated by the high-accuracy estimates from ODP 690 and ODP 1051: the warming was accomplished within 6 ± 3 kyr, and the cooling was accomplished within 25 ± 12 kyr (conservative error bounds). These high-accuracy results are owing to relatively high average temporal resolutions of these records around the PETM (ODP 690, 6.7 kyr; ODP 1051, 3.5 kyr). The next-coarser resolved series (DSDP 527, 15 kyr) still shows relatively short durations of 36 kyr (warming) and 30 kyr (cooling). The short-duration estimates of the initial warming phase, all from high-latitude records, are in agreement with previous estimates, obtained partly on identical records under different timescales and from per-eye inspection [*Kennett and Stott*, 1991; *Zachos et al.*, 2001a, 2008; *Cronin*, 2010]. At face value, our estimate of a short duration of also the second, cooling phase of the PETM seems to disagree with a previous, detailed study [*Röhl et al.*, 2007] on ODP

690 and IODP 1263, finding a duration of the whole PETM of ∼170 kyr. However, the following points may help to reconcile this apparent disagreement.

1. The study by *Röhl et al.* [2007] was based on precession-cycle counting of the Ba elemental records and defining the PETM in the conventional way, via carbon isotopes (δ^{13}C).

2. As *Röhl et al.* [2007, p. 6 therein] noted, the "location of the termination of the recovery phase [called cooling phase by us] is somewhat subjective because of the asymptotic shape of the carbon isotope excursion." Our adopted regression models (section 3.1) do explicitly allow for a termination of the recovery phase of the PETM at a warmer level than before the PETM—which we think is realistic. Recovery to the identical level, if one wishes to adopt such a definition, would have taken longer.

Extraterrestrial ^{3}He-based timescales for the PETM sections in marine sedimentary records [*Farley and Eltgroth*, 2003; *Murphy et al.*, 2010] provide additional information. To study the influence on estimated PETM parameters of the selection of the timescale, we brought the ODP 690 and ODP 1051 δ^{18}O records [*Cramer et al.*, 2009] onto the ^{3}He-based timescales [*Farley and Eltgroth*, 2003] by means of linear interpolation and utilizing the sediment-depth points. The ^{3}He-based timescales are relative to the timing of the PETM peak, hence we studied only durations and amplitudes. The results (not shown) attest to the robustness of estimates from ODP 1051; all entries (Table 5) are only minimally affected. Also both amplitude estimates (warming and cooling) from ODP 690 are robust. On the other hand, the duration estimates from ODP 690 (Table 5) should be interpreted with caution. While the value for the end (cooling phase of the PETM)

changed from 35 ± 16 kyr (Table 5) to 16 ± 11 kyr (^{3}He-based), which is still compatible with the summary estimate of a few tens of kyr duration, the value for the start (warming phase) changed from 14 ± 4 kyr (Table 5) to 33 ± 8 kyr (^{3}He-based). However, still valid are the conclusions that (1) both warming and cooling phases of the PETM were relatively fast (i.e., within a few of tens of kyr) and (2) the amplitude of the warming was larger than that of the cooling.

One may ask whether the warmer PETM recovery temperature is due to the long-term background warming trend (PE-Trend). The δ^{18}O slope of the PE-Trend is (weighted average of the entries in Table 4)

$$(0.67 \pm 0.05 \text{ ‰})/(3.95 \pm 0.50 \text{ Myr}) \approx 0.17 \pm 0.02 \text{ ‰/Myr}.$$

During the full PETM duration of 0.031 ± 0.012 Myr, the PE-Trend would therefore account for merely 0.005 ± 0.002 ‰; adopting a PETM duration of 0.170 Myr [*Röhl et al.*, 2007] would still account for merely 0.03 ‰. This contribution of PE-Trend is insufficient to explain the significantly warmer recovery levels of the PETM, as recorded in the benthic δ^{18}O records.

4.1.2. Eocene

The PE-Trend warming ended ~53.5 to 54.5 Ma (section 4.1.1.1) and culminated in the EECO with the warmest long-term temperatures on land and sea during the Cenozoic [*Huber and Caballero*, 2011; *Hollis et al.*, 2012; *Pross et al.*, 2012]. These warm conditions during the EECO can also be simulated with climate models, that is, this "early Eocene equable climate problem" can be solved [*Huber and Caballero*, 2011]. The EECO ended

and gave way to a long-term (i.e., several Myr long) cooling, long since recognized from deep-sea δ^{18}O records [*Miller et al.*, 1987; *Stott et al.*, 1990].

Our statistical model for this cooling follows *Miller et al.* [1987] and *Tripati et al.* [2005], who noted that it comprises two steps. The earlier step is called Long-Term Eocene Cooling I (LTEC-I) by us, the later step LTEC-II. These steps are separated by the Mid-Eocene Climatic Optimum (MECO) [*Shackleton and Kennett*, 1975; *Bohaty and Zachos*, 2003; *Zachos et al.*, 2008]. Geological evidence, primarily the occurrence of ice-rafted debris (IRD), suggests that the Eocene hosted some degree of sea and land ice [*Ehrmann et al.*, 1992; *Eldrett et al.*, 2007; *St. John*, 2008; *Tripati et al.*, 2008]. The interpretation of the LTEC-I and LTEC II δ^{18}O amplitudes therefore has to take to some degree an ice-volume signal into account, and correction attempts have been made using Mg/Ca paleothermometry [*Lear et al.*, 2000; *Billups and Schrag*, 2003; *Pekar et al.*, 2005; *Creech et al.*, 2010; *Dawber and Tripati*, 2011].

4.1.2.1. Climate Transition LTEC-I

The EECO ended with an increase in benthic δ^{18}O, which has a start that was within error bars synchronous at ~49 Ma for low and high latitudes; this finding is well supported by nine records (Figure 7, Table 6). Because of the synchroneity one may be inclined to speculate about statistically significant ice-volume contributions [*Creech et al.*, 2010] to that δ^{18}O signal. However, the nine records deviate from each other—also within the high latitudes alone—in their duration and the end of the earlier cooling phase, LTEC-I. These deviations suggest therefore that ice-volume signal contributions, if at all statistically significant, must have had a relatively short life, in agreement with a conjecture (a span

of less than or equal to ∼0.5 Myr) by *Creech et al.* [2010]. The long-term LTEC-I δ^{18}O amplitude (of 0.82 ± 0.08 ‰, external error) thus corresponds to a rather pure bottom-water cooling (of 3.5 ± 0.5 °C), in line with previous assessments [*Miller et al.*, 1987; *Zachos et al.*, 2001a; *Billups and Schrag*, 2003]. The equator–pole temperature gradient (deep sea) was unaffected during the LTEC-I transition.

4.1.2.2. Climate Transition LTEC-II

The apparently non-synchronous end of the first cooling phase LTEC-I (section 4.1.2.1) was followed by the MECO, a longer-term "event" within the interval from 39 to 44 Ma. The MECO was geographically rather heterogeneous: some records (e.g., ODP 689 and ODP 748) display a strong δ^{18}O minimum, while other records do not (Figures 7 and 8). (*Bohaty and Zachos* [2003] report warming amplitudes equivalent to 1 ‰ δ^{18}O for a compilation of records: ODP 689, ODP 690, ODP 738, ODP 744, and ODP 748.) *Cronin* [2010, p. 105–106 therein] relates the MECO heterogeneity to heterogeneous changes in calcium-carbonate compensation depth (CCD) and productivity (*van Andel* [1975]; see also more recent quantifications [*Bohaty and Zachos*, 2003; *Coxall et al.*, 2005; *Lyle et al.*, 2005; *Pälike et al.*, 2012]). Information from high-resolution δ^{18}O records on the end of the MECO and the second cooling phase LTEC-II is more sparse (five records) than for LTEC-I. However, it is certain that both cooling phases were long-term, over several Myr [*Ehrmann et al.*, 1992; *Kennett and Stott*, 1990; *Zachos et al.*, 2001a].

It is interesting to note that the δ^{18}O amplitude of the LTEC-II transition was significantly smaller for the low-latitude record ODP 1218, which has 0.35 ‰, than for each of the four high-latitude records (Figure 8, Table 7), which average 0.68 ‰. Although this

is just a single record, ODP 1218 covers the full fit interval rather homogeneously at a high temporal resolution, and this low-latitude record agrees in change-point times excellently with the weighted averages from the four high-latitude records. We thus conclude that ODP 1218 gives rather reliable estimates. Under the assumption of still negligible ice-volume changes [*Zachos et al.*, 2001a], it follows that the LTEC-II transition may have been associated with a changing deep-ocean circulation pattern or latitudinal temperature gradients.

4.1.3. Eocene–Oligocene

After the long-term Eocene cooling phases, which ended ∼38 Ma (LTEC-II, section 4.1.2.2), the global climate system seems to have remained relatively stable for several million years until the EOT. The EOT spans the Eocene–Oligocene boundary at ∼34 Ma and is marked by a rather abrupt transition toward heavier δ^{18}O. This shift is widely interpreted as reflecting the glaciation of Antarctica [*Miller et al.*, 1987, 1991; *Prothero et al.*, 2003]. This interpretation is ultimately supported by direct geological [*Ivany et al.*, 2006] and sedimentological [*Barrera and Huber*, 1991; *Ehrmann et al.*, 1992; *Zachos et al.*, 1992] evidence. With the appearance of significant ice, the partition problem of the δ^{18}O amplitudes (temperature versus ice-volume signal) intensifies. We estimate the EOT glaciation signals on the basis of twelve records and also quantify the "overshoot" behavior at the end of the transition, previously termed the Eocene–Oligocene Glacial Maximum or EOGM [*Zachos et al.*, 1996].

4.1.3.1. Eocene–Oligocene Transition (EOT)

Our estimates for the timing of the EOT start (Figure 9, Table 8) show some agreement (within systematic error bars) between low and high latitudes, with a combined weighted average of 34.04 ± 0.09 Ma. The result from ODP 803, western equatorial Pacific, deviates. Rather than a regional climatological signal, this likely reflects the less-than-optimal statistical conditions (only short coverage of the earlier part of the transition, see Figure 9). The end of the isotope shift is around 33.67 ± 0.03 Ma (combined weighted average from roughly synchronous low and high latitudes).

Our estimates for the duration of the EOT isotope shift (Table 8) are around 0.2 to 0.3 Myr, in excellent agreement with *Coxall et al.* [2005]. (This range is also compatible with a calculation of the duration via $[34.04 \pm 0.09]$ Ma $- [33.67 \pm 0.03]$ Ma $= [0.37 \pm 0.09]$ Myr.) Some systematic uncertainties are apparent. These may stem from the less-than-optimal functional form of the ramp regression model (Figure 9). Some of the series, especially the high-resolution records ODP 744 and ODP 1218, but also others such as DSDP 529, DSDP 574, ODP 689, and ODP 748, show the clear "overshoot" behavior at the EOT end, where δ^{18}O does not remain constant but turns slightly back and recovers at lighter values (indicated by arrows in Figure 9), marking the end of the EOGM [*Zachos et al.*, 1996]. Owing to the unavailability of an objective statistical regression model for the overshoot, the eye may be better at finding the overshoot present in other records. (At least two additional parameters, one for the size, the other for the duration of the overshoot would need to be invoked, making fitting rather difficult. We attempt to quantify the overshoot for the high-resolution record ODP 1218 in a subsequent paragraph.)

The comparison of our time estimates with previous estimates from the literature is more fruitful for the EOT duration than for its start or end timings since the latter reflect also the preference by researchers for adopting a certain geologic timescale. *Barrera and Huber* [1991] see a duration of 0.6 Myr in the benthic δ^{18}O record from ODP 744, which we think (see the individual estimation result in Table 8) is an overestimation, perhaps caused by an influence of the "overshoot." *Zachos et al.* [1996] examine benthic δ^{18}O from ODP 744 and DSDP 522 and find a shorter duration, 0.35 Myr. The ODP 1218 δ^{18}O record, from the eastern equatorial Pacific, provides excellent statistical inference conditions (7 kyr resolution). The EOT in that record has been described as comprising two distinct steps, each of a duration of 0.04 Myr [*Coxall et al.*, 2005; *Coxall and Wilson*, 2011]. Our fitting of two ramps to that record (Table 8) agrees well with their result. Previously, based on records from DSDP 522 and ODP 744, *Zachos et al.* [1996, p. 251 therein] reported that "more than half of the EOT isotope shift occurred over the final 40–50 kyr [from 350 kyr]."—a view that is compatible with a two-step change. *Bohaty et al.* [2012] also identify the two isotope steps in their Southern Ocean δ^{18}O records. One can easily fit two ramps instead of one to a smooth transition (Figure 9).

Coxall et al. [2005] further identified in the same record, ODP 1218, the overshoot behavior associated with the end of the EOGM. This feature was noted also by *Pälike et al.* [2006], who gave a duration of the recovery after the overshoot of 0.4 to 0.8 Myr. We fitted a ramp to the ODP 1218 δ^{18}O record, regression interval from 32.50 to 33.65 Ma, in order to quantify the recovery from the overshoot. It turned out (results not shown), confirming *Pälike et al.* [2006], that the recovery was achieved within 0.5 ± 0.2 Myr, with

an amplitude of $+0.26 \pm 0.04$ ‰ (deglaciation/warming). To summarize the findings on the timing of the EOT: it was a fast transition (0.2 to 0.3 Myr duration); likely in at least two faster steps, as seen in the high-resolution ODP 1218 record; it was centered ∼33.86 Ma (Table 8); and it included at the end an overshoot behavior with a recovery to less glaciated and/or warmer conditions of 0.26 ‰ δ^{18}O amplitude within 0.5 Myr, a phenomenon that is quantified here for the ODP 1218 record, but which likely has a larger regional, even global scale.

In a recent paper, *Westerhold et al.* [2014] developed an astronomically tuned timescale for the middle Eocene to early Oligocene and determined the Eocene–Oligocene boundary to be at 33.89 Ma, which is in close agreement with our EOT midpoint estimate of 33.86 ± 0.04 Ma (Table 8; low and high latitudes, external error).

Our estimates for the benthic δ^{18}O amplitude of the EOT (Table 8) show an excellent agreement between low (0.91 ± 0.06 ‰) and high (0.98 ± 0.07 ‰) latitudes. Averaging all individual values, the overall glaciation/cooling is found to be 0.94 ‰ with a systematic error of 0.05 ‰ and a statistical error of 0.02 ‰. Our estimate for the amplitude is similar whether we assume the isotope shift was achieved in one or in two steps. A subsequent recovery from that "glacial overshoot" seems to be a phenomenon of a large regional, perhaps even global scale.

Previous amplitude estimates, based on (1) analyzing subsets of the same δ^{18}O database as ours (section 2), (2) using the same [*Gradstein et al.*, 2004] or (the earlier papers) slightly other timescales, and (3) quantifying the amplitudes in the curves mostly per eye, are mainly comparable to our results. *Barrera and Huber* [1991] find a glaciation/cooling

of 1.15 ‰ on the ODP 744 record, an almost perfect agreement with our individual estimate (Table 8). In their review paper on the Cenozoic Antarctic cryosphere evolution, *Shevenell and Kennett* [2007] see an overall amplitude of ∼1 ‰. *Billups and Schrag* [2003] examine paired proxies (benthic δ^{18}O and Mg/Ca ratios) on records from ODP 689 and ODP 757, finding no evidence for temperature changes across the EOT and, hence, assessing the δ^{18}O amplitude of ∼1 ‰ as ice-volume related. Only *Tripati et al.* [2005, p. 341 therein] overestimate in our opinion the EOT amplitude when they constitute a benthic δ^{18}O amplitude of "up to" 1.5 ‰. We think this overestimation stems from putting too much emphasis on the extremes (i.e., the warm extremes at the EOT start and the cold extremes at the EOT end) rather than on the mean trend (as the regression does it).

Before turning to the application of Mg/Ca paleothermometry with respect to the EOT, let us consider the simple interpretation of the observed δ^{18}O amplitude as a pure ice-volume signal. First, current Antarctic ice volume corresponds to a sea-level change of 58 m [*Fretwell et al.*, 2013]. For the EOT, there exists an independent estimate of the ice-volume change based on sequence stratigraphy from the coastal area of New Jersey. *Pekar et al.* [2002] found that the apparent sea level during the earliest Oligocene fell by 80 ± 15 m. Since the temporal resolution of such studies is inevitably rather coarse, one has to compare that sea-level amplitude with the EOT amplitude in marine δ^{18}O that was attained following the EOGM in the recovery state. Our best quantitative estimate for this comes from marine record ODP 1218, where the initial (two-step) glaciation with an amplitude of 0.96 ± 0.04 ‰ (Table 8) was followed by a recovery deglaciation amplitude

of 0.26 ± 0.04 ‰. The net amplitude for longer-term ice-volume changes (glaciation of Antarctica) would be 0.70 ± 0.06 ‰. Adopting a relation of 1.1 ‰ per 100 m between changes in δ^{18}O and sea level [*Fairbanks and Matthews*, 1978; *de Boer et al.*, 2012], the net amplitude in oxygen isotopes would correspond to 64 ± 5 m sea-level change, in good agreement with the New Jersey observation. However, the major source of uncertainty in bringing δ^{18}O and ice volume together in this manner is the δ^{18}O–sea-level relation, which *Fairbanks and Matthews* [1978] established for a considerably different climatological–geographical situation, the Pleistocene. Since the assumed relation is violated to some degree when applied to the earliest Oligocene, for example because of the theoretical nonlinear functional form [*Mix and Ruddiman*, 1984], the true error bars would be a little larger, and the "excellent agreement" would be somewhat spurious; "some", "little", "somewhat": model results [*de Boer et al.*, 2012] show that the violation of the assumed actualism is not strong.

From a physics viewpoint, the true δ^{18}O signal stored during ice-buildup on Antarctica should depend on the travel distance of the precipitation (Rayleigh destillation) and the source values [*Oeschger and Langway Jr.*, 1989]. Uncertainties in the knowledge about past travel distances and source regions propagate ultimately into the uncertainty about the signal partitioning (ice volume versus temperature). *Bohaty et al.* [2012] offer a quantitative discussion of the relation between ice volume and δ^{18}O at around the EOT, and *Gasson et al.* [2012] explore the uncertainties in the relationship between temperature, ice volume, and sea level over the past 50 Myr. Compare also the work by *Katz et al.* [2008], *Lear et al.* [2008], and *de Boer et al.* [2012].

In an early study, *Lear et al.* [2000] found no evidence for a decrease (cooling) in the benthic foraminiferal Mg/Ca record from DSDP 522. This surprising result was later reproduced for ODP Sites 689 and 757 [*Billups and Schrag*, 2003], ODP Site 1218 [*Lear et al.*, 2004], IODP Site 1263 [*Peck et al.*, 2010], ODP Site 1090 and IODP Site 1265 [*Pusz et al.*, 2011], and ODP Sites 689 and 748 [*Bohaty et al.*, 2012]. Identification of a secondary carbonate saturation state control on benthic foraminiferal Mg/Ca [*Elderfield et al.*, 2006] has enabled these results to be reconciled with a deep-sea cooling event, as the EOT was also marked by a ∼1 km deepening of the CCD [*Lear et al.*, 2004; *Coxall et al.*, 2005; *Lear et al.*, 2008, 2010; *Peck et al.*, 2010; *Pusz et al.*, 2011; *Bohaty et al.*, 2012]. Regional variations in the CCD deepening likely produced a variable impact on benthic foraminiferal Mg/Ca at different sites. Furthermore, the carbonate saturation state effect on benthic foraminiferal Mg/Ca may be nonlinear, perhaps operating only below a saturation state threshold [*Rosenthal et al.*, 2006]; although see the useful discussion in the paper by *Elderfield et al.* [2006]. The two-step CCD deepening might therefore be expected to produce an offset also in the timing of Mg/Ca signals between sites. Current work using combinations of new calibrations, independent proxies for carbonate saturation state and/or exploiting infaunal benthic foraminifera shows promise in unravelling the temperature and saturation state controls on benthic foraminiferal Mg/Ca records [*Elderfield et al.*, 2010; *Lear et al.*, 2010; *Yu et al.*, 2010]. However, until this secondary control on benthic foraminiferal Mg/Ca ratios is better quantified, it is not advisable to stack multi-site benthic foraminiferal Mg/Ca records from intervals of significant change in carbonate saturation state for quantitative statistical analysis. In the deep-sea realm

the shelf-basin hypothesis implies that this precaution applies to most intervals of major changes in sea level [*Berger and Winterer*, 1974]. However, the CCD deepening at the EOT apparently did not affect the primary Mg/Ca of shallow-dwelling benthic or planktic foraminifera. The planktic foraminiferal Mg/Ca paleothermometry indicates a ∼2 to 3 °C cooling at both low [*Lear et al.*, 2008] and high [*Bohaty et al.*, 2012] latitudes, and suggests that approximately 0.6 ‰ of the overall EOT δ^{18}O shift can be ascribed to increased continental ice volume [*Lear et al.*, 2008; *Bohaty et al.*, 2012]. A shelf record of benthic foraminiferal δ^{18}O and Mg/Ca through an EOT section containing lithologic variations and hiatuses is understandably relatively noisy, yet the long-term shift in the δ^{18}O of seawater calculated from this record is also not inconsistent with this value [*Katz et al.*, 2008]. This estimate of the change in the δ^{18}O of seawater across the EOT is also in good agreement with the results of a transient one-dimensional ice-sheet model [*de Boer et al.*, 2012].

Regarding physical–climatological causal explanations of the EOT glaciation, the timing of the EOT start, determined by us as 34.04 ± 0.09 Ma (Table 8), excludes an external astronomical influence in the form of the Popigai impact in Siberia that occurred 35.7 ± 0.1 Ma [*Bottomley et al.*, 1997]; already those authors had excluded that connection; this finding is robust also against uncertainties in the geologic timescale. We rather prefer declining levels of atmospheric CO_2 [*DeConto and Pollard*, 2003; *Pagani et al.*, 2011; *Egan et al.*, 2013] or the tectonic explanation via the opening of the Drake Passage and the Tasmanian Seaway and their impacts on Southern Ocean circulation, the thermal isolation of Antarctica, and various feedback links (e.g., ice–albedo). This explanation

that has chiefly been elaborated by James P. Kennett and his co-workers in a number of papers, see *Kennett and Exon* [2004] and references cited therein; see also *Sijp et al.* [2009] for a climate-model analysis of the role of these forcing factors.

A model study using a fully coupled atmosphere–ocean–ice model is lacking up to date. By parameterizing the ocean heat transport in a coupled atmosphere–ice model, *DeConto and Pollard* [2003] concluded that the role of the Drake Passage is rather minor compared to greenhouse-gas levels in conjunction with the Earth's orbital parameters. A continental ice sheet can only be established if the orbital parameters favor cool austral summers. However, once the atmospheric CO_2 declines further, the Antarctic ice sheet becomes almost insensitive to the orbital forcing. *Cristini et al.* [2012] presented a model sensitivity study aimed to understand if and how the opening of the Drake Passage served as a forcing factor for the Antarctic climate transition. A reduced southward heat flux and a decrease of both water and air temperature is found around and over Antarctica when the Drake Passage is open. A more massive ice sheet develops on the continent, in this case compared to the model configuration with closed Drake Passage. More recently, *Wilson et al.* [2013] suggested the possibility of substantial ice in the Antarctic interior before the Eocene–Oligocene boundary. As pointed out by these authors, the EOT glaciation likely depends on the distribution of the bedrock topography. Several long-term processes of landscape evolution, including glacial erosion, thermal subsidence, and tectonics, have likely lowered the topography in the West Antarctic region considerably, with Antarctic land area having decreased by approximately 20 percent. The ice-sheet model, on which these reconstructions are based, shows (1) that the West Antarctic Ice Sheet first formed

at around the EOT in concert with the continental-scale expansion of the East Antarctic Ice Sheet and (2) that the total volume of East and West Antarctic ice (33.4 to 35.9 million cubic kilometers) was more than 1.4 times greater than previously assumed.

4.1.4. Oligocene

Although the Oligocene seems to have had a relatively stable climate between the two glaciation steps EOT (section 4.1.3.1) and Oligocene–Miocene Boundary or OMB (section 4.1.5.1), we detect and quantify some statistically significant oscillations in benthic δ^{18}O records (O-Swings).

4.1.4.1. O-Swings

The early part of the Oligocene swings started with a significant δ^{18}O decrease (Figure 10, Table 9). The high latitudes (DSDP 522, ODP 689, ODP 744, and ODP 748) exhibit a stronger deglaciation/warming slope ($\sim$0.46 ‰ Myr^{-1}) than the one low-latitude record ODP 1218 ($\sim$0.23 ‰ Myr^{-1}), and that trend seems to have persisted longer for the high latitudes, up to $\sim$32 Ma. After that time the slopes stayed for a period at around zero, for low as well as high latitudes (Table 9).

Previous studies based on marine benthic δ^{18}O [*Miller et al.*, 1987; *Barrera and Huber*, 1991; *Ehrmann et al.*, 1992; *Zachos et al.*, 2001a; *Lyle et al.*, 2008] have also found evidence for a relatively stable Oligocene climate, on Antarctica and also likely on a global scale. Previous studies based on Mg/Ca [*Billups and Schrag*, 2003; *Lear et al.*, 2004] indicate for some locations that variations in temperature of deep waters (and their feeding surface sources) did exist but were not large.

The later part of the initial Oligocene swing brought a slight glaciation/cooling before ~27 to 28 Ma and a slight deglaciation/warming thereafter (Figure 10, Table 10). The associated δ^{18}O slopes are small and seem not to deviate strongly between the six low-latitude sites and the seven high-latitude sites. *Zachos et al.* [2001a, p. 688 therein] had previously noted "a warming trend [that] reduced the extent of Antarctic ice" after 26 to 27 Ma.

An estimation of temperature versus ice-volume changes across the Oligocene swings on the basis of quantified amplitudes would likely be rather inaccurate due to the small signal sizes and also the paucity of records (especially from low latitudes during the earlier part). However, the swings were to a considerable degree in concert (Tables 9 and 10), consistent with some contribution from fluctuating ice volumes [*Lear et al.*, 2004]. These fluctuations likely affected the sheet established during the previous EOT on the Antarctic continent, although they were certainly too small for a complete melting. Possibly, also some parts of a minor ice sheet in the Northern Hemisphere grew and fluctuated, as there exists IRD evidence for that space–time point [*Tripati et al.*, 2008].

The timescale of fluctuations analyzed here for the swings of Oligocene climate are relatively long-term (several Myr). Short-term fluctuations (i.e., on timescales shorter than several Myr), of periods 405 kyr and 1.2 Myr, were identified in the high-resolution record from ODP 1218 [*Pälike et al.*, 2006] and related to Earth's orbital variations in eccentricity and obliquity, respectively. This short-term "heartbeat" of Oligocene climate was superimposed on the long-term swings we describe here. The availability of further

high-resolution records would allow an improved understanding of the interplay of these variations of different timescales.

4.1.5. Oligocene–Miocene

The first major Cenozoic glaciation step was the EOT at the end of the Eocene, which we discussed in a preceding part of this review (section 4.1.3.1). The second major glaciation event was the OMB at the end of the Oligocene. *Miller et al.* [1991, Table 4 therein] defined an "Mi-1 event" in the benthic δ^{18}O record DSDP 522 as the heavy excursion at 56.93 m core depth—a value also we find as the end of the OMB (with an age estimate of 23.25 Ma) using statistical regression techniques (Table 11). While *Miller et al.* [1991] considered further Mi-events of glaciation in sedimentary series, our focus here is to quantify the OMB transition in many records from geographically distributed sites in order to assess its spatial extent and climatological relevance.

4.1.5.1. Oligocene–Miocene Boundary (OMB)

There are six δ^{18}O records from the low latitudes, three of which (ODP 926, ODP 929, and ODP 1218) have sufficiently high temporal resolution to allow a rather accurate estimation of the timing of the OMB change. It started at 23.24 ± 0.05 Ma (conservative error bound) and ended at 22.95 ± 0.06 Ma (Figure 11, Table 11).

Nine δ^{18}O records from the high latitudes, although comprising just one high-resolution time series (ODP 1090), still render accurate timing estimates. At high latitudes, OMB started at 23.63 ± 0.14 Ma and ended at 23.27 ± 0.10 Ma.

Owing to the rather large number of sites contributing to the estimations and the small systematic errors, one may conclude on basis of this statistical evidence that the OMB

change at high latitudes started earlier, and also ended earlier, than the change at low latitudes. *Miller et al.* [1991], to whom were available just two coarsely resolved time series, estimated a duration of ∼1 Myr, which is clearly longer than our estimate of ∼0.2 to 0.3 Myr (Table 11). Our estimate is corroborated by the review paper of *Shevenell and Kennett* [2007], who noted a duration of 0.2 Myr.

The validity of the conclusions of whether climate transitions at low and high latitudes were (within error bars) synchronous or not depends on the assumed value of the timescale uncertainty, s_{date}. We carried out a sensitivity experiment to study the effects of increasing s_{date} from 0.1 Myr [*Cramer et al.*, 2011], which is already a conservative (large) choice. Adopting $s_{\mathrm{date}} = 0.2$ Myr led to an OMB start of 23.24 ± 0.09 Ma (conservative error bounds) for the low latitudes and 23.64 ± 0.10 Ma for the high latitudes: still significantly different. Also the conclusion that the OMB end was earlier for low than for high latitudes was found to be robust against increasing s_{date} to 0.2 Myr. Adopting an even larger timescale uncertainty, $s_{\mathrm{date}} = 0.5$ Myr, still allowed to conclude that the OMB started earlier for low than for high latitudes. However, the OMB end estimates with error bars do, for this large s_{date} value, overlap considerably (low latitudes, 22.96 ± 0.21 Ma; high latitudes, 23.29 ± 0.17 Ma). Finally, adopting $s_{\mathrm{date}} = 0.9$ Myr produced large overlaps and let the asynchronism become insignificant. It is difficult to reject the hypothesis that at around the OMB the timescale uncertainty is as large as 0.9 Myr since ultimately the timescale accuracy for each individual record depends on the dating quality of the age control points, their identifiability in the records, and their temporal resolution. On the other hand, ODP 703 (low resolution) and ODP 744 (deviation from the ramp form) do

not offer optimal statistical conditions for estimating the OMB timing (Figure 11), and one may omit these values from the weighted averaging (Table 11); then the apparent asynchronism becomes almost insignificant and smaller timescale errors than 0.9 Myr can explain this. To conclude, the finding of an insignificant asynchronism is compatible with the simple explanation of an ice-volume dominated signal.

The estimated duration of the OMB transition is with ∼0.2 to 0.3 Myr about the same as that of the EOT glaciation (section 4.1.3.1). And also the OMB transition leaves in the large majority of the analyzed records the imprint of an overshoot behavior followed by a recovery (indicated by arrows in Figure 11)—back to nearly as "warm" conditions as before the transition. This similarity between the EOT glaciation and the OMB transition in quantitative timing parameter values and also the shape of the typical course over time, points at a dynamical similarity: also OMB may reflect a glaciation.

The low- and high-latitude OMB records disply a remarkably close similarity in their amplitudes (Table 11). The combined overall weighted mean from the fifteen records is a cooling/glaciation amplitude of 0.60 ‰, with a systematic error of 0.03 ‰ and a statistical error of 0.02 ‰. (We think that *Miller et al.* [1991] as well as *Shevenell and Kennett* [2007] overestimated the δ^{18}O amplitude; both of them give a value of ∼1.0 ‰. This overestimation stems from employing too few records and/or putting too much emphasis on the extremes.)

The close similarity between low and high latitudes in the δ^{18}O amplitude (an increase of 0.60±0.03 ‰ across the OMB) suggests a more global signal origin: ice-volume changes, in line with previous assessments [*Miller et al.*, 1991; *Shevenell and Kennett*, 2007]. How-

ever, the temperature signal cannot be neglected: *Billups and Schrag* [2002] made Mg/Ca paleothermometry on the low-resolution, benthic record ODP 747 and found [*Billups and Schrag*, 2002, Figure 6 therein] a cooling of ∼1 °C. *Lear et al.* [2004, p. 6 therein] applied the Mg/Ca method to high-resolution benthic ODP 1218 data, finding evidence for bottom-water cooling–warming cycles of ∼2 °C amplitude, cycles that occurred before and around the OMB. Furthermore, *Mawbey and Lear* [2013] document an orbital component in the deep-water temperature history at Ceara Rise sites ODP 926 and ODP 929, with amplitudes in the order of 2 °C. Interestingly, there may exist a time lag between temperature and ice-volume changes. *Shevenell and Kennett* [2007, p. 2318 therein] noted that "cooling of deep-ocean waters may have played a role in triggering Mi-1."

A temperature signal of 1.5 ± 0.5 °C or 0.35 ± 0.12 ‰ δ^{18}O implies a lower limit for the ice-volume related δ^{18}O amplitude of 0.25 ± 0.12 ‰ for the OMB glaciation. This value is less than, but in size comparable to the δ^{18}O amplitude of 0.39 ± 0.04 ‰ associated with the NHG in the late Pliocene [*Mudelsee and Raymo*, 2005], but the geological evidence [*Naish et al.*, 2001] suggests that at least part of the ice was stored on Antarctica. *Shevenell and Kennett* [2007] make the interesting observation that at around the OMB glaciation, the Antarctic ice sheet could have reached the continental shelf, with the resulting consequences of marine-based, fluctuating ice sheets, as described for the Northern Hemisphere in the Pleistocene [*Berger and Jansen*, 1994].

Regarding the causes of the OMB glaciation, note that prior to the glaciation the temperatures of the deep ocean had changed (the lag behavior described in a previous paragraph). Further note the overshoot/recovery behavior, which previous work [*Zachos*

et al., 2001b; *Lear*, 2007] had also described. *Zachos et al.* [2001b, p. 277 therein] use the insightful expression "overshoot of equilibrium." This hints at considering elements of nonlinear dynamical systems theory [*Stanley*, 1971] for explaining abrupt paleoclimatic transitions. Abruptness requires that positive feedback loops set in, which could enhance and accelerate an ongoing transition by orders of magnitude.

In the case of the glaciation of Antarctica (or the Northern Hemisphere), it seems clear that two major, more or less independent atmospheric climate variables have to act together to yield rather fast changes in ice volume [*Prentice and Matthews*, 1991]: temperature (which needs to be low) and moisture (which needs to be high). One or the other variable may take the lead, driven externally by tectonic changes [*Ruddiman et al.*, 1997; *Crowley and Burke*, 1998; *Kennett and Exon*, 2004] or astronomical pacing [*Zachos et al.*, 1997; *Naish et al.*, 2001; *Zachos et al.*, 2001b; *Pälike et al.*, 2006]. The other variable, influenced externally or by local climate noise (other, unknown influences) has to pass a certain threshold, a "material constant" of the paleoclimatic system, to let the abrupt change start. The change itself may then invoke negative feedback loops, which would bring an end at a new, intermediate equilibrium level [*Stanley*, 1971].

4.1.6. Miocene

The OMB transition (section 4.1.5.1) was a strong glaciation, which initiated the Miocene. It was not the only one in that epoch: "Isotope workers generally agree that there was a buildup of the Antarctic ice sheet in the middle Miocene" [*Miller et al.*, 1991, p. 6840 therein], and these authors proposed that there were seven glaciation intervals ("Mi-events") in the early to middle Miocene. However, on a longer timescale,

the Miocene climate trend contains a warming in its early half, which culminated in the climatic optimum (MMCO). *Cronin* [2010] notes that this warm interval was from 18 to 14 Ma. We statistically analyze the timing of this warm interval (finding that is was from ∼17 to 15 Ma) and also the amplitudes of the change-points (start and end) in the middle Miocene climate. The later half of the Miocene brought, on a longer timescale, cooling and glaciation, driving climate away from the relatively warm MMCO.

We ask for attention of usage of words "start" and "end" in these sections on the Miocene. The MMCO-Start transition started and ended, then the MMCO was established. Afterwards, the Middle Miocene Climate Transition (MMCT) [*Flower and Kennett*, 1993a; *Shevenell et al.*, 2004] brought the MMCO to an end.

4.1.6.1. Climate Transition MMCO-Start

The start of the warming toward the MMCO (start of MMCO-Start) was at ∼17.5 Ma; low and high latitudes were coeval within the considerably large error bars (Figure 12, Table 12). The chief reason for the large estimation errors is the large climate variability around the trend, which is in its size even comparable to the δ^{18}O amplitude of ∼0.2 to 0.4 ‰ (Table 12). MMCO-Start was completed by ∼17.0 Ma.

The large climate variability imprinted on the δ^{18}O curves stems partly from the Mi- events of ice-volume fluctuations [*Miller et al.*, 1991] and from deep-water variability [*Wright et al.*, 1992; *Billups and Schrag*, 2002].

4.1.6.2. Middle Miocene Climate Transition (MMCT)

Although eight benthic δ^{18}O time series from the low latitudes and nine series from the high latitudes contribute to the estimation of the timing when the transition from

the warm MMCO to colder conditions started and ended, the statistical results appear somewhat ambiguous (Figure 13, Table 13). The start was at ∼15 Ma or slightly later, and the estimates for low and high latitudes are apart from each other by 0.32 ± 0.26 Myr (conservative error bounds propagated), that is, high latitudes started earlier. The end was clearly earlier (∼14 Ma) for high compared to low latitudes (∼13 Ma). For the other two major glaciation steps, EOT (Table 8) and OMB (Table 11), the high latitudes were either earlier (less likely) or coeval (more likely) with the low for both start and end.

Some of the records documenting the MMCT reflect an almost abrupt δ^{18}O increase (DSDP 317, DSDP 366, and ODP 667 from the low latitudes; DSDP 281 and DSDP 555 from the high latitudes), while the other, which include some rather highly resolved series (e.g., DSDP 574 or ODP 1171), exhibit a longer-term transition that can be excellently statistically modeled by means of a ramp (Figure 13). The low resolution or the existence of hiatuses at around the MMCT may be responsible for the apparent abruptness at DSDP 317 and DSDP 366, but more data and improved age models are required before the possibility of an abrupt end to the MMCO in some places may be dismissed. For example, *Holbourn et al.* [2005, 2007] construct benthic δ^{18}O records from two low-latitudinal sites (ODP 1146, western Pacific; ODP 1237, eastern Pacific) that are both relatively short but bracket the MMCT at high temporal resolution: these records indicate a rather abrupt glaciation at around 13.9 Ma. Notably, the MMCT does not exhibit an overshoot/recovery signature.

While the seventeen δ^{18}O records display scatter in the timing estimates, they render a rather close agreement in the δ^{18}O amplitude. The overall weighted mean of the entries

(Table 13) is 0.88 ‰ with a systematic error of 0.04 ‰ and a statistical error of 0.02 ‰. This δ^{18}O increase is, within error bars, of the same magnitude as the increase across the EOT (section 4.1.3.1) and of ∼0.3 ‰ larger magnitude than the increase across the OMB (section 4.1.5.1). Already the size of the amplitude, but also the coherency across results (Table 13), point to a strong ice-volume component (glaciation) at the end of the MMCO.

Previous papers vary in their assessment of whether the MMCT was abrupt or not. *Miller et al.* [1987, p. 9 therein] mentioned a "sharp" δ^{18}O increase at ∼15 to 13 Ma, which they interpreted as a reestablishment or intensification of glacial conditions. *Lear et al.* [2000] as well as *Billups and Schrag* [2002] showed plots of Mg/Ca-derived deep-water temperature changes and concluded that a gradual cooling by ∼2 to 3 °C occurred. Using the advanced analytical technique via paired records of Mg/Ca and Li/Ca, indicating temperature and carbonate saturation variations, *Lear et al.* [2010] found a long-term change from 15.3 to 12.5 Ma and estimated an overall cooling of ∼1 °C. In their review paper on Cenozoic climate evolution, *Zachos et al.* [2001a] interpreted previous work with oxygen and carbon isotopes on marine benthic records [*Vincent et al.*, 1985; *Flower and Kennett*, 1995] and also concluded that the cooling was gradual and that a reestablishment of major Antarctic ice sheets occurred across the MMCT. On the other hand, *Shevenell and Kennett* [2007] relied on the work that generated the δ^{18}O record DSDP 281 [*Shackleton and Kennett*, 1975], which exhibits a very fast transition (Figure 13), and, thus, assessed the MMCT as abrupt, of ∼1 ‰ at 14 Ma. The variety of assessments underlines the importance of analyzing a multitude of records from distributed locations (Tables 1 and 2) to be able to distinguish between more regional and more global climate signals.

If we assume that besides Antarctic ice growth across the MMCT there occurred also "global cooling" [*Shevenell and Kennett*, 2007, p. 2319 therein], then we may start an ice-volume estimation on basis of a deep-water cooling of 1.5 ± 0.5 °C; the large error should accommodate for the fact that the cooling amplitude is inferred only from a few coarsely resolved [*Lear et al.*, 2000; *Billups and Schrag*, 2002] and one higher resolved [*Lear et al.*, 2010] time series. The corresponding δ^{18}O signal is 0.35 ± 0.12 ‰, and the ice-volume related δ^{18}O signal from the MMCT is

$$(0.88 \pm 0.04 \text{ ‰}) - (0.35 \pm 0.12 \text{ ‰}) \approx 0.53 \pm 0.13 \text{ ‰}.$$

Thus, the signal proportion of ice volume is

$$1 - (0.35 \pm 0.12)/(0.88 \pm 0.04) \approx 0.60 \pm 0.14.$$

Shevenell and Kennett [2007] assessed "direct" signal-proportion determination (via Mg/Ca) and indirect determination and claimed a value of 80 and 70 percent, respectively. This agrees with our value of 60 ± 14 percent. We recommend using the calculated ice-volume amplitude of 0.53 ± 0.13 ‰ for quantitative testing by means of concepts and models of sea-level changes and the ice-sheet geometry on Antarctica or the Northern Hemisphere [*Saltzman*, 2002].

Cronin [2010] briefly reviewed causal explanations of the end of the MMCO, the cooling, and the ice-sheet growth after the middle of the Miocene. An initial cooling shift could have been caused by an enhanced biological pumping activity of the ocean, which led to atmospheric CO_2 removal into organic sedimentary matter, as is documented by an increase in δ^{13}C [*Holbourn et al.*, 2005, 2007, 2013; *Diester-Haass et al.*, 2009, 2013] and in organic-rich layers in the coastal Monterey Formation, California, and elsewhere [*Vincent*

and Berger, 1985]. Alternatively to this "Monterey hypothesis", CO_2 removal could also have been accomplished by enhanced weathering, for example in the uplifted Himalaya region [*Raymo*, 1994]. Regardless, there is recent evidence for reduced CO_2 during the middle Miocene [*Foster et al.*, 2012; *Badger et al.*, 2013; *Masson-Delmotte et al.*, 2013]. An essential element of the causal chain is Southern Ocean circulation and heat transport [*Flower and Kennett*, 1993a, b, 1994, 1995]. Our result (Table 13) from time series analysis of an earlier start, and an earlier end as well, of the cooling at high latitudes compared to low, may allow the interpretation that polar cooling amplification was also involved.

There is more abundant oxygen isotopic evidence for the MMCT cooling in the Miocene than for previous glaciations, and this evidence suggests that a complex causal network existed, spatially heterogeneous processes and feedback mechanisms acted, and the cooling was not globally homogeneous. Recently, *Knorr and Lohmann* [2014] have used a coupled atmosphere–ocean model to disentangle the effects of CO_2 and Antarctic ice-sheet changes on the characteristic temperature evolution during the MMCT. Ocean circulation changes in response to Antarctic ice-sheet growth can cause a sea-surface warming and concurrent deep-water cooling in large parts of the Southern Ocean. In contrast, longer-term surface and deep-water temperature trends are dominated by CO_2 changes, indicating that the feedbacks with the ice-sheet changes in Antarctica might induce non-heterogeneous trends in temperatures of bottom waters, surface waters, and in other properties (e.g., salinity). These impacts provide a coherent explanation for the Southern Ocean temperature evolution during the Miocene ice-sheet expansion [*Shevenell et al.*, 2008] and suggest that

the climate response and feedbacks to large ice-sheet changes in Antarctica may be more complex than previously thought.

4.1.7. Miocene–Pliocene

The preceding sections analyzed the Miocene down to a bound of ∼10 Ma. We quantified the relatively warm MMCO and, at the end of it ∼13 to 14 Ma, the third major Cenozoic glaciation step (MMCT). Previous own work [*Mudelsee and Raymo*, 2005] had examined the interval from 2 to 4 Ma in order to quantify the fourth glaciation step, the NHG, which started in the Pliocene at ∼3.6 Ma. For the range between 4 and 10 Ma, there is room for further analysis. We identify a longer-term, but minor cooling trend, which we call 4-to-10-Ma.

4.1.7.1. Climate Transition 4-to-10-Ma

There are no discernable, or by means of statistical techniques quantifiable, climate steps within the interval from 4 to 10 Ma (Figure 14). The numerical results show mostly cooling trends (four from five low-latitude and nine from twelve high-latitude records); and the few warming trends detected are statistically not, or hardly (ODP 806), significant (Table 14). The fact that systematic errors are about two to three times larger than the statistical errors indicates spatially heterogeneous slope values. However, no geographical pattern (low versus high latitudes or individual ocean basins) can be identified (Table 14). For example, even within a single region, the Ontong Java Plateau (west equatorial Pacific), the slopes have different signs (cooling at Site DSDP 289 and warming at ODP 806). Regional to even local effects (temperature, other) on the δ^{18}O trends are evident. Spatio-temporal stochastic model fits may lead here to better insight into patterns.

The average slope, calculated over all records from Table 14, is 0.039 ± 0.008 ‰ Myr^{-1}, conservatively the larger (systematic) error bar is given. Over the full 6-Myr span, this means a δ^{18}O change of 0.23 ± 0.05 ‰, a value that can further be tested (e.g., by means of climate models) and possibly split into contributions from changes in ice volume (which should be rather small), in temperature of bottom waters and, hence, the feeding surface waters, and in other properties (e.g., salinity).

Previous work utilizing Mg/Ca-thermometry on deep waters support the conclusion of minor gradual cooling trends in the late Miocene and early Pliocene: *Billups and Schrag* [2002] examined ODP 747 from the Southern Ocean (however, there is a gap between ∼5 and 7.5 Ma in their record), *Lear et al.* [2003] analyzed ODP 806 from the Ontong Java Plateau and ODP 926 from the equatorial Atlantic, and *Billups and Scheiderich* [2010] reviewed (Oligocene to) Miocene paleotemperature trends from foraminiferal Mg/Ca records obtained from six ODP sites. Agreeably, more records analyzed in that manner would help to draw a clearer geographical picture. Decreasing trends in atmospheric CO_2 have been inferred [*Tripati et al.*, 2009] and made responsible for the cooling [*Cerling et al.*, 1997; *Tripati et al.*, 2009].

4.2. Cenozoic Climate Persistence

The persistence time is an important dynamical parameter that quantifies the "memory" or "inertia" of random climate fluctuations. It corresponds in the frequency domain to the redness of a climate spectrum.

From a technological perspective, obtaining the estimates of the AR(1) persistence time τ (Table 3) was a challenge due to the difficult numerical minimizations of the least-

squares cost function [*Mudelsee*, 2002]. For fifteen of the 48 analyzed records, no result could be obtained. These difficulties seem to originate mainly from the relatively coarse resolution (i.e., large average spacing, $\bar{d}$) of those records (Tables 1 and 2), which brings the "equivalent autocorrelation coefficient", $a = \exp(-\bar{d}/\tau)$, close to zero, that means, the lower bound. All high-resolution records (i.e., with $\bar{d} < 100$ kyr), yield meaningful persistence time estimates with small error bars, which dominate the weighted averaging (Table 3).

The white-noise residuals of the fitted AR(1) persistence model [*Mudelsee*, 2010],

$$\epsilon(i) = e(i) - \exp\{-[t(i) - t(i-1)]/\widehat{\tau}\} \cdot e(i-1), \tag{19}$$

attested in lag-1 scatterplots of $\epsilon(i-1)$ versus $\epsilon(i)$ (not shown) graphically that the AR(1) model may be a suitable description. The idea is that in a scatterplot the AR(1) (red noise) data display an orientation along the 1:1 line ("warm yesterday, warm today"), while white-noise data do not display such an orientation and rather look like a cloud [*Mudelsee*, 2010]. Even when considering the large systematic errors (Table 3) it seems that the low-latitude records exhibit a shorter memory ($\widehat{\tau} \approx 4.0$ kyr) than the high-latitude records ($\widehat{\tau} \approx 8.5$ kyr). To give a physical–climatological explanation is difficult. A reduced AR(1) "inertia" of deep-water temperature fluctuations at low latitudes, compared to high latitudes, would have to be derived from climate-theoretical principles of long-term Cenozoic climate evolution. Alternatively, one may interpret the AR(1) parameter by invoking noise-influenced Milankovitch variability under the premise that high-latitude climate fluctuations are more influenced by changes in obliquity (period around 41 kyr [*Berger*, 1978]) and low-latitude fluctuations by changes in precession (periods around 19

kyr [*Berger*, 1978]), but still then the astronomical–climatological link has to be evaluated [*Laepple and Lohmann*, 2009, Figure 7 therein], including the nonlinearities in the system. When neglecting ice-sheet feedbacks, the low-latitude fluctuations are dominated by changes in precession, semi-precession, and eccentricity. Such astronomical–physical–climatological concepts should be tested by means of climate models [*Saltzman*, 2002] and theoretical analyses [*Laepple and Lohmann*, 2009; *Livina et al.*, 2011, 2013].

We further examined, by estimating persistence for time intervals before and after 34 Ma in a pairwise manner, whether the existence of larger ice sheets in the later interval could have influenced the memory of δ^{18}O fluctuations in deep waters. Only four records, all from high latitudes (DSDP 525, ODP 689, ODP 690, and ODP 748), are of high resolution and cover the intervals before and after 34 Ma sufficiently long (Table 2) to be assessed as representative. Persistence time estimation on these records, however, did not give conclusive results; in two cases (ODP 690 and ODP 748) the later interval showed a longer memory (as one would assume from the existing larger ice volumes with larger "time constants" than the temperature of water bodies [*Mudelsee and Raymo*, 2005]); in the two other cases the results were opposite. Also the results on low-latitude records were inconclusive.

The AR(1) is a rather simple model of persistence in the fluctuations around the long-term ($\sim$Myr) climate trend: just the immediate past value is "remembered." An alternative model is that variations (shorter than $\sim$Myr) in the geometry of Earth's orbit are superimposed on the long-term climate trends. Although the arguments brought in favor of such Milankovitch variability are partly based on isotope and other climate proxy

records that had previously been tuned to match the astronomical target, we assess the available evidence [*Fischer*, 1981; *Hilgen et al.*, 1995; *Zachos et al.*, 1996; *Kent*, 1999; *Hinnov*, 2000; *Kashiwaya et al.*, 2001; *Zachos et al.*, 2001a, b; *Abdul Aziz et al.*, 2003; *Coxall et al.*, 2005; *Lourens et al.*, 2005; *Pälike et al.*, 2006; *Röhl et al.*, 2007; *Shevenell and Kennett*, 2007; *Westerhold et al.*, 2007; *Lyle et al.*, 2008; *Sexton et al.*, 2011; *DeConto et al.*, 2012; *Westerhold et al.*, 2014] as convincing enough to consider that indeed Milankovitch variability cannot be ignored even on Cenozoic timescales. The upper bounds of the persistence time estimates (Table 3) are in the order of a few tens of kyr—which seems basically compatible with the result of fitting AR(1) models to noise-influenced Milankovitch time series (eccentricity, obliquity, and precession). Further evidence should be obtainable from spectrum estimation [*Priestley*, 1981; *Percival and Walden*, 1993; *Bendat and Piersol*, 2010; *Mudelsee*, 2010] on the residuals series, $e(i)$. This task is beyond the scope of this "time-domain" review. Researchers embarking on it should consider using spectrum estimation tools that (1) can directly process the unevenly spaced records [*Schulz and Mudelsee*, 2002] and (2) take timescale uncertainties into account [*Mudelsee et al.*, 2009].

4.3. Cenozoic Benthic δ^{18}O Stacks

Figure 15 shows the new stacks (for low and high latitudes) of benthic oxygen isotopic composition together with Zachos et al.'s stack [*Zachos et al.*, 2001a]. For comparing the records one should bear in mind the effects the smoothing bandwidth has on a resulting stack. *Zachos et al.* [2001a] employed a five-point running mean, and their database shows an average spacing of ∼5.2 kyr over the interval [4 Ma; 61 Ma], that is, their

stack was produced with a bandwidth in the order of 26 kyr. On the other hand, the optimized bandwidth employed in our kernel smoothing for the new stacks is clearly larger, roughly between 500 and 1500 kyr (Figure 3). That means, our new stacks use a stronger smoothing and utilize also a larger database than *Zachos et al.* [2001a]. Consequently, one should expect narrower statistical uncertainty bands for our stacks than for Zachos et al.'s stack. In addition to these statistical prerequisites, *Zachos et al.* [2001a, 2008] remarked that portions of their stack may be biased due to the uneven spatial and temporal data distribution.

Considering the "theoretical" shortcomings of Zachos et al.'s stack mentioned in the previous paragraph, visually overlying the three stacks reveals a surprisingly good agreement, over most time intervals, between Zachos et al.'s stack on the one hand, and each of our new stacks on the other (Figure 15). Larger, systematic discrepancies seem to be restricted to the interval from about the end of the EOGM in the early Oligocene (∼31 Ma) to about the start of the MMCO in the middle Miocene (∼17 Ma); this interval is discussed in a subsequent paragraph. The old stack [*Zachos et al.*, 2001a] appears to deviate from the two benthic stacks also regarding short-term excursions, such as the PETM (∼ 55 Ma for Zachos et al.'s stack) or the MECO (∼ 41 Ma). However, this cannot be interpreted as a deviation but rather as an inevitable away-smoothing of those short-term excursions by the large kernel bandwidths in our two new benthic kernel stacks.

Also comparing the low with the high latitudes in the kernel stacks (Figure 15) reveals a rather close agreement. It seems that systematic deviations are restricted to roughly that interval between 17 and 31 Ma. This agreement is remarkable for the earlier part

(Paleocene–Eocene), where the amount of ice is thought to be insignificant: it implies that on longer timescales (∼Myr) the polar bottom-water amplification was weak or even absent. On shorter timescales, at around the PETM, we quantified the amplification factor as somewhere around two (section 4.1.1.2). That means, not only climate sensitivity [*PALAEOSENS Project Members*, 2012], also polar amplification should be evaluated in dependence on the analyzed timescale of the changes.

5. Conclusions and Future Directions

We analyzed a large data compilation of marine benthic δ^{18}O records [*Cramer et al.*, 2009] by means of statistical tools [*Mudelsee*, 2010]. This allowed quantification of Cenozoic climate evolution in terms of ice volume and temperature. We determined the timing and amplitudes of climate transitions and events (Figure 1) with realistic error bars, taking into account the various sources of uncertainty (measurement and proxy noise, dating errors). Even so, the uneven spatio-temporal data distribution may introduce bias in our results, and also our approach of comparing low with high latitudes may yield biased results for time intervals of strong latitudinal dependent evolutionary processes. Therefore the taken uncertainty-analytical approach was conservative, that means, the reported error bars and constructed uncertainty bands are to be seen as upper bounds; it is unlikely that they underestimate the true magnitude of the uncertainty. We further constructed two stacks (for low and high latitudes) of benthic δ^{18}O with error band. This form of "quantitative re-analysis review" is thought to contribute to advancing the quantitative and causal understanding of Cenozoic climate changes.

During the Paleocene–Eocene epochs, a gradual warming (called PE-Trend) occurred, which was punctuated by the PETM warming event ∼55.76 Ma. PE-Trend led to the EECO (∼54 to 49 Ma), the warmest longer phase during the entire Cenozoic.

The Eocene saw a long-term global cooling, which can be separated into two gradual transitions (LTEC-I and LTEC-II), in between of which was the MECO. Low latitude deep water cooled stronger than high (southern) latitude deep water, ice volume had only a minor signal proportion.

The transition from the Eocene to the Oligocene (EOT) was a cooling associated with ice-buildup on Antarctica. This was followed by a partial "recovery" to warmer conditions, an "overshoot" behavior that led to the EOGM.

Subsequent to climate swings comprising warming/deglaciation and cooling/glaciation during the Oligocene (termed "O-Swings"), the OMB at the boundary to the Miocene (∼23 Ma) constituted a second major glaciation step during the Cenozoic.

The warm Mid-Miocene Climatic Optimum (MMCO), estimated as from ∼17 to 15 Ma, ended with the third step of increased ice volume (estimated relative signal proportion 60 ± 14 %). The late Miocene showed a minor longer-term cooling trend.

Regarding causal explanations for the various Cenozoic climate events and transitions, one cannot neglect the changes in atmospheric greenhouse-gas concentrations, which have the potential to act also on short timescales (e.g., the PETM), and one cannot neglect long-term tectonic changes, such as those affecting the Southern Ocean circulation (e.g., the EOT). With significant ice volume arriving on Antarctica, the EOT brought into play another forcing and responding climate variable. This made the interaction of the

relevant climate variables more complex, and it should also have enhanced the geographical differentiation (low and high latitudes). This differentiation may also be responsible for the long-term systematic deviations in the new benthic δ^{18}O stacks between low latitudes (warmer) and high latitudes (colder) during the interval from 17 to 31 Ma. In other time periods, the new stacks do overlap considerably, and they do also agree with a previous, global benthic δ^{18}O stack [*Zachos et al.*, 2001a].

Cenozoic climate transitions may be evaluated also in terms of rate of change (‰ per Myr). In analogy to considering the climate-change rate in the recent past (few decades) and its causal agents [*Solomon et al.*, 2007; *Stocker et al.*, 2013], also the rate of change in the geologic past can be used to shed light on the Earth's climatic situation. The results (Table 15) indicate that the PETM was a strong event, both in its earlier warming and in its later cooling phase. However, the PETM is somewhat different from the other transitions in that it was a rather short-term event. From the other, longer-term transitions, the EOT (-1.874 ‰ Myr^{-1}), followed by the OMB (-1.058 ‰ Myr^{-1}), are the two strongest Cenozoic climate transitions; both of which brought glaciation/cooling. The EOT was also strong in its recovery from the "overshoot" ($+0.520$ ‰ Myr^{-1}). Notably, this recovery was stronger than the other warming transitions (PE-Trend or MMCO-Start). The third glaciation step (MMCT) was significantly weaker than EOT or OMB. These assessments are robust as regards the selection of the geologic timescale: A re-analysis of the PE-Trend rates following *Cande and Kent* [1995] instead of *Gradstein et al.* [2004] resulted in values that are within error bars indistinguishable (results not shown). The agreement for transitions or events that occurred later is likely not worse than for PE-Trend.

Future research may be enhanced along three directions (data, statistics, and models), leading to an increase in the current knowledge about the Cenozoic climate evolution. Crucial from an epistemological viewpoint is that researchers deepen or acquire the ability to integrate all three directions into their arsenal of methods.

5.1. Data

Since it is hard to disagree with the simple statement "more data is better", the task here is rather to identify those dimensions in the data space where invested resources may yield a maximum of new information. Regarding the dimension "time", a look on the results tables quickly informs that the Paleocene and Eocene epochs are clearly less well documented than later epochs. Regarding "geographical space", it appears that currently we have fewer records from low latitudes. Since preservation of the information carriers (shells of foraminifera) depends on the CCD and, thus, the geographical location, it is likely rather difficult to achieve a state with more refined spatial information (e.g., several latitudinal belts). *Cramer et al.* [2009] notably study the role of different ocean basins.

Increasing the accuracy of the timescales of the Cenozoic isotope records (*Cramer et al.* [2011] give for the relative precision, s_{date}, a value of less than 0.1 Myr) is thought to be a major challenge. Absolute age determinations, less dependent on the validity of correctly assumed Milankovitch variations so far back in time, could come from a chronostratigraphic framework that is based also on documented global stratigraphic events (e.g., the deposition of volcanic ashes): a huge and difficult compilation work to be carried out.

Another dimension in the data space is "proxy variable", and δ^{13}C is here a prime candidate for further analysis of changes in ventilation, productivity, and flow of water

masses [*Kroopnick*, 1985; *Zahn et al.*, 1986; *Wright et al.*, 1992; *Sarnthein et al.*, 1994; *Diester-Haass et al.*, 2009, 2013]. The δ^{13}C compilation [*Cramer et al.*, 2009] could be analyzed in a similar manner as in the present paper (for which it would be beyond the scope). Proxy variables for water-temperature changes are clearly required to solve the δ^{18}O partition problem (ice volume and temperature), and we expect future advances from Mg/Ca paleothermometry and also the more recently developed carbonate clumped isotope thermometry [*Eiler*, 2007; *Tripati et al.*, 2010; *Eiler*, 2011].

5.2. Statistical Analysis

As regards parametric statistical time series analysis, the employed simple regression tools (linear, ramp, and break) were found useful for quantifying the observed Cenozoic climate events and transitions. However, for achieving a better quantitative understanding of the "overshoot" behavior (e.g., at around the OMB), it should be useful to develop slightly more complex parametric models, comprising more parameters—and constituting more difficult numerical challenges. It should be kept in mind that it makes sense to fit such advanced models only to time series data of high quality, coverage, and resolution.

As regards nonparametric statistical time series analysis, alternative procedures of stack construction via smoothing records individually before averaging should be theoretically examined. This may be achieved by means of Monte Carlo simulations, where a prescribed (i.e., known) stack target is superimposed with noise added to the individual records, and the performance of stack reconstruction techniques is assessed via error measures.

Timescale construction for marine sedimentary records currently uses interpolation and astronomical tuning on basis of a set of dated fixpoints (bio-, magneto-, and other chronos-

tratigraphic events). The Bayesian or frequentist methods adopted by the coral [*Hendy et al.*, 2012], ice core [*Parrenin et al.*, 2007; *Klauenberg et al.*, 2011], and speleothem [*Scholz and Hoffmann*, 2011; *Hercman and Pawlak*, 2012] communities could also significantly benefit the marine research community. It is important that a timescale construction algorithm delivers not only the best-fit timescale but also simulated timescales (taking dating errors into account), which can be fed into computer simulation methods of climate time series analysis [*Mudelsee*, 2010]. Such methods are usually a hybrid of a parametric (timescale simulation) and a nonparametric part (bootstrap). They are computing intensive because both parts require many numerical random operations.

With the advent of new proxy records of Cenozoic climate, more spatial raw information enters the database. This principally allows construction of spatio-temporal stochastic models and fit them to data [*Rue and Held*, 2005; *Diggle and Ribeiro Jr.*, 2007; *Cressie and Wikle*, 2011; *Tingley et al.*, 2012]. This could help to relate climate changes in time quantitatively to changes or gradients in geographical space. Evidently, observational data can also be compared with climate model output by means of spatio-temporal stochastic models. To slightly dampen the expectations, it should take a considerable amount of time until measurement capacities and computing power are able to supply enough meaningful data.

5.3. Climate Models

Unraveling the climate variations during the Cenozoic era by means of climate models requires technical advances in data acquisition, conceptual understanding, and numerical modeling. Coupled general circulation models (GCMs) have been utilized to evaluate the

magnitude of future climate change [*Solomon et al.*, 2007; *Stocker et al.*, 2013]. Validation of these models by simulating warm Cenozoic climate states is essential for understanding the sensitivity of the climate system to external forcing. The models are clearly unrivaled in their ability to simulate a broad range of large-scale phenomena on seasonal to decadal timescales [*Meehl et al.*, 2007], but their reliability on longer timescales, when the Earth will most likely enter into a warmer climate, requires additional evaluation. Cenozoic climate records derived from paleo-environmental proxies allow testing of these models because they provide records of past warm climate conditions. With this knowledge, we can study the critical issue whether in Earth system models the key processes associated, for example, with ice sheets, clouds, permafrost, and global biogeochemical cycles—that are all relevant to the climate system—are well captured and if the range of possible solutions is covered by the models [*Schmidt*, 2010; *Schmidt et al.*, 2014]. On the other hand, the models may provide tools to interpret the data in a meaningful way (e.g., regarding temperature) and to understand mechanisms of heterogeneous climate evolution [*Knorr and Lohmann*, 2014]. Past episodes of greenhouse warming furthermore provide insight into the coupling of the climate and the carbon cycle and thus may help to predict the consequences of unabated carbon emissions in the future [*Zachos et al.*, 2008].

For performing the model experiments, one has to know the input parameters, such as greenhouse-gas concentrations or the tectonic configuration [*Mikolajewicz et al.*, 1993; *von der Heydt and Dijkstra*, 2006; *Sijp et al.*, 2009; *Henrot et al.*, 2010; *Butzin et al.*, 2011; *Sijp et al.*, 2011; *Yang et al.*, 2013], and recently such data sets of the gateway configurations have become available [*Herold et al.*, 2008]. Substantial efforts have been

made in this direction using Earth system models [*Steph et al.*, 2006; *You et al.*, 2009; *Knorr et al.*, 2011], but a fully coupled approach including interactive ice sheets and atmosphere–ocean dynamics is still missing.

Until now, most climate models have difficulties in simulating the warm Cenozoic, especially at high latitudes [*Micheels et al.*, 2011; *Huber*, 2012; *Dowsett et al.*, 2013; *Salzmann et al.*, 2013]. It seems that the models systematically underestimate the climate sensitivity on long timescales [*Lohmann et al.*, 2013a; *Salzmann et al.*, 2013] and that they lack the ability to adequately simulate abrupt events such as the PETM [*Valdes*, 2011]. It may be that the models miss feedbacks in the system related, for example, to ocean mixing [*Rose and Ferreira*, 2013; *Green and Huber*, 2013] and/or the quantitative translation of the proxy records into climate variables is problematic. Furthermore, the modeling of the Cenozoic climate is limited to either time-slice experiments performed with GCMs [*Bradshaw et al.*, 2012], or transient experiments performed with simplified climate models [*Merico et al.*, 2008; *Langebroek et al.*, 2009; *Willeit et al.*, 2013]. In the future, paleoclimate modeling shall reach a new stage, as increased computer power makes transient simulations with comprehensive global climate models (still with a low spatial horizontal resolution of several hundred kilometers) feasible. In contrast to conventional time-slice experiments, this approach is not restricted to equilibrium transitions and is, furthermore, capable of utilizing all available data for validation. Earth system models can be used for studying Cenozoic climate dynamics, as a "surrogate laboratory" for numerical experimentation with the climate system to explore mechanisms of the transitions during the Cenozoic (as documented here). In the Earth system model approach, synergetic

effects of the climate components can be evaluated. For example, the vegetation effect on the ocean circulation may be one important mechanism explaining the relatively warm late Miocene climate [*Knorr et al.*, 2011, and references therein]. The special challenges of paleoclimate modeling at these long timescales are balanced by unique opportunities to study the evolution of climate and the Earth system over its full dynamical range including multiple equilibria and thresholds [*Pollard and DeConto*, 2005; *DeConto et al.*, 2008; *Huber*, 2012]. A particular aspect is related to proxy models (e.g., for δ^{18}O), which are necessary to interpret the recorder systems and their large-scale climate information. This approach allows a more direct comparison of data and models. It offers—as in the case of δ^{18}O—the possibility to distinguish between effects of temperature, hydrological cycle, and sea-level variations [*Langebroek et al.*, 2010; *de Boer et al.*, 2012]. Finally, it allows to test the assumptions about the climate recorder systems regarding leads, lags, and other filter properties [*Laepple et al.*, 2011; *Lohmann et al.*, 2013b].

Acknowledgments. Bob Kopp and three others supplied thorough and constructive reviews. Gregor Knorr made helpful comments on the definition of abruptness in climatology. The Deutsche Forschungsgemeinschaft provided financial support (FOR 1070 Understanding Cenozoic Climate Cooling, MU 1595/4-1 Climate Sensitivity during and between Interglacials).

References

Abdul Aziz, H., W. Krijgsman, F. J. Hilgen, D. S. Wilson, and J. P. Calvo (2003), An astronomical polarity timescale for the late middle Miocene based on cyclic continental

sequences, *Journal of Geophysical Research*, *108*(B3), 2159, doi:10.1029/2002JB001818.

Badger, M. P. S., C. H. Lear, R. D. Pancost, G. L. Foster, T. R. Bailey, M. J. Leng, and H. A. Abels (2013), CO_2 drawdown following the middle Miocene expansion of the Antarctic ice sheet, *Paleoceanography*, *28*(1), 42–53, doi:10.1002/palo.20015.

Barras, C., J.-C. Duplessy, E. Geslin, E. Michel, and F. J. Jorissen (2010), Calibration of δ^{18}O of cultured benthic foraminiferal calcite as a function of temperature, *Biogeosciences*, *7*(4), 1349–1356.

Barrera, E., and B. T. Huber (1991), Paleogene and early Neogene oceanography of the Southern Indian Ocean: Leg 119 foraminifer stable isotope results, in *Proc. ODP, Sci. Results*, vol. 119, edited by J. Barron et al., pp. 693–717, Ocean Drilling Program, College Station, T. X.

Bendat, J. S., and A. G. Piersol (2010), *Random Data: Analysis and Measurement Procedures*, fourth ed., 604 pp., Wiley, Hoboken, N. J.

Berger, A. L. (1978), Long-term variations of daily insolation and Quaternary climatic changes, *Journal of the Atmospheric Sciences*, *35*(12), 2362–2367.

Berger, W. H., and E. Jansen (1994), Mid-Pleistocene climate shift—the Nansen connection, in *The Polar Oceans and Their Role in Shaping the Global Environment*, edited by O. M. Johannessen, R. D. Muench, and J. E. Overland, pp. 295–311, American Geophysical Union, Washington, D. C.

Berger, W. H., and E. L. Winterer (1974), Plate stratigraphy and the fluctuating carbonate line, in *Pelagic Sediments: on Land and under the Sea*, edited by K. J. Hsü and H. C. Jenkyns, pp. 11–48, Blackwell, Oxford.

Berggren, W. A., D. V. Kent, C. C. Swisher III, and M.-P. Aubry (1995), A revised Cenozoic geochronology and chronostratigraphy, in *Geochronology, Time Scales and Global Stratigraphic Correlation*, edited by W. A. Berggren, D. V. Kent, M.-P. Aubry, and J. Hardenbol, pp. 129–212, Society for Sedimentary Geology, Tulsa, O. K.

Bevington, P. R., and D. K. Robinson (1992), *Data reduction and error analysis for the physical sciences*, second ed., 328 pp., McGraw-Hill, New York.

Billups, K., and K. Scheiderich (2010), A synthesis of late Oligocene through Miocene deep sea temperatures as inferred from foraminiferal Mg/Ca ratios, in *Carbonate Systems During the Oligocene–Miocene Climatic Transition*, edited by M. Mutti, W. E. Piller, and C. Betzler, pp. 1–16, Wiley, Chichester.

Billups, K., and D. P. Schrag (2002), Paleotemperatures and ice volume of the past 27 Myr revisited with paired Mg/Ca and $^{18}O/^{16}O$ measurements on benthic foraminifera, *Paleoceanography*, *17*(1), 1003, doi:10.1029/2000PA000567.

Billups, K., and D. P. Schrag (2003), Application of benthic foraminiferal Mg/Ca ratios to questions of Cenozoic climate change, *Earth and Planetary Science Letters*, *209*(1–2), 181–195.

Birge, R. T. (1932), The calculation of errors by the method of least squares, *Physical Review*, *40*(2), 207–227.

Bohaty, S. M., and J. C. Zachos (2003), Significant Southern Ocean warming event in the late middle Eocene, *Geology*, *31*(11), 1017–1020.

Bohaty, S. M., J. C. Zachos, and M. L. Delaney (2012), Foraminiferal Mg/Ca evidence for Southern Ocean cooling across the Eocene–Oligocene transition, *Earth and Planetary*

Science Letters, *317–318*, 251–261.

Bottomley, R., R. Grieve, D. York, and V. Masaitis (1997), The age of the Popigai impact event and its relation to events at the Eocene/Oligocene boundary, *Nature*, *388*(6640), 365–368.

Bradley, R. S. (1999), *Paleoclimatology: Reconstructing Climates of the Quaternary*, second ed., 610 pp., Academic Press, San Diego.

Bradshaw, C. D., D. J. Lunt, R. Flecker, U. Salzmann, M. J. Pound, A. M. Haywood, and J. T. Eronen (2012), The relative roles of CO_2 and palaeogeography in determining late Miocene climate: Results from a terrestrial model–data comparison, *Climate of the Past*, *8*(2), 1257–1285.

Briskin, M., and J. Harrell (1980), Time-series analysis of the pleistocene deep-sea paleoclimatic record, *Marine Geology*, *36*(1–2), 1–22.

Brockmann, M., T. Gasser, and E. Herrmann (1993), Locally adaptive bandwidth choice for kernel regression estimators, *Journal of the American Statistical Association*, *88*(424), 1302–1309.

Broecker, W. S. (1995), *The glacial world according to Wally*, 318 pp., Eldigio Press, Palisades, New York.

Buck, C. E., and A. R. Millard (Eds.) (2004), *Tools for Constructing Chronologies: Crossing Disciplinary Boundaries*, 257 pp., Springer, London.

Butzin, M., G. Lohmann, and T. Bickert (2011), Miocene ocean circulation inferred from marine carbon cycle modeling combined with benthic isotope records, *Paleoceanography*, *26*(1), PA1203, doi:10.1029/2009PA001901.

Cande, S. C., and D. V. Kent (1995), Revised calibration of the geomagnetic polarity timescale for the late Cretaceous and Cenozoic, *Journal of Geophysical Research*, *100*(B4), 6093–6095.

Cerling, T. E., J. M. Harris, B. J. MacFadden, M. G. Leakey, J. Quade, V. Eisenmann, and J. R. Ehleringer (1997), Global vegetation change through the Miocene/Pliocene boundary, *Nature*, *389*(6647), 153–158.

Coxall, H. K., and P. A. Wilson (2011), Early Oligocene glaciation and productivity in the eastern equatorial Pacific: Insights into global carbon cycling, *Paleoceanography*, *26*(2), PA2221, doi:10.1029/2010PA002021.

Coxall, H. K., P. A. Wilson, H. Pälike, C. H. Lear, and J. Backman (2005), Rapid stepwise onset of Antarctic glaciation and deeper calcite compensation in the Pacific Ocean, *Nature*, *433*(7021), 53–57.

Cramer, B. S., J. R. Toggweiler, J. D. Wright, M. E. Katz, and K. G. Miller (2009), Ocean overturning since the late Cretaceous: Inferences from a new benthic foraminiferal isotope compilation, *Paleoceanography*, *24*(4), PA4216, doi:10.1029/2008PA001683.

Cramer, B. S., K. G. Miller, P. J. Barrett, and J. D. Wright (2011), Late Cretaceous–Neogene trends in deep ocean temperature and continental ice volume: Reconciling records of benthic foraminiferal geochemistry (δ^{18}O and Mg/Ca) with sea level history, *Journal of Geophysical Research*, *116*(C12), C12023, doi:10.1029/2011JC007255.

Creech, J. B., J. A. Baker, C. J. Hollis, H. E. G. Morgans, and E. G. C. Smith (2010), Eocene sea temperatures for the mid-latitude southwest Pacific from Mg/Ca ratios in planktonic and benthic foraminifera, *Earth and Planetary Science Letters*, *299*(3–4),

483–495.

Cressie, N., and C. K. Wikle (2011), *Statistics for Spatio-Temporal Data*, 588 pp., Wiley, Hoboken, N. J.

Cristini, L., K. Grosfeld, M. Butzin, and G. Lohmann (2012), Influence of the opening of the Drake Passage on the Cenozoic Antarctic ice sheet: A modeling approach, *Palaeogeography, Palaeoclimatology, Palaeoecology*, *339–341*, 66–73.

Cronin, T. M. (2010), *Paleoclimates: Understanding Climate Change Past and Present*, 441 pp., Columbia University Press, New York.

Crowley, T. J., and K. C. Burke (Eds.) (1998), *Tectonic Boundary Conditions for Climate Reconstructions*, 285 pp., Oxford University Press, New York.

Crowley, T. J., and G. R. North (1990), Modeling onset of glaciation, *Annals of Glaciology*, *14*(1), 39–42.

Crowley, T. J., and G. R. North (1991), *Paleoclimatology*, 339 pp., Oxford University Press, New York.

Dawber, C. F., and A. K. Tripati (2011), Constraints on glaciation in the middle Eocene (46–37 Ma) from Ocean Drilling Program (ODP) Site 1209 in the tropical Pacific Ocean, *Paleoceanography*, *26*(2), PA2208, doi:10.1029/2010PA002037.

de Boer, B., R. S. W. van de Wal, L. J. Lourens, and R. Bintanja (2012), Transient nature of the Earth's climate and the implications for the interpretation of benthic δ^{18}O records, *Palaeogeography, Palaeoclimatology, Palaeoecology*, *335–336*, 4–11.

DeConto, R. M., and D. Pollard (2003), Rapid Cenozoic glaciation of Antarctica induced by declining atmospheric CO_2, *Nature*, *421*(6920), 245–249.

DeConto, R. M., D. Pollard, P. A. Wilson, H. Pälike, C. H. Lear, and M. Pagani (2008), Thresholds for Cenozoic bipolar glaciation, *Nature*, *455*(7213), 652–656.

DeConto, R. M., S. Galeotti, M. Pagani, D. Tracy, K. Schaefer, T. Zhang, D. Pollard, and D. J. Beerling (2012), Past extreme warming events linked to massive carbon release from thawing permafrost, *Nature*, *484*(7392), 87–91.

Deep Sea Drilling Project (Ed.) (1969–1986), *Initial Reports of the Deep Sea Drilling Project*, vol. 1–96, U.S. Govt. Printing Office, Washington, D. C.

Diester-Haass, L., K. Billups, D. R. Gröcke, L. François, V. Lefebvre, and K. C. Emeis (2009), Mid-Miocene paleoproductivity in the Atlantic Ocean and implications for the global carbon cycle, *Paleoceanography*, *24*(1), PA1209, doi:10.1029/2008PA001605.

Diester-Haass, L., K. Billups, I. Jacquemin, K. C. Emeis, V. Lefebvre, and L. François (2013), Paleoproductivity during the middle Miocene carbon isotope events: A data–model approach, *Paleoceanography*, *28*(2), 334–346, doi:10.1002/palo.20033.

Diggle, P. J., and P. J. Ribeiro Jr. (2007), *Model-based Geostatistics*, 228 pp., Springer, New York.

Dowsett, H. J., K. M. Foley, D. K. Stoll, M. A. Chandler, L. E. Sohl, M. Bentsen, B. L. Otto-Bliesner, F. J. Bragg, W.-L. Chan, C. Contoux, A. M. Dolan, A. M. Haywood, J. A. Jonas, A. Jost, Y. Kamae, G. Lohmann, D. J. Lunt, K. H. Nisancioglu, A. Abe-Ouchi, G. Ramstein, C. R. Riesselman, M. M. Robinson, N. A. Rosenbloom, U. Salzmann, C. Stepanek, S. L. Strother, H. Ueda, Q. Yan, and Z. Zhang (2013), Sea surface temperature of the mid-Piacenzian ocean: A data–model comparison, *Nature Reports Climate Change*, *3*, doi:10.1038/srep02013.

Dutton, A., K. C. Lohmann, and R. M. Leckie (2005), Insights from the Paleogene tropical Pacific: Foraminiferal stable isotope and elemental results from Site 1209, Shatsky Rise, *Paleoceanography*, *20*(3), PA3004, doi:10.1029/2004PA001098.

Edgar, K. M., H. Pälike, and P. A. Wilson (2013), Testing the impact of diagenesis on the δ^{18}O and δ^{13}C of benthic foraminiferal calcite from a sediment burial depth transect in the equatorial Pacific, *Paleoceanography*, *28*(3), 468–480, doi:10.1002/palo.20045.

Efron, B. (1979), Bootstrap methods: Another look at the jackknife, *The Annals of Statistics*, *7*(1), 1–26.

Efron, B., and R. J. Tibshirani (1993), *An Introduction to the Bootstrap*, 436 pp., Chapman and Hall, London.

Egan, K. E., R. E. M. Rickaby, K. R. Hendry, and A. N. Halliday (2013), Opening the gateways for diatoms primes Earth for Antarctic glaciation, *Earth and Planetary Science Letters*, *375*, 34–43.

Ehrmann, W. U., M. J. Hambrey, J. G. Baldauf, J. Barron, B. Larsen, A. Mackensen, S. W. Wise Jr., and J. C. Zachos (1992), History of Antarctic glaciation: An Indian Ocean perspective, in *Synthesis of Results from Scientific Drilling in the Indian Ocean*, edited by R. A. Duncan, D. K. Rea, R. B. Kidd, U. von Rad, and J. K. Weissel, pp. 423–446, American Geophysical Union, Washington, D. C.

Eiler, J. M. (2007), "Clumped-isotope" geochemistry—The study of naturally-occuring, multiply-substituted isotopologues, *Earth and Planetary Science Letters*, *262*(3–4), 309–327.

Eiler, J. M. (2011), Paleoclimate reconstruction using carbonate clumped isotope thermometry, *Quaternary Science Reviews*, *30*(25–26), 3575–3588.

Elderfield, H., J. Yu, P. Anand, T. Kiefer, and B. Nyland (2006), Calibrations for benthic foraminiferal Mg/Ca paleothermometry and the carbonate ion hypothesis, *Earth and Planetary Science Letters*, *250*(3–4), 633–649.

Elderfield, H., M. Greaves, S. Barker, I. R. Hall, A. Tripati, P. Ferretti, S. Crowhurst, L. Booth, and C. Daunt (2010), A record of bottom water temperature and seawater δ^{18}O for the Southern Ocean over the past 440 kyr based on Mg/Ca of benthic foraminiferal *Uvigerina* spp., *Quaternary Science Reviews*, *29*(1–2), 160–169.

Eldrett, J. S., I. C. Harding, P. A. Wilson, E. Butler, and A. P. Roberts (2007), Continental ice in Greenland during the Eocene and Oligocene, *Nature*, *446*(7132), 176–179.

Epstein, S., R. Buchsbaum, H. A. Lowenstam, and H. C. Urey (1953), Revised carbonate-water isotopic temperature scale, *Geological Society of America Bulletin*, *64*(11), 1315–1325.

Fairbanks, R. G., and R. K. Matthews (1978), The marine oxygen isotope record in Pleistocene coral, Barbados, West Indies, *Quaternary Research*, *10*(2), 181–196.

Farley, K. A., and S. F. Eltgroth (2003), An alternative age model for the Paleocene–Eocene thermal maximum using extraterrestrial ^{3}He, *Earth and Planetary Science Letters*, *208*(3–4), 135–148.

Fischer, A. G. (1981), Climatic oscillations in the biosphere, in *Biotic Crises in Ecological and Evolutionary Time*, edited by M. H. Nitecki, pp. 103–131, Academic Press, New York.

Flower, B. P., and J. P. Kennett (1993a), Middle Miocene ocean–climate transition: High-resolution oxygen and carbon isotopic records from Deep Sea Drilling Project Site 588A, southwest Pacific, *Paleoceanography*, *8*(6), 811–843.

Flower, B. P., and J. P. Kennett (1993b), Relations between Monterey Formation deposition and middle Miocene global cooling: Naples Beach section, California, *Geology*, *21*(10), 877–880.

Flower, B. P., and J. P. Kennett (1994), The middle Miocene climatic transition: East Antarctic ice sheet development, deep ocean circulation and global carbon cycling, *Palaeogeography, Palaeoclimatology, Palaeoecology*, *108*(3–4), 537–555.

Flower, B. P., and J. P. Kennett (1995), Middle Miocene deepwater paleoceanography in the southwest Pacific: Relations with East Antarctic ice sheet development, *Paleoceanography*, *10*(6), 1095–1112.

Foster, G. L., C. H. Lear, and J. W. B. Rae (2012), The evolution of pCO_2, ice volume and climate during the middle Miocene, *Earth and Planetary Science Letters*, *341*, 243–254.

Fretwell, P., H. D. Pritchard, D. G. Vaughan, J. L. Bamber, N. E. Barrand, R. Bell, C. Bianchi, R. G. Bingham, D. D. Blankenship, G. Casassa, G. Catania, D. Callens, H. Conway, A. J. Cook, H. F. J. Corr, D. Damaske, V. Damm, F. Ferraccioli, R. Forsberg, S. Fujita, Y. Gim, P. Gogineni, J. A. Griggs, R. C. A. Hindmarsh, P. Holmlund, J. W. Holt, R. W. Jacobel, A. Jenkins, W. Jokat, T. Jordan, E. C. King, J. Kohler, W. Krabill, M. Riger-Kusk, K. A. Langley, G. Leitchenkov, C. Leuschen, B. P. Luyendyk, K. Matsuoka, J. Mouginot, F. O. Nitsche, Y. Nogi, O. A. Nost, S. V. Popov, E. Rignot, D. M. Rippin, A. Rivera, J. Roberts, N. Ross, M. J. Siegert, A. M.

Smith, D. Steinhage, M. Studinger, B. Sun, B. K. Tinto, B. C. Welch, D. Wilson, D. A. Young, C. Xiangbin, and A. Zirizzotti (2013), Bedmap2: Improved ice bed, surface and thickness datasets for Antarctica, *Cryosphere*, *7*(1), 375–393.

Gasser, T., and H.-G. Müller (1979), Kernel estimation of regression functions, in *Smoothing Techniques for Curve Estimation*, edited by T. Gasser and M. Rosenblatt, pp. 23–68, Springer, Berlin.

Gasser, T., and H.-G. Müller (1984), Estimating regression functions and their derivatives by the kernel method, *Scandinavian Journal of Statistics*, *11*(3), 171–185.

Gasson, E., M. Siddall, D. J. Lunt, O. J. L. Rackham, C. H. Lear, and D. Pollard (2012), Exploring uncertainties in the relationship between temperature, ice volume, and sea level over the past 50 million years, *Reviews of Geophysics*, *50*(1), RG1005, doi:10.1029/2011RG000358.

Gilman, D. L., F. J. Fuglister, and J. M. Mitchell Jr. (1963), On the power spectrum of "red noise", *Journal of the Atmospheric Sciences*, *20*(2), 182–184.

Gradstein, F. M., J. G. Ogg, and A. G. Smith (Eds.) (2004), *A Geologic Time Scale 2004*, 589 pp., Cambridge University Press, Cambridge.

Green, J. A. M., and M. Huber (2013), Tidal dissipation in the early Eocene and implications for ocean mixing, *Geophysical Research Letters*, *40*(11), 2707-2713, doi: 10.1002/grl.50510.

Hasselmann, K. (1976), Stochastic climate models: Part I. Theory, *Tellus*, *28*(6), 473–485.

Hendy, E. J., P. J. Tomiak, M. J. Collins, J. Hellstrom, A. W. Tudhope, J. M. Lough, and K. E. H. Penkman (2012), Assessing amino acid racemization variability in coral

intra-crystalline protein for geochronological applications, *Geochimica et Cosmochimica Acta*, *86*, 338–353.

Henrot, A.-J., L. François, E. Favre, M. Butzin, M. Ouberdous, and G. Munhoven (2010), Effects of CO_2, continental distribution, topography and vegetation changes on the climate at the middle Miocene: A model study, *Climate of the Past*, *6*(5), 675–694.

Hercman, H., and J. Pawlak (2012), MOD-AGE: An age–depth model construction algorithm, *Quaternary Geochronology*, *12*, 1–10.

Herold, N., M. Seton, R. D. Müller, Y. You, and M. Huber (2008), Middle Miocene tectonic boundary conditions for use in climate models, *Geochemistry, Geophysics, Geosystems*, *9*(10), Q10009, doi:10.1029/2008GC002046.

Herrmann, E. (1997), Local bandwidth choice in kernel regression estimation, *Journal of Computational and Graphical Statistics*, *6*(1), 35–54.

Hilgen, F. J., W. Krijgsman, C. G. Langereis, L. J. Lourens, A. Santarelli, and W. J. Zachariasse (1995), Extending the astronomical (polarity) time scale into the Miocene, *Earth and Planetary Science Letters*, *136*(3–4), 495–510.

Hinnov, L. A. (2000), New perspectives on orbitally forced stratigraphy, *Annual Review of Earth and Planetary Sciences*, *28*, 419–475.

Holbourn, A., W. Kuhnt, M. Schulz, and H. Erlenkeuser (2005), Impacts of orbital forcing and atmospheric carbon dioxide on Miocene ice-sheet expansion, *Nature*, *438*(7067), 483–487.

Holbourn, A., W. Kuhnt, M. Schulz, J.-A. Flores, and N. Andersen (2007), Orbitally-paced climate evolution during the middle Miocene "Monterey" carbon-isotope excur-

sion, *Earth and Planetary Science Letters*, *261*(3–4), 534–550.

Holbourn, A., W. Kuhnt, S. Clemens, W. Prell, and N. Andersen (2013), Middle to late Miocene stepwise climate cooling: Evidence from a high-resolution deep water isotope curve spanning 8 million years, *Paleoceanography*, *28*(4), 688–699, doi: 10.1002/2013PA002538.

Hollis, C. J., K. W. R. Taylor, L. Handley, R. D. Pancost, M. Huber, J. B. Creech, B. R. Hines, E. M. Crouch, H. E. G. Morgans, J. S. Crampton, S. Gibbs, P. N. Pearson, and J. C. Zachos (2012), Early Paleogene temperature history of the southwest Pacific Ocean: Reconciling proxies and models, *Earth and Planetary Science Letters*, *349–350*, 53–66.

Huber, M. (2012), Progress in greenhouse climate modeling, in *Reconstructing Earth's Deep-Time Climate—The State of the Art in 2012*, edited by L. C. Ivany and B. T. Huber, pp. 213–262, Paleontological Society, Lawrence, K. S.

Huber, M., and R. Caballero (2011), The early Eocene equable climate problem revisited, *Climate of the Past*, *7*(2), 603–633.

Imbrie, J., J. D. Hays, D. G. Martinson, A. McIntyre, A. C. Mix, J. J. Morley, N. G. Pisias, W. L. Prell, and N. J. Shackleton (1984), The orbital theory of Pleistocene climate: Support from a revised chronology of the marine δ^{18}O record, in *Milankovitch and Climate*, vol. 1, edited by A. Berger, J. Imbrie, J. Hays, G. Kukla, and B. Saltzman, pp. 269–305, D. Reidel, Dordrecht.

Integrated Ocean Drilling Program (Ed.) (2005ff.), *Proceedings of the Integrated Ocean Drilling Program*, vol. 301ff., Integrated Ocean Drilling Program Management Interna-

tional, College Station, T. X.

Ivany, L. C., S. Van Simaeys, E. W. Domack, and S. D. Samson (2006), Evidence for an earliest Oligocene ice sheet on the Antarctic Peninsula, *Geology*, *34*(5), 377–380.

Kashiwaya, K., S. Ochiai, H. Sakai, and T. Kawai (2001), Orbit-related long-term climate cycles revealed in a 12-Myr continental record from Lake Baikal, *Nature*, *410*(6824), 71–74.

Katz, M. E., K. G. Miller, J. D. Wright, B. S. Wade, J. V. Browning, B. S. Cramer, and Y. Rosenthal (2008), Stepwise transition from the Eocene greenhouse to the Oligocene icehouse, *Nature Geoscience*, *1*(5), 329–334.

Kennett, J. P. (1982), *Marine Geology*, 813 pp., Prentice-Hall, Englewood Cliffs, N. J.

Kennett, J. P., and N. F. Exon (2004), Paleoceanographic evolution of the Tasmanian Seaway and its climatic implications, in *The Cenozoic Southern Ocean: Tectonics, Sedimentation, and Climate Change Between Australia and Antarctica*, edited by N. F. Exon, J. P. Kennett, and M. J. Malone, pp. 345–367, American Geophysical Union, Washington, D. C.

Kennett, J. P., and L. D. Stott (1990), Proteus and Proto-Oceanus: Ancestral Paleogene oceans as revealed from Antarctic stable isotopic results; ODP Leg 113, in *Proc. ODP, Sci. Results*, vol. 113, edited by P. F. Barker et al., pp. 225–229, Ocean Drilling Program, College Station, T. X.

Kennett, J. P., and L. D. Stott (1991), Abrupt deep-sea warming, palaeoceanographic changes and benthic extinctions at the end of the Palaeocene, *Nature*, *353*(6341), 225–229.

Kent, D. V. (1999), Orbital tuning of geomagnetic polarity time-scales, *Philosophical Transactions of the Royal Society of London, Series A*, *357*(1757), 1995–2007.

Klauenberg, K., P. G. Blackwell, C. E. Buck, R. Mulvaney, R. Röthlisberger, and E. W. Wolff (2011), Bayesian glaciological modelling to quantify uncertainties in ice core chronologies, *Quaternary Science Reviews*, *30*(21–22), 2961–2975.

Knorr, G., and G. Lohmann (2014), A warming climate during the Antarctic ice sheet growth at the Middle Miocene transition, *Nature Geoscience*, doi:10.1038/NGEO2119, to appear March 2014.

Knorr, G., M. Butzin, A. Micheels, and G. Lohmann (2011), A warm Miocene climate at low atmospheric CO_2 levels, *Geophysical Research Letters*, *38*(20), L20701, doi: 10.1029/2011GL048873.

Kroopnick, P. M. (1985), The distribution of ^{13}C of $\sum CO_2$ in the world oceans, *Deep-Sea Research A*, *32*(1), 57–84.

Künsch, H. R. (1989), The jackknife and the bootstrap for general stationary observations, *The Annals of Statistics*, *17*(3), 1217–1241.

Laepple, T., and G. Lohmann (2009), Seasonal cycle as template for climate variability on astronomical timescales, *Paleoceanography*, *24*(4), PA4201, doi:10.1029/2008PA001674.

Laepple, T., M. Werner, and G. Lohmann (2011), Synchronicity of Antarctic temperatures and local solar insolation on orbital timescales, *Nature*, *471*(7336), 91–94.

Langebroek, P. M., A. Paul, and M. Schulz (2009), Antarctic ice-sheet response to atmospheric CO_2 and insolation in the middle Miocene, *Climate of the Past*, *5*(4), 633–646.

Langebroek, P. M., A. Paul, and M. Schulz (2010), Simulating the sea level imprint on marine oxygen isotope records during the middle Miocene using an ice sheet–climate model, *Paleoceanography*, *25*(4), PA4203, doi:10.1029/2008PA001704.

Le Roux, J. P. (2012a), A review of Tertiary climate changes in southern South America and the Antarctic peninsula. Part 1: Oceanic conditions, *Sedimentary Geology*, *247–248*, 1–20.

Le Roux, J. P. (2012b), A review of Tertiary climate changes in southern South America and the Antarctic peninsula. Part 2: Continental conditions, *Sedimentary Geology*, *247–248*, 21–38.

Lear, C. H. (2007), Mg/Ca palaeothermometry: A new window into Cenozoic climate change, in *Deep-Time Perspectives on Climate Change: Marrying the Signal from Computer Models and Biological Proxies*, edited by M. Williams, A. M. Haywood, F. J. Gregory, and D. N. Schmidt, pp. 313–322, The Geological Society, London, (published for The Micropalaeontological Society).

Lear, C. H., H. Elderfield, and P. A. Wilson (2000), Cenozoic deep-sea temperatures and global ice volumes from Mg/Ca in benthic foraminiferal calcite, *Science*, *287*(5451), 269–272.

Lear, C. H., Y. Rosenthal, and J. D. Wright (2003), The closing of a seaway: Ocean water masses and global climate change, *Earth and Planetary Science Letters*, *210*(3–4), 425–436.

Lear, C. H., Y. Rosenthal, H. K. Coxall, and P. A. Wilson (2004), Late Eocene to early Miocene ice sheet dynamics and the global carbon cycle, *Paleoceanography*, *19*(4),

PA4015, doi:10.1029/2004PA001039.

Lear, C. H., T. R. Bailey, P. N. Pearson, H. K. Coxall, and Y. Rosenthal (2008), Cooling and ice growth across the Eocene–Oligocene transition, *Geology*, *36*(3), 251–254.

Lear, C. H., E. M. Mawbey, and Y. Rosenthal (2010), Cenozoic benthic foraminiferal Mg/Ca and Li/Ca records: Toward unlocking temperatures and saturation states, *Paleoceanography*, *25*(4), P4215, doi:10.1029/2009PA001880.

Lisiecki, L. E., and M. E. Raymo (2005), A Plio–Pleistocene stack of 57 globally distributed benthic δ^{18}O records, *Paleoceanography*, *20*(1), PA1003, doi: 10.1029/2004PA001071.

Livina, V. N., F. Kwasniok, G. Lohmann, J. W. Kantelhardt, and T. M. Lenton (2011), Changing climate states and stability: From Pliocene to present, *Climate Dynamics*, *37*(11–12), 2437–2453.

Livina, V. N., G. Lohmann, M. Mudelsee, and T. M. Lenton (2013), Forecasting the underlying potential governing the time series of a dynamical system, *Physica A*, *392*(18), 3891–3902.

Lohmann, G., M. Pfeiffer, T. Laepple, G. Leduc, and J.-H. Kim (2013a), A model–data comparison of the Holocene global sea surface temperature evolution, *Climate of the Past*, *9*(4), 1807–1839.

Lohmann, G., A. Wackerbarth, P. M. Langebroek, M. Werner, J. Fohlmeister, D. Scholz, and A. Mangini (2013b), Simulated European stalagmite record and its relation to a quasi-decadal climate mode, *Climate of the Past*, *9*(1), 89–98.

Lourens, L. J., A. Sluijs, D. Kroon, J. C. Zachos, E. Thomas, U. Röhl, J. Bowles, and I. Raffi (2005), Astronomical pacing of late Palaeocene to early Eocene global warming events, *Nature*, *435*(7045), 1083–1087.

Lyle, M., A. Olivarez Lyle, J. Backman, and A. Tripati (2005), Biogenic sedimentation in the Eocene equatorial Pacific—the stuttering greenhouse and Eocene carbonate compensation depth, in *Proc. ODP, Sci. Results*, vol. 199, edited by P. A. Wilson, M. Lyle, and J. V. Firth, pp. 1–35, Ocean Drilling Program, College Station, T. X.

Lyle, M., J. Barron, T. J. Bralower, M. Huber, A. Olivarez Lyle, A. C. Ravelo, D. K. Rea, and P. A. Wilson (2008), Pacific Ocean and Cenozoic evolution of climate, *Reviews of Geophysics*, *46*(2), RG2002, doi:10.1029/2005RG000190.

Marchitto, T. M., W. B. Curry, J. Lynch-Stieglitz, S. P. Bryan, K. M. Cobb, and D. C. Lund (2014), Improved oxygen isotope temperature calibrations for cosmopolitan benthic foraminifera, *Geochimica et Cosmochimica Acta*, *130*, 1–11.

Martinson, D. G., N. G. Pisias, J. D. Hays, J. Imbrie, T. C. Moore Jr., and N. J. Shackleton (1987), Age dating and the orbital theory of the ice ages: Development of a high-resolution 0 to 300,000-year chronostratigraphy, *Quaternary Research*, *27*(1), 1–29.

Masson-Delmotte, V., M. Schulz, A. Abe-Ouchi, J. Beer, A. Ganopolski, J. F. González Rouco, E. Jansen, K. Lambeck, J. Luterbacher, T. Naish, T. Osborn, B. Otto-Bliesner, T. Quinn, R. Ramesh, M. Rojas, X. Shao, and A. Timmermann (2013), Information from paleoclimate archives, in *Climate Change 2013: The Physical Science Basis. Working Group I Contribution to the Fifth Assessment Report of the Intergovernmental Panel on Climate Change*, edited by T. F. Stocker, D. Qin, G.-K. Plattner,

M. M. B. Tignor, S. K. Allen, J. Boschung, A. Nauels, Y. Xia, V. Bex, and P. M. Midgley, pp. 383–464, Cambridge University Press, Cambridge.

Mawbey, E. M., and C. H. Lear (2013), Carbon cycle feedbacks during the Oligocene–Miocene transient glaciation, *Geology*, doi:10.1130/G34422.1, published online 3 July 2013.

Meehl, G. A., T. F. Stocker, W. D. Collins, P. Friedlingstein, A. T. Gaye, J. M. Gregory, A. Kitoh, R. Knutti, J. M. Murphy, A. Noda, S. C. B. Raper, I. G. Watterson, A. J. Weaver, and Z.-C. Zhao (2007), Global climate projections, in *Climate Change 2007: The Physical Science Basis. Contribution of Working Group I to the Fourth Assessment Report of the Intergovernmental Panel on Climate Change*, edited by S. Solomon, D. Qin, M. Manning, M. Marquis, K. Averyt, M. M. B. Tignor, H. L. Miller Jr., and Z. Chen, pp. 747–845, Cambridge University Press, Cambridge.

Merico, A., T. Tyrrell, and P. A. Wilson (2008), Eocene/Oligocene ocean de-acidification linked to Antarctic glaciation by sea-level fall, *Nature*, *452*(7190), 979–982.

Micheels, A., A. A. Bruch, J. Eronen, M. Fortelius, M. Harzhauser, T. Utescher, and V. Mosbrugger (2011), Analysis of heat transport mechanisms from a late Miocene model experiment with a fully-coupled atmosphere–ocean general circulation model, *Palaeogeography, Palaeoclimatology, Palaeoecology*, *304*(3–4), 337–350.

Mikolajewicz, U., E. Maier-Reimer, T. J. Crowley, and K.-Y. Kim (1993), Effect of Drake and Panamanian gateways on the circulation of an ocean model, *Paleoceanography*, *8*(4), 409–426.

Miller, K. G., R. G. Fairbanks, and G. S. Mountain (1987), Tertiary oxygen isotope synthesis, sea level history, and continental margin erosion, *Paleoceanography*, *2*(1), 1–19.

Miller, K. G., J. D. Wright, and R. G. Fairbanks (1991), Unlocking the ice house: Oligocene–Miocene oxygen isotopes, eustacy, and margin erosion, *Journal of Geophysical Research*, *96*(B4), 6829–6848.

Mix, A. C., and W. F. Ruddiman (1984), Oxygen-isotope analyses and Pleistocene ice volumes, *Quaternary Research*, *21*(1), 1–20.

Montgomery, D. C., and E. A. Peck (1992), *Introduction to Linear Regression Analysis*, second ed., 527 pp., Wiley, New York.

Mudelsee, M. (2000), Ramp function regression: A tool for quantifying climate transitions, *Computers and Geosciences*, *26*(3), 293–307.

Mudelsee, M. (2002), TAUEST: A computer program for estimating persistence in unevenly spaced weather/climate time series, *Computers and Geosciences*, *28*(1), 69–72.

Mudelsee, M. (2009), Break function regression: A tool for quantifying trend changes in climate time series, *European Physical Journal Special Topics*, *174*(1), 49–63.

Mudelsee, M. (2010), *Climate Time Series Analysis: Classical Statistical and Bootstrap Methods*, 474 pp., Springer, Dordrecht.

Mudelsee, M., and M. E. Raymo (2005), Slow dynamics of the Northern Hemisphere glaciation, *Paleoceanography*, *20*(4), PA4022, doi:doi:10.1029/2005PA001153.

Mudelsee, M., D. Scholz, R. Röthlisberger, D. Fleitmann, A. Mangini, and E. W. Wolff (2009), Climate spectrum estimation in the presence of timescale errors, *Nonlinear*

Processes in Geophysics, *16*(1), 43–56.

Mudelsee, M., J. Fohlmeister, and D. Scholz (2012), Effects of dating errors on nonparametric trend analyses of speleothem time series, *Climate of the Past*, *8*(5), 1637–1648.

Murphy, B. H., K. A. Farley, and J. C. Zachos (2010), An extraterrestrial ^{3}He-based timescale for the Paleocene–Eocene thermal maximum (PETM) from Walvis Ridge, IODP Site 1266, *Geochimica et Cosmochimica Acta*, *74*(17), 5098–5108.

Naish, T. R., K. J. Woolfe, P. J. Barrett, G. S. Wilson, C. Atkins, S. M. Bohaty, C. J. Bücker, M. Claps, F. J. Davey, G. B. Dunbar, A. G. Dunn, C. R. Fielding, F. Florindo, M. J. Hannah, D. M. Harwood, S. A. Henrys, L. A. Krissek, M. Lavelle, J. van der Meer, W. C. McIntosh, F. Niessen, S. Passchier, R. D. Powell, A. P. Roberts, L. Sagnotti, R. P. Scherer, C. P. Strong, F. Talarico, K. L. Verosub, G. Villa, D. K. Watkins, P.-N. Webb, and T. Wonik (2001), Orbitally induced oscillations in the East Antarctic ice sheet at the Oligocene/Miocene boundary, *Nature*, *413*(6857), 719–723.

Nisancioglu, K. H., M. E. Raymo, and P. H. Stone (2003), Reorganization of Miocene deep water circulation in response to the shoaling of the Central American Seaway, *Paleoceanography*, *18*(1), 1006, doi:10.1029/2002PA000767.

Ocean Drilling Program (Ed.) (1986–2004), *Proceedings of the Ocean Drilling Program, Initial Reports*, vol. 101–210, Ocean Drilling Program, College Station, T. X.

Ocean Drilling Program (Ed.) (1988–2007), *Proceedings of the Ocean Drilling Program, Scientific Results*, vol. 101–210, Ocean Drilling Program, College Station, T. X.

Oeschger, H., and C. C. Langway Jr. (Eds.) (1989), *The Environmental Record in Glaciers and Ice Sheets*, 401 pp., Wiley, Chichester.

Pagani, M., M. Huber, Z. Liu, S. M. Bohaty, J. Henderiks, W. Sijp, S. Krishnan, and R. M. DeConto (2011), The role of carbon dioxide during the onset of Antarctic glaciation, *Science*, *334*(6060), 1261–1264.

PALAEOSENS Project Members (2012), Making sense of palaeoclimate sensitivity, *Nature*, *491*(7426), 683–691.

Pälike, H., R. D. Norris, J. O. Herrle, P. A. Wilson, H. K. Coxall, C. H. Lear, N. J. Shackleton, A. K. Tripati, and B. S. Wade (2006), The heartbeat of the Oligocene climate system, *Science*, *314*(5807), 1894–1898.

Pälike, H., M. W. Lyle, H. Nishi, I. Raffi, A. Ridgwell, K. Gamage, A. Klaus, G. Acton, L. Anderson, J. Backman, J. Baldauf, C. Beltran, S. M. Bohaty, P. Bown, W. Busch, J. E. T. Channell, C. O. J. Chun, M. Delaney, P. Dewangan, T. Dunkley Jones, K. M. Edgar, H. Evans, P. Fitch, G. L. Foster, N. Gussone, H. Hasegawa, E. C. Hathorne, H. Hayashi, J. O. Herrle, A. Holbourn, S. Hovan, K. Hyeong, K. Iijima, T. Ito, S.-i. Kamikuri, K. Kimoto, J. Kuroda, L. Leon-Rodriguez, A. Malinverno, T. C. Moore Jr., B. H. Murphy, D. P. Murphy, H. Nakamura, K. Ogane, C. Ohneiser, C. Richter, R. Robinson, E. J. Rohling, O. Romero, K. Sawada, H. Scher, L. Schneider, A. Sluijs, H. Takata, J. Tian, A. Tsujimoto, B. S. Wade, T. Westerhold, R. Wilkens, T. Williams, P. A. Wilson, Y. Yamamoto, S. Yamamoto, T. Yamazaki, and R. E. Zeebe (2012), A Cenozoic record of the equatorial Pacific carbonate compensation depth, *Nature*, *488*(7413), 609–614.

Parrenin, F., J.-M. Barnola, J. Beer, T. Blunier, E. Castellano, J. Chappellaz, G. Dreyfus, H. Fischer, S. Fujita, J. Jouzel, K. Kawamura, B. Lemieux-Dudon, L. Louler-

gue, V. Masson-Delmotte, B. Narcisi, J.-R. Petit, G. Raisbeck, D. Raynaud, U. Ruth, J. Schwander, M. Severi, R. Spahni, J. P. Steffensen, A. Svensson, R. Udisti, C. Waelbroeck, and E. Wolff (2007), The EDC3 chronology for the EPICA Dome C ice core, *Climate of the Past*, *3*(3), 485–497.

Peck, V. L., J. Yu, S. Kender, and C. R. Riesselman (2010), Shifting ocean carbonate chemistry during the Eocene–Oligocene climate transition: Implications for deep-ocean Mg/Ca paleothermometry, *Paleoceanography*, *25*(4), PA4219, doi: 10.1029/2009PA001906.

Pekar, S. F., N. Christie-Blick, M. A. Kominz, and K. G. Miller (2002), Calibration between eustatic estimates from backstripping and oxygen isotopic records for the Oligocene, *Geology*, *30*(10), 903–906.

Pekar, S. F., A. Hucks, M. Fuller, and S. Li (2005), Glacioeustatic changes in the early and middle Eocene (51–42 Ma): Shallow-water stratigraphy from ODP Leg 189 Site 1171 (South Tasman Rise) and deep-sea δ^{18}O records, *Geological Society of America Bulletin*, *117*(7–8), 1081–1093.

Percival, D. B., and A. T. Walden (1993), *Spectral Analysis for Physical Applications: Multitaper and Conventional Univariate Techniques*, 583 pp., Cambridge University Press, Cambridge.

Pollard, D., and R. M. DeConto (2005), Hysteresis in Cenozoic Antarctic ice-sheet variations, *Global and Planetary Change*, *45*(1–3), 9–21.

Popper, K. (1935), *Logik der Forschung: Zur Erkenntnistheorie der modernen Naturwissenschaft*, 248 pp., Julius Springer, Wien.

Prentice, M. L., and R. K. Matthews (1988), Cenozoic ice-volume history: Development of a composite oxygen isotope record, *Geology*, *16*(11), 963–966.

Prentice, M. L., and R. K. Matthews (1991), Tertiary ice sheet dynamics: The snow gun hypothesis, *Journal of Geophysical Research*, *96*(B4), 6811–6827.

Press, F., and R. Siever (1986), *Earth*, fourth ed., 656 pp., Freeman, New York.

Priestley, M. B. (1981), *Spectral Analysis and Time Series*, 890 pp., Academic Press, London.

Pross, J., L. Contreras, P. K. Bijl, D. R. Greenwood, S. M. Bohaty, S. Schouten, J. A. Bendle, U. Röhl, L. Tauxe, J. I. Raine, C. E. Huck, T. van de Flierdt, S. S. R. Jamieson, C. E. Stickley, B. van de Schootbrugge, C. Escutia, H. Brinkhuis, and Integrated Ocean Drilling Program Expedition 318 Scientists (2012), Persistent near-tropical warmth on the Antarctic continent during the early Eocene epoch, *Nature*, *488*(7409), 73–77.

Prothero, D. R., L. C. Ivany, and E. A. Nesbitt (Eds.) (2003), *From Greenhouse to Icehouse: The Marine Eocene–Oligocene Transition*, 541 pp., Columbia University Press, New York.

Pusz, A. E., R. C. Thunell, and K. G. Miller (2011), Deep water temperature, carbonate ion, and ice volume changes across the Eocene–Oligocene climate transition, *Paleoceanography*, *26*(2), PA2205, doi:10.1029/2010PA001950.

Raymo, M. E. (1994), The Himalayas, organic carbon burial, and climate in the Miocene, *Paleoceanography*, *9*(3), 399–404.

Röhl, U., T. Westerhold, T. J. Bralower, and J. C. Zachos (2007), On the duration of the Paleocene–Eocene Thermal Maximum (PETM), *Geochemistry, Geophysics, Geosys-*

tems, *8*(12), Q12002, doi:10.1029/2007GC001784.

Rose, B. E. J., and D. Ferreira (2013), Ocean heat transport and water vapor greenhouse in a warm equable climate: A new look at the low gradient paradox, *Journal of Climate*, *26*(6), 2117–2136.

Rosenthal, Y., C. H. Lear, D. W. Oppo, and B. K. Linsley (2006), Temperature and carbonate ion effects on Mg/Ca and Sr/Ca ratios in benthic foraminifera: Aragonitic species *Hoeglundina elegans*, *Paleoceanography*, *21*(1), PA1007, doi: 10.1029/2005PA001158.

Ruddiman, W. F., and J. E. Kutzbach (1990), Late Cenozoic plateau uplift and climate change, *Transactions of the Royal Society of Edinburgh, Earth Sciences*, *81*, 301–314.

Ruddiman, W. F., M. E. Raymo, W. L. Prell, and J. E. Kutzbach (1997), The uplift–climate connection: A synthesis, in *Tectonic Uplift and Climate Change*, edited by W. F. Ruddiman, pp. 471–515, Plenum, New York.

Rue, H., and L. Held (2005), *Gaussian Markov Random Fields: Theory and Applications*, 263 pp., Chapman and Hall, Boca Raton, F. L.

Saltzman, B. (2002), *Dynamical Paleoclimatology: Generalized Theory of Global Climate Change*, 354 pp., Academic Press, San Diego.

Salzmann, U., A. M. Dolan, A. M. Haywood, W.-L. Chan, J. Voss, D. J. Hill, A. Abe-Ouchi, B. Otto-Bliesner, F. J. Bragg, M. A. Chandler, C. Contoux, H. J. Dowsett, A. Jost, Y. Kamae, G. Lohmann, D. J. Lunt, S. J. Pickering, M. J. Pound, G. Ramstein, N. A. Rosenbloom, L. Sohl, C. Stepanek, H. Ueda, and Z. Zhang (2013), Challenges in quantifying Pliocene terrestrial warming revealed by data–model discord, *Nature*

Climate Change, *3*(11), 969–974.

Sarnthein, M., K. Winn, S. J. A. Jung, J.-C. Duplessy, L. Labeyrie, H. Erlenkeuser, and G. Ganssen (1994), Changes in East Atlantic deepwater circulation over the last 30,000 years: Eight time slice reconstructions, *Paleoceanography*, *9*(2), 209–267.

Schmidt, G. A. (2010), Enhancing the relevance of palaeoclimate model/data comparisons for assessments of future climate change, *Journal of Quaternary Science*, *25*(1), 79–87.

Schmidt, G. A., J. D. Annan, P. J. Bartlein, B. I. Cook, E. Guilyardi, J. C. Hargreaves, S. P. Harrison, M. Kageyama, A. N. LeGrande, B. Konecky, S. Lovejoy, M. E. Mann, V. Masson-Delmotte, C. Risi, D. Thompson, A. Timmermann, L.-B. Tremblay, and P. Yiou (2014), Using palaeo-climate comparisons to constrain future projections in CMIP5, *Climate of the Past*, *10*(1), 221–250.

Scholz, D., and D. Hoffmann (2011), StalAge – an algorithm designed for construction of speleothem age models, *Quaternary Geochronology*, *6*(3–4), 369–382.

Schulz, M., and M. Mudelsee (2002), REDFIT: Estimating red-noise spectra directly from unevenly spaced paleoclimatic time series, *Computers and Geosciences*, *28*(3), 421–426.

Seibold, E., and W. H. Berger (1996), *The Sea Floor: An Introduction to Marine Geology*, third ed., 356 pp., Springer, Berlin.

Sexton, P. F., R. D. Norris, P. A. Wilson, H. Pälike, T. Westerhold, U. Röhl, C. T. Bolton, and S. Gibbs (2011), Eocene global warming events driven by ventilation of oceanic dissolved organic carbon, *Nature*, *471*(7338), 349–352.

Shackleton, N. J. (1982), The deep-sea sediment record of climate variability, *Progress in Oceanography*, *11*(2), 199–218.

Shackleton, N. J., and M. A. Hall (1984), Oxygen and carbon isotope stratigraphy of Deep Sea Drilling Project hole 552A: Plio–Pleistocene glacial history, in *Init. Repts. DSDP*, vol. 81, edited by D. G. Roberts et al., pp. 599–609, U.S. Govt. Printing Office, Washington, D. C.

Shackleton, N. J., and J. P. Kennett (1975), Paleotemperature history of the Cenozoic and the initiation of Antarctic glaciation: Oxygen and carbon isotope analyses in DSDP Sites 277, 279, and 281, in *Init. Repts. DSDP*, vol. 29, edited by J. P. Kennett et al., pp. 743–755, U.S. Govt. Printing Office, Washington, D. C.

Shackleton, N. J., M. A. Hall, and A. Boersma (1984), Oxygen and carbon isotope data from Leg 74 foraminifers, in *Init. Repts. DSDP*, vol. 74, edited by T. C. Moore Jr. et al., pp. 599–612, U.S. Govt. Printing Office, Washington, D. C.

Shevenell, A. E., and J. P. Kennett (2007), Cenozoic Antarctic cryosphere evolution: Tales from deep-sea sedimentary records, *Deep-Sea Research II*, *54*(21–22), 2308–2324.

Shevenell, A. E., J. P. Kennett, and D. W. Lea (2004), Middle Miocene Southern Ocean cooling and Antarctic cryosphere expansion, *Science*, *305*(5691), 1766–1770.

Shevenell, A. E., J. P. Kennett, and D. W. Lea (2008), Middle Miocene ice sheet dynamics, deep-sea temperatures, and carbon cycling: A Southern Ocean perspective, *Geochemistry, Geophysics, Geosystems*, *9*(2), Q02006, doi:10.1029/2007GC001736.

Sijp, W. P., M. H. England, and J. R. Toggweiler (2009), Effect of ocean gateway changes under greenhouse warmth, *Journal of Climate*, *22*(24), 6639–6652.

Sijp, W. P., M. H. England, and M. Huber (2011), Effect of the deepening of the Tasman Gateway on the global ocean, *Paleoceanography*, *26*(4), PA4207, doi:

10.1029/2011PA002143.

Solomon, S., D. Qin, M. Manning, M. Marquis, K. Averyt, M. M. B. Tignor, H. L. Miller Jr., and Z. Chen (Eds.) (2007), *Climate Change 2007: The Physical Science Basis. Contribution of Working Group I to the Fourth Assessment Report of the Intergovernmental Panel on Climate Change*, 996 pp., Cambridge University Press, Cambridge.

St. John, K. (2008), Cenozoic ice-rafting history of the central Arctic Ocean: Terrigenous sands on the Lomonosov Ridge, *Paleoceanography*, *23*(1), PA1S05, doi: 10.1029/2007PA001483.

Stanley, H. E. (1971), *Introduction to Phase Transitions and Critical Phenomena*, 308 pp., Oxford University Press, New York.

Stanley, S. M. (1989), *Earth and life through time*, second ed., 689 pp., Freeman, New York.

Steph, S., R. Tiedemann, M. Prange, J. Groeneveld, D. Nürnberg, L. Reuning, M. Schulz, and G. H. Haug (2006), Changes in Caribbean surface hydrography during the Pliocene shoaling of the Central American Seaway, *Paleoceanography*, *21*(4), PA4221, doi: 10.1029/2004PA001092.

Stocker, T. F., D. Qin, G.-K. Plattner, M. M. B. Tignor, S. K. Allen, J. Boschung, A. Nauels, Y. Xia, V. Bex, and P. M. Midgley (Eds.) (2013), *Climate Change 2013: The Physical Science Basis. Working Group I Contribution to the Fifth Assessment Report of the Intergovernmental Panel on Climate Change*, 1535 pp., Cambridge University Press, Cambridge.

Stott, L. D., J. P. Kennett, N. J. Shackleton, and R. M. Corfield (1990), The evolution of Antarctic surface waters during the Paleogene: Inferences from the stable isotopic composition of planktonic foraminifers, ODP Leg 113, in *Proc. ODP, Sci. Results*, vol. 113, edited by P. F. Barker et al., pp. 849–863, Ocean Drilling Program, College Station, T. X.

Tingley, M. P., P. F. Craigmile, M. Haran, B. Li, E. Mannshardt, and B. Rajaratnam (2012), Piecing together the past: Statistical insights into paleoclimatic reconstructions, *Quaternary Science Reviews*, *35*, 1–22.

Tripati, A., and H. Elderfield (2005), Deep-sea temperature and circulation changes at the Paleocene–Eocene Thermal Maximum, *Science*, *308*(5730), 1894–1898.

Tripati, A., J. Backman, H. Elderfield, and P. Ferretti (2005), Eocene bipolar glaciation associated with global carbon cycle changes, *Nature*, *436*(7049), 341–346.

Tripati, A. K., R. A. Eagle, A. C. Morton, J. A. Dowdeswell, K. L. Atkinson, Y. Bahé, C. F. Dawber, E. Khadun, R. M. H. Shaw, O. Shorttle, and L. Thanabalasundaram (2008), Evidence for glaciation in the northern hemisphere back to 44 Ma from ice-rafted debris in the Greenland Sea, *Earth and Planetary Science Letters*, *265*(1–2), 112–122.

Tripati, A. K., C. D. Roberts, and R. A. Eagle (2009), Coupling of CO_2 and ice sheet stability over major climate transitions of the last 20 million years, *Science*, *326*(5958), 1394–1397.

Tripati, A. K., R. A. Eagle, N. Thiagarajan, A. C. Gagnon, H. Bauch, P. R. Halloran, and J. M. Eiler (2010), ^{13}C–^{18}O isotope signatures and 'clumped isotope' thermometry in foraminifera and coccoliths, *Geochimica et Cosmochimica Acta*, *74*(20), 5697–5717.

Valdes, P. (2011), Built for stability, *Nature Geoscience*, *4*(7), 414–416.

van Andel, T. H. (1975), Mesozoic/Cenozoic calcite compensation depth and the global distribution of calcareous sediments, *Earth and Planetary Science Letters*, *26*(2), 187–194.

Vincent, E., and W. H. Berger (1985), Carbon dioxide and polar cooling in the Miocene: The Monterey hypothesis, in *The Carbon Cycle and Atmospheric CO_2: Natural Variations Archean to Present*, edited by E. T. Sundquist and W. S. Broecker, pp. 455–468, American Geophysical Union, Washington, D. C.

Vincent, E., J. S. Killingley, and W. H. Berger (1985), Miocene oxygen and carbon isotope stratigraphy of the tropical Indian Ocean, in *The Miocene Ocean: Paleoceanography and Biogeography*, edited by J. P. Kennett, pp. 103–130, Geological Society of America, Boulder, C. O.

von der Heydt, A., and H. A. Dijkstra (2006), Effect of ocean gateways on the global ocean circulation in the late Oligocene and early Miocene, *Paleoceanography*, *21*(1), PA1011, doi:10.1029/2005PA001149.

von Storch, H., and F. W. Zwiers (1999), *Statistical Analysis in Climate Research*, 484 pp., Cambridge University Press, Cambridge.

Wasserman, L. (2004), *All of Statistics: A Concise Course in Statistical Inference*, 442 pp., Springer, New York.

Westerhold, T., U. Röhl, J. Laskar, I. Raffi, J. Bowles, L. J. Lourens, and J. C. Zachos (2007), On the duration of magnetochrons C24r and C25n and the timing of early Eocene global warming events: Implications from the Ocean Drilling Program Leg 208 Walvis

Ridge depth transect, *Paleoceanography*, *22*(2), PA2201, doi:10.1029/2006PA001322.

Westerhold, T., U. Röhl, H. Pälike, R. Wilkens, P. A. Wilson, and G. Acton (2014), Orbitally tuned timescale and astronomical forcing in the middle Eocene to early Oligocene, *Climate of the Past*, *10*(3), 955–973.

Willeit, M., A. Ganopolski, and G. Feulner (2013), On the effect of orbital forcing on mid-Pliocene climate, vegetation and ice sheets, *Climate of the Past*, *9*(4), 1749–1759.

Wilson, D. S., D. Pollard, R. M. DeConto, S. S. R. Jamieson, and B. P. Luyendyk (2013), Initiation of the West Antarctic Ice Sheet and estimates of total Antarctic ice volume in the earliest Oligocene, *Geophysical Research Letters*, *40*(16), 4305–4309, doi:10.1002/grl.50797.

Wright, J. D., K. G. Miller, and R. G. Fairbanks (1992), Early and middle Miocene stable isotopes: Implications for deepwater circulation and climate, *Paleoceanography*, *7*(3), 357–389.

Wunsch, C. (2003), The spectral description of climate change including the 100 ky energy, *Climate Dynamics*, *20*(4), 353–363.

Yang, S., E. Galbraith, and J. Palter (2013), Coupled climate impacts of the Drake Passage and the Panama Seaway, *Climate Dynamics*, doi:10.1007/s00382-013-1809-6.

You, Y., M. Huber, R. D. Müller, C. J. Poulsen, and J. Ribbe (2009), Simulation of the Middle Miocene Climate Optimum, *Geophysical Research Letters*, *36*(4), L04702, doi:10.1029/2008GL036571.

Yu, J., G. L. Foster, H. Elderfield, W. S. Broecker, and E. Clark (2010), An evaluation of benthic foraminiferal B/Ca and δ^{11}B for deep ocean carbonate ion and pH reconstruc-

tions, *Earth and Planetary Science Letters*, *293*(1–2), 114–120.

Zachos, J., M. Pagani, L. Sloan, E. Thomas, and K. Billups (2001a), Trends, rhythms, and aberrations in global climate 65 Ma to present, *Science*, *292*(5517), 686–693.

Zachos, J. C., J. R. Breza, and S. W. Wise (1992), Early Oligocene ice-sheet expansion on Antarctica: Stable isotope and sedimentological evidence from Kerguelen Plateau, southern Indian Ocean, *Geology*, *20*(6), 569–573.

Zachos, J. C., T. M. Quinn, and K. A. Salamy (1996), High-resolution (10^4 years) deep-sea foraminiferal stable isotope records of the Eocene–Oligocene climate transition, *Paleoceanography*, *11*(3), 251–266.

Zachos, J. C., B. P. Flower, and H. Paul (1997), Orbitally paced climate oscillations across the Oligocene/Miocene boundary, *Nature*, *388*(6642), 567–570.

Zachos, J. C., N. J. Shackleton, J. S. Revenaugh, H. Pälike, and B. P. Flower (2001b), Climate response to orbital forcing across the Oligocene–Miocene boundary, *Science*, *292*(5515), 274–278.

Zachos, J. C., G. R. Dickens, and R. E. Zeebe (2008), An early Cenozoic perspective on greenhouse warming and carbon-cycle dynamics, *Nature*, *451*(7176), 279–283.

Zahn, R., K. Winn, and M. Sarnthein (1986), Benthic foraminiferal δ^{13}C and accumulation rates of organic carbon: *Uvigerina peregrina* group and *Cibicidoides wuellerstorfi*, *Paleoceanography*, *1*(1), 27–42.

Zeebe, R. E., and J. C. Zachos (2013), Long-term legacy of massive carbon input to the Earth system: Anthropocene versus Eocene, *Philosophical Transactions of the Royal Society of London, Series A*, *371*(2001), 20120006, doi:10.1098/rsta.2012.0006.

Zhisheng, A., J. E. Kutzbach, W. L. Prell, and S. C. Porter (2001), Evolution of Asian monsoons and phased uplift of the Himalaya–Tibetan plateau since late Miocene times, *Nature*, *411*(6833), 62–66.

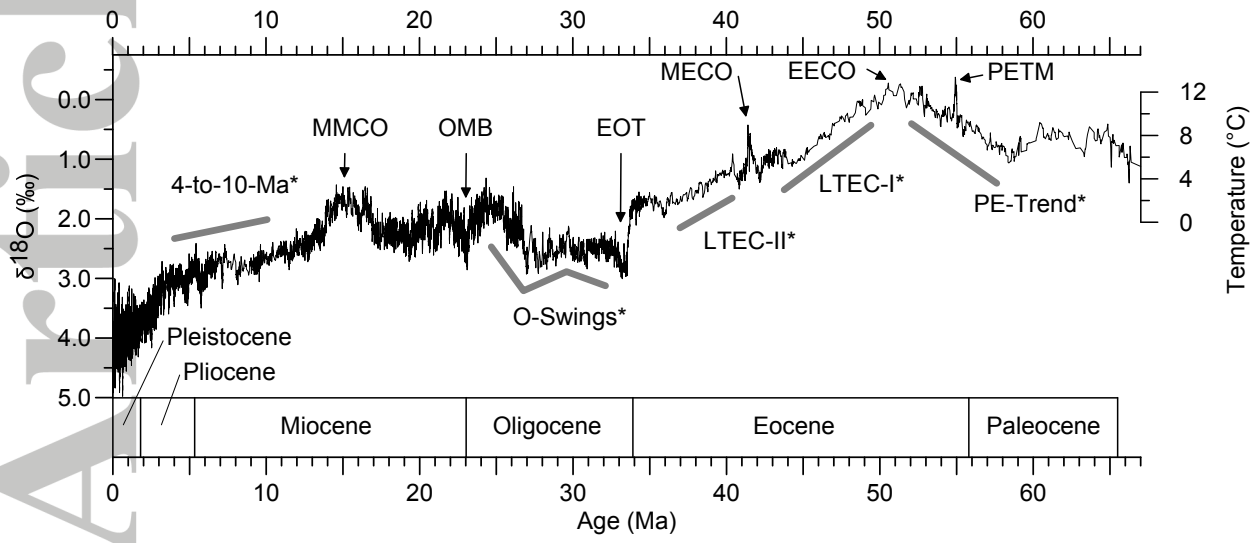

Figure 1. Cenozoic climate evolution. The proxy of oxygen isotopic composition (δ^{18}O) obtained from benthic foraminiferal shells found in marine sediment cores [*Zachos et al.*, 2001a] indicates changes in global ice volume (from around 34 Ma) and bottom-water temperature; heavier δ^{18}O values reflecting more ice/lower temperatures. The δ^{18}O values are adjusted to the genus *Cibicidoides* and 0.64 ‰ added [*Shackleton and Hall*, 1984; *Zachos et al.*, 2001a]. The record is a stack based on data from several drill sites and smoothed by means of a five-point running mean. The timescale of the δ^{18}O stack is after *Berggren et al.* [1995], while the boundaries of the Cenozoic epochs are after *Gradstein et al.* [2004]. The temperature axis [*Zachos et al.*, 2001a] was computed on the basis of an ice-free ocean; it applies to the time before the start of the EOT glaciation (about 34 Ma; see Table 8). The analyzed transitions and events are: Paleocene–Eocene warming trend (PE-Trend), Paleocene–Eocene Thermal Maximum (PETM), Long-term Eocene Cooling I (LTEC-I), Long-term Eocene Cooling II (LTEC-II), Eocene–Oligocene Transition (EOT), the Oligocene "swinging" trends (O-Swings), Oligocene–Miocene Boundary (OMB), Mid-Miocene Climatic Optimum (MMCO), and interval from 4 to 10 Ma (4-to-10-Ma); the Early Eocene Climatic Optimum (EECO) is not analyzed separately but in its relation with PE-Trend and LTEC-I; likewise the Mid-Eocene Climatic Optimum (MECO) is analyzed in its relation with LTEC-I and LTEC-II. Some transitions and events (asterisked) have not yet been explicitly named in the literature.

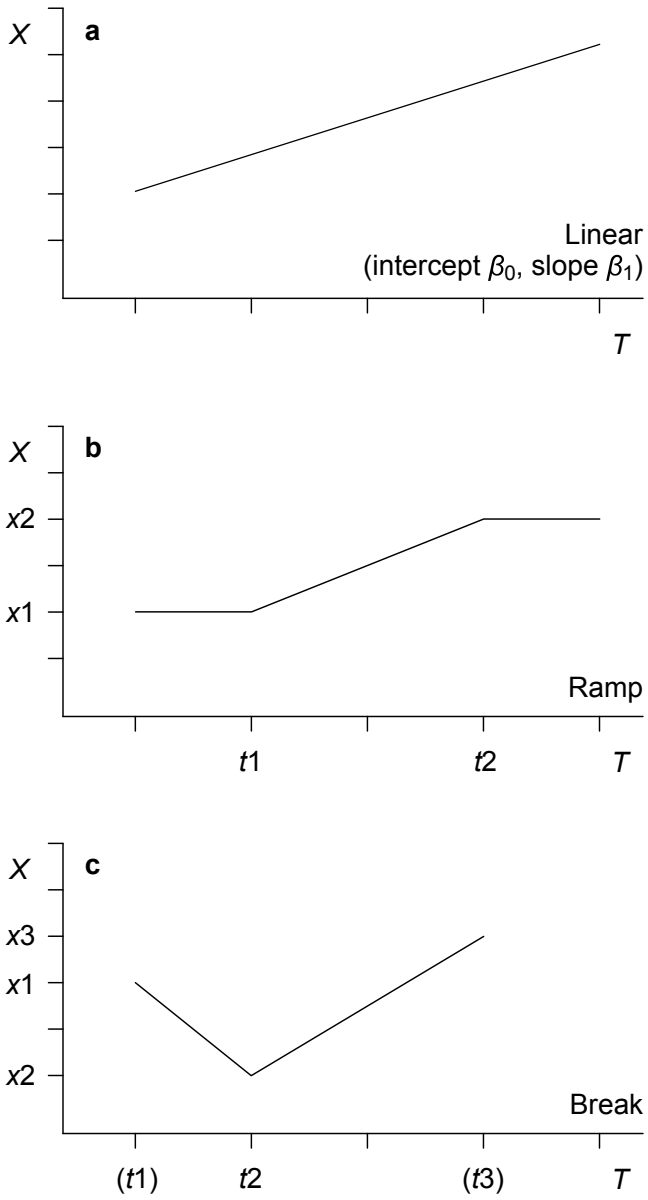

Figure 2. Regression models. The linear model (a) has two parameters (intercept, slope), the ramp model (b) has four parameters, and the break model (c) has four parameters ($t1$ is constrained as left, $t3$ as right bound of the time interval).

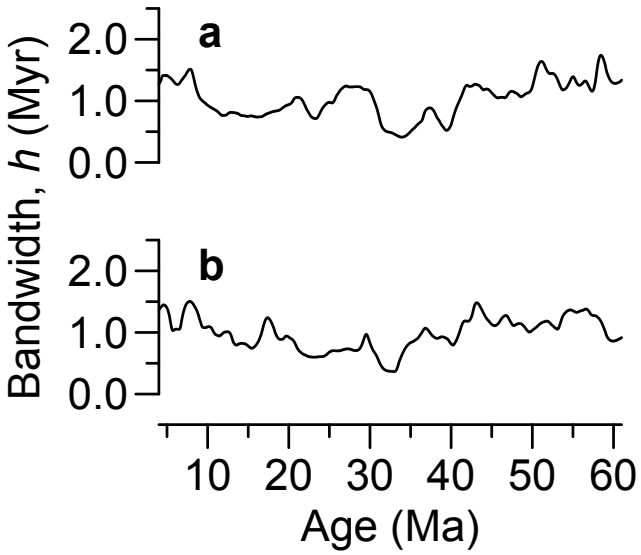

Figure 3. Stack construction, optimized adaptive kernel bandwidths (a, low latitudes; b, high latitudes).

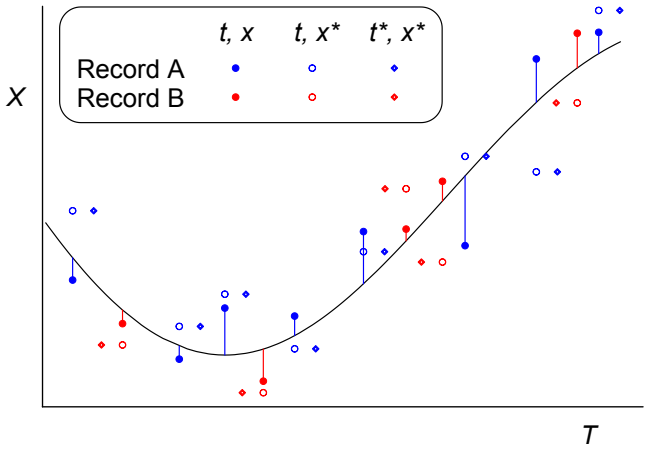

Figure 4. Stack construction, bootstrap resampling. Kernel regression is fitted (black line) to the data points (t, x), which are shown for two hypothetical records, A (blue symbols) and B (red symbols). ARB resampling is applied to the residuals (vertical lines connecting data and fit), yielding a first version of the resamples (t, x^*). Timescale simulation is applied to all values of a record simultaneously, but independent between records, yielding the final version of the resamples (t^*, x^*).

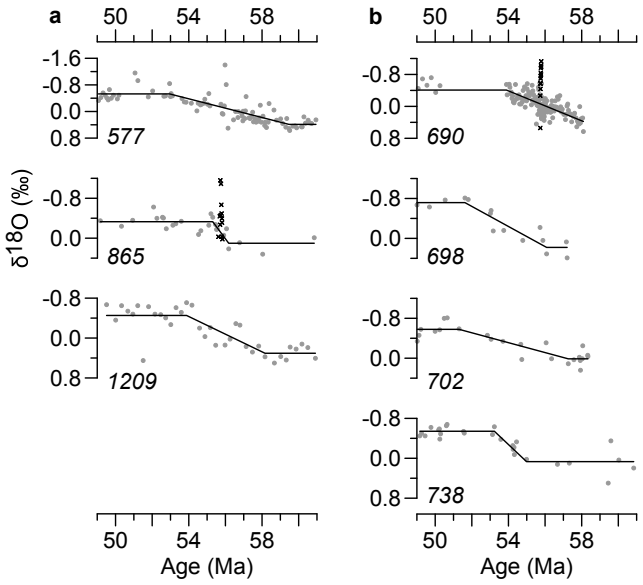

Figure 5. Results, climate transition PE-Trend (a, low latitudes; b, high latitudes). Fitted regressions (solid black lines) to time series (gray dots) are shown for individual data sets (DSDP/ODP/IODP site numbers in italics). Note that for ODP 690 and ODP 865, twelve and thirteen "outlier" values (crosses), respectively, corresponding to the climate event PETM (Figure 6), were excluded from the fitting procedure. See Table 4 for numerical results.

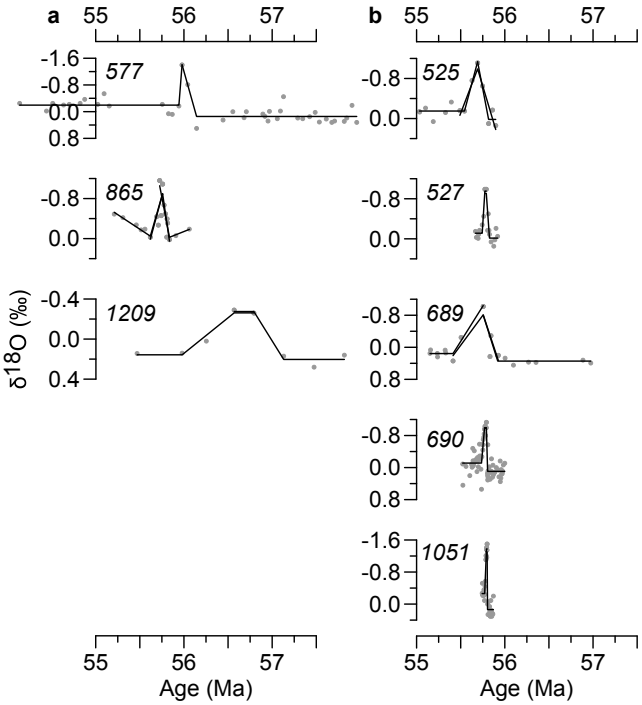

Figure 6. Results, climate event PETM (a, low latitudes; b, high latitudes); cf. Figure 5. This climate event was decribed by a combination of regression models (ramp–ramp for DSDP 527, DSDP 577, ODP 690, ODP 1051, and ODP 1209; ramp–break–ramp for DSDP 525 and ODP 689; and break–break–break for ODP 865). See Table 5 for numerical results. Note that for DSDP 577 and ODP 1209 the fit range is larger than the shown time-axis range.

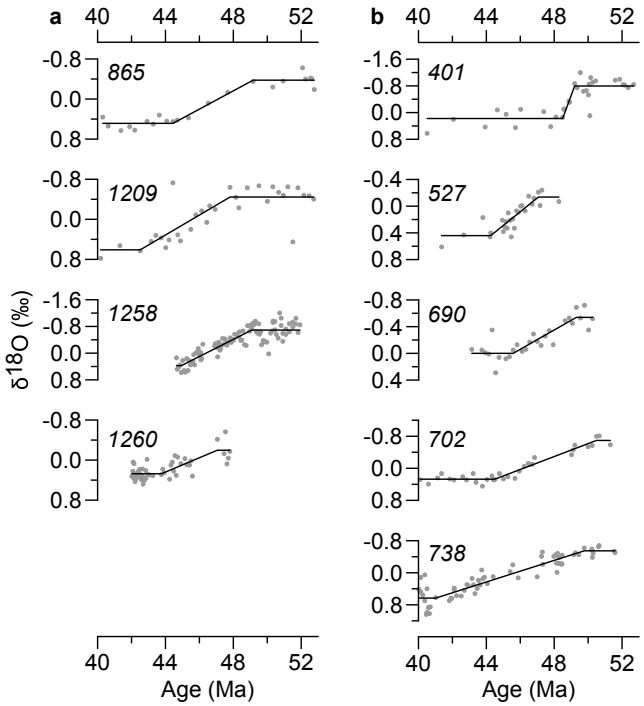

Figure 7. Results, climate transition LTEC-I (a, low latitudes; b, high latitudes); cf. Figure 5. See Table 6 for numerical results.

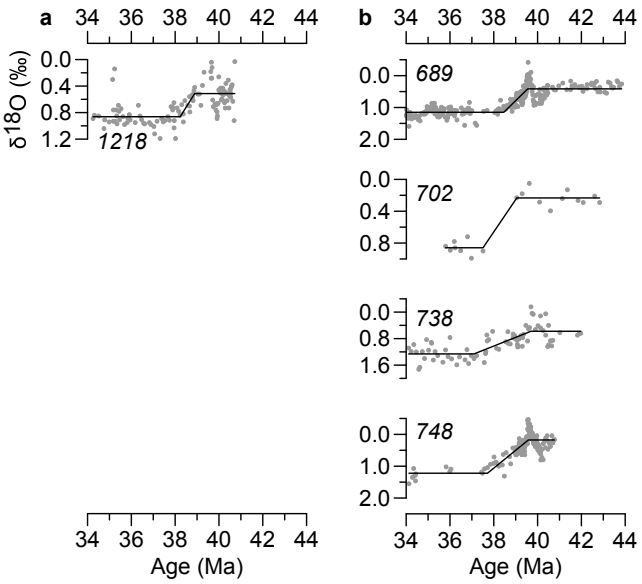

Figure 8. Results, climate transition LTEC-II (a, low latitudes; b, high latitudes); cf. Figure 5. See Table 7 for numerical results.

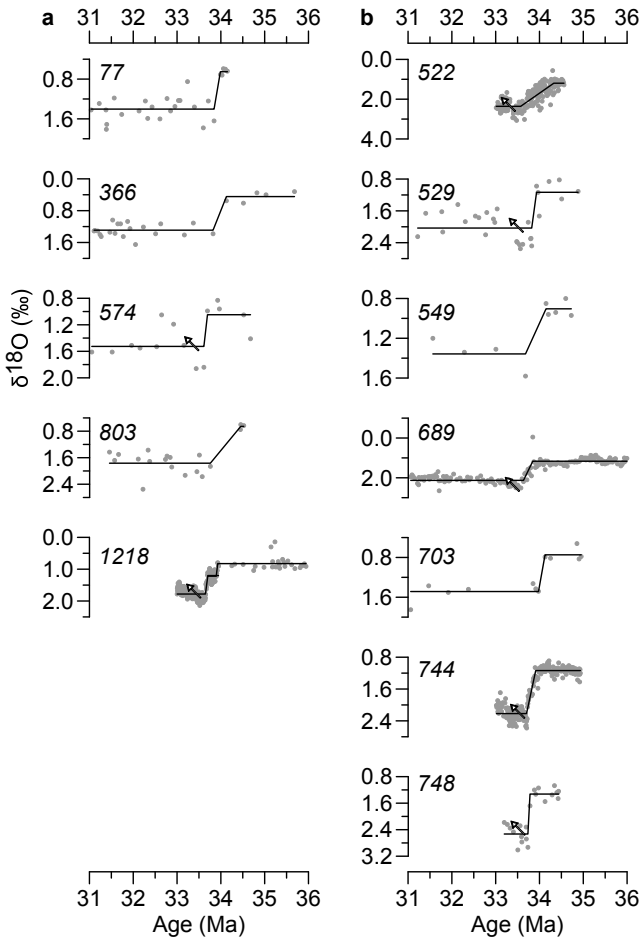

Figure 9. Results, Eocene–Oligocene Transition (EOT) (a, low latitudes; b, high latitudes); cf. Figure 5. For ODP 1218, the transition is statistically modeled as a two-step change [*Coxall et al.*, 2005]. Arrows indicate "overshoot" behavior. See Table 8 for numerical results.

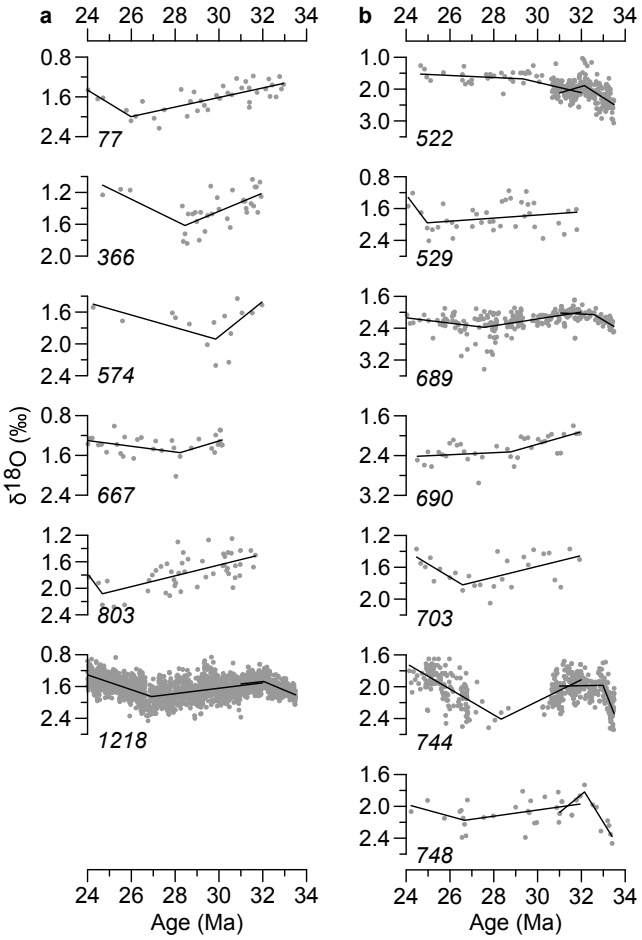

Figure 10. Results, Oligocene swinging trends (O-Swings) (a, low latitudes; b, high latitudes); cf. Figure 5. Note that this interval is analyzed in two parts (early and late). See Tables 9 and 10 for numerical results.

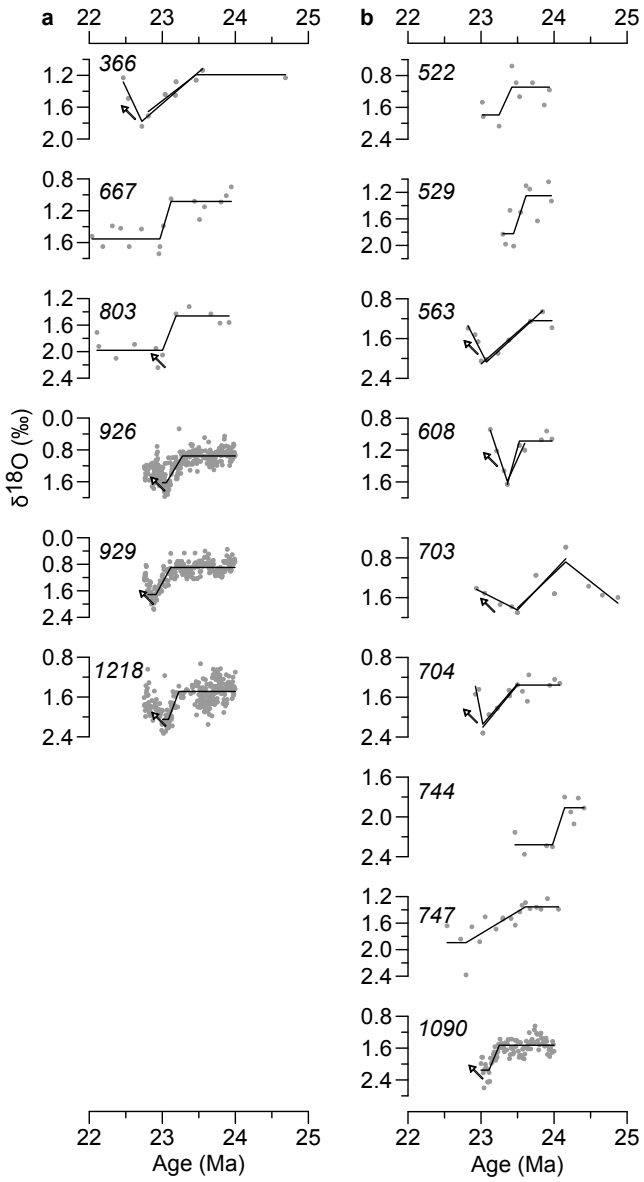

Figure 11. Results, Oligocene–Miocene Boundary (OMB) (a, low latitudes; b, high latitudes); cf. Figure 5. Note that, due to lack of high-resolution data in the fit region, some regressions consist of a combination of a ramp and a break (DSDP 366, DSDP 563, DSDP 608, and ODP 704) or a combination of two breaks (ODP 703). Arrows indicate "overshoot" behavior. Note that for records ODP 926, ODP 929, and ODP 1218 the data values are plotted beyond the lower bound of the fit interval, to 22.75 Ma, to document the overshoots. See Table 11 for numerical results.

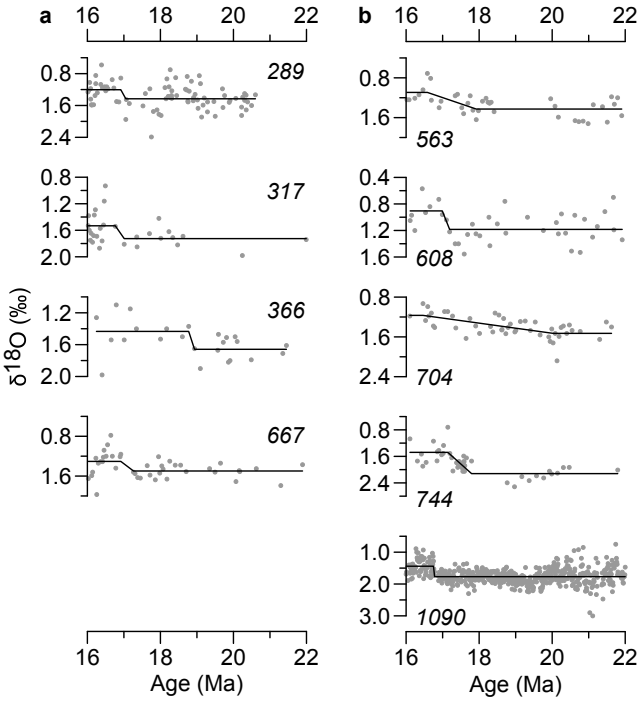

Figure 12. Results, climate transition MMCO-Start (a, low latitudes; b, high latitudes); cf. Figure 5. See Table 12 for numerical results.

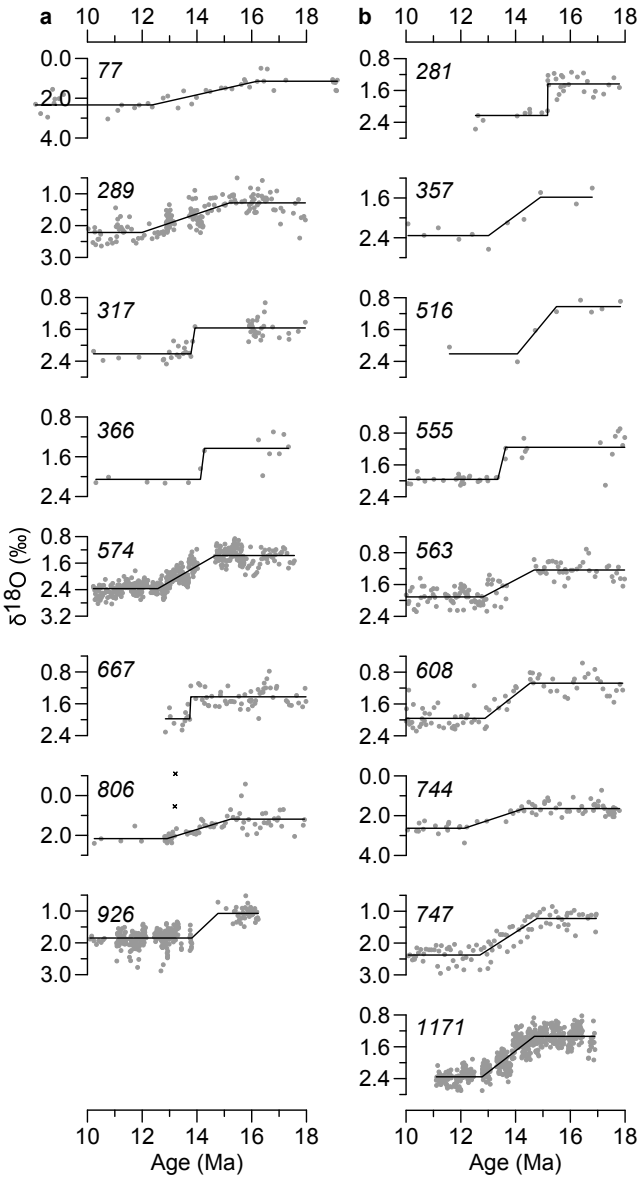

Figure 13. Results, Middle Miocene Climate Transition (MMCT) (a, low latitudes; b, high latitudes); cf. Figure 5. Note that for DSDP 77 the fit range was extended (8 to 19 Ma) owing to low resolution, and for ODP 806 two "outlier" values (crosses) were excluded from the fitting procedure. See Table 13 for numerical results.

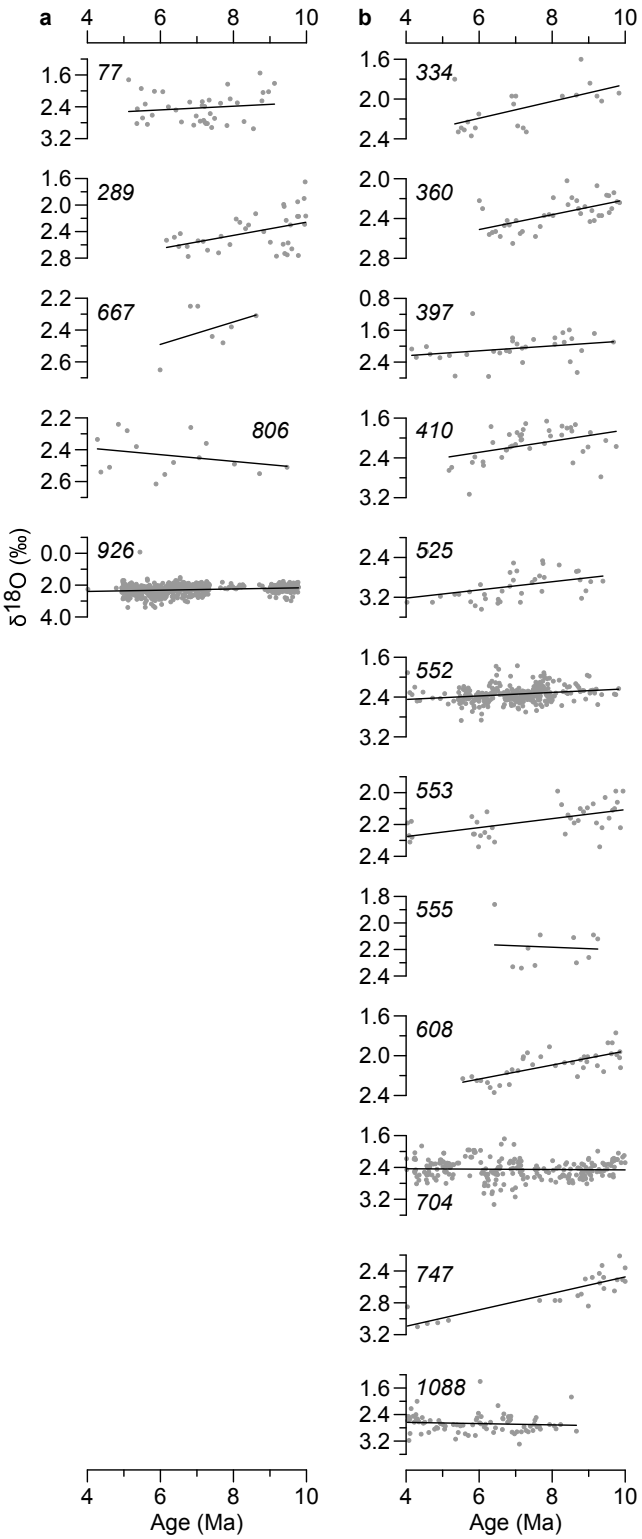

Figure 14. Results, climate transition 4-to-10-Ma (a, low latitudes; b, high latitudes); cf. Figure 5. See Table 14 for numerical results.

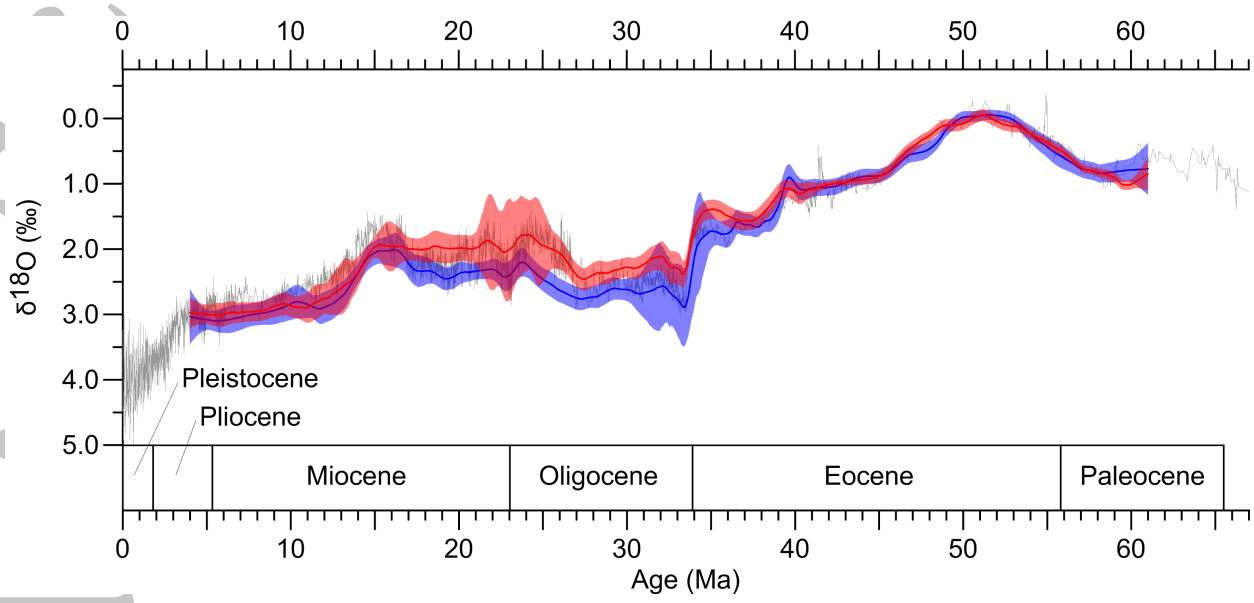

Figure 15. Cenozoic climate stacks (marine benthic δ^{18}O). Shown is Zachos et al.'s stack (gray line), which comprises data from low and high latitudes, the new stack from low-latitude data (red line) with uncertainty band (red shaded), and the new stack from high-latitude data (blue line) with uncertainty band (blue shaded). The δ^{18}O values are adjusted to the genus *Cibicidoides* and 0.64 ‰ added [*Shackleton and Hall*, 1984; *Zachos et al.*, 2001a]. For more details, see Figure 1 on Cenozoic climate, section 3.3 on stack construction, and section 4.3 on results interpretation.

Table 1. Database, Low-Latitude Records

Record	Geographical Position[a]	Water Depth[a] (m)	Time Interval (Ma)	Time Spacing	
				Average (kyr)	Maximum (kyr)
DSDP 77	0°N 133°W	4291	[5.1; 34.1]	207	1851
DSDP 289	0°N 159°E	2206	[6.2; 20.6]	55	529
DSDP 317	11°S 162°W	2560	[5.6; 23.3]	274	2289
DSDP 366	6°N 20°W	2853	[9.0; 35.7]	281	2381
DSDP 574	4°N 133°W	4561	[10.2; 34.7]	48	4747
DSDP 577	32°N 158°E	2675	[38.0; 60.9]	246	5907
ODP 667	5°N 22°W	3529	[6.0; 30.2]	171	1950
ODP 803	2°N 161°E	3422	[16.3; 34.5]	198	2981
ODP 806	0°N 159°E	2520	[4.3; 19.2]	127	847
ODP 865	18°N 180°W	1517	[36.0; 60.9]	444	2816
ODP 926	4°N 43°W	3598	[4.0; 26.9]	7	1434
ODP 929	6°N 44°W	4356	[15.1; 25.1]	17	2180
ODP 1209	33°N 159°E	2387	[37.7; 60.9]	401	1428
ODP 1218	9°N 135°W	4828	[19.0; 41.0]	7	373
IODP 1258	9°N 55°W	3192	[44.6; 53.8]	64	697
IODP 1260	9°N 55°W	2549	[39.4; 47.8]	70	1470

[a] For paleogeographical position and paleo water depth, see *Cramer et al.* [2009].

[b] For references of δ^{18}O data, see *Cramer et al.* [2009, auxiliary material 2008pa001683-ds01.txt therein]; for references and methods of timescale construction, see section 2.3.

Table 2. Database, High-Latitude Records

Record	Geographical Position[a]	Water Depth[a] (m)	Time Interval (Ma)	Time Spacing Average (kyr)	Time Spacing Maximum (kyr)
DSDP 281	48°S 148°E	1591	[7.9; 20.6]	236	3180
DSDP 334	37°N 34°W	2619	[5.3; 11.1]	251	986
DSDP 357	30°S 36°W	2086	[8.6; 21.5]	807	1610
DSDP 360	36°S 18°E	2949	[6.0; 23.8]	194	3111
DSDP 397	27°N 15°W	2900	[4.2; 9.7]	178	583
DSDP 401	47°N 9°W	2495	[34.9; 56.0]	351	1870
DSDP 410	46°N 29°W	2975	[5.2; 12.0]	148	542
DSDP 516	30°S 35°W	1313	[4.0; 20.9]	392	6539
DSDP 522	26°S 5°W	4441	[23.0; 34.6]	26	867
DSDP 525	29°S 3°E	2467	[4.0; 61.0]	227	19950
DSDP 527	28°S 2°E	4428	[4.1; 56.9]	894	22987
DSDP 529	29°S 3°E	3035	[21.5; 44.1]	279	7113
DSDP 549	49°N 13°W	2513	[24.0; 38.6]	768	1613
DSDP 552	56°N 23°W	2301	[4.0; 10.2]	21	348
DSDP 553	56°N 23°W	2328	[4.0; 23.6]	213	6918
DSDP 555	57°N 21°W	1659	[6.4; 18.4]	226	2683
DSDP 563	34°N 44°W	3786	[9.3; 32.7]	113	2047
DSDP 608	43°N 23°W	3526	[5.6; 24.2]	119	593
ODP 689	65°S 3°E	2080	[23.8; 57.0]	54	7281
ODP 690	65°S 1°E	2914	[24.5; 58.1]	131	4837
ODP 698	51°S 33°W	2138	[48.7; 57.2]	529	1210
ODP 702	51°S 26°W	3083	[35.8; 58.3]	382	2176
ODP 703	47°S 8°E	1796	[22.5; 37.0]	268	1475
ODP 704	47°S 7°E	2532	[4.0; 29.5]	74	5447
ODP 738	63°S 83°E	2253	[33.4; 60.8]	184	2125
ODP 744	62°S 81°E	2307	[10.0; 36.7]	40	1670
ODP 747	55°S 77°E	1697	[4.0; 26.7]	103	2495
ODP 748	58°S 79°E	1288	[23.7; 40.8]	63	1401
ODP 1051	30°N 76°W	1981	[36.6; 55.9]	85	18337
ODP 1088	41°S 14°E	2082	[4.0; 8.7]	54	296
ODP 1090	43°S 9°E	3702	[15.9; 24.2]	11	110
ODP 1171	48°S 149°E	2148	[11.1; 16.9]	10	292

[a] For paleogeographical position and paleo water depth, see *Cramer et al.* [2009].

[b] For references of δ^{18}O data, see *Cramer et al.* [2009, auxiliary material 2008pa001683-ds01.txt therein]; for references and methods of timescale construction, see section 2.3.

Table 3. Results[a] Persistence Time Estimation

Record	Persistence Time (Myr)	Record	Persistence Time (Myr)
	Low-Latitude Records		
DSDP 77	0.042 ± 0.019	ODP 806	0.027 ± 0.011
DSDP 289	0.010 ± 0.003	ODP 865	[c]
DSDP 317	0.066 ± 0.167	ODP 926	0.0037 ± 0.0002
DSDP 366	[c]	ODP 929	0.011 ± 0.001
DSDP 574	0.010 ± 0.001	ODP 1209	[c]
DSDP 577	0.055 ± 0.019	ODP 1218	0.0037 ± 0.0002
ODP 667	0.035 ± 0.013	IODP 1258	0.013 ± 0.007
ODP 803	[c]	IODP 1260	0.022 ± 0.007
Average[b]	$0.0040^{\pm 0.0005}_{\pm 0.0001}$		
	High-Latitude Records		
DSDP 281	0.060 ± 0.033	DSDP 563	0.021 ± 0.007
DSDP 334	0.084 ± 0.058	DSDP 608	[c]
DSDP 357	[c]	ODP 689	0.015 ± 0.002
DSDP 360	[c]	ODP 690	[c]
DSDP 397	[c]	ODP 698	0.206 ± 0.256
DSDP 401	[c]	ODP 702	0.095 ± 0.064
DSDP 410	0.039 ± 0.025	ODP 703	0.068 ± 0.046
DSDP 516	0.106 ± 0.817	ODP 704	0.013 ± 0.002
DSDP 522	0.004 ± 0.001	ODP 738	0.051 ± 0.016
DSDP 525	0.041 ± 0.011	ODP 744	0.012 ± 0.001
DSDP 527	[c]	ODP 747	[c]
DSDP 529	0.064 ± 0.029	ODP 748	0.025 ± 0.006
DSDP 549	[c]	ODP 1051	0.016 ± 0.027
DSDP 552	0.007 ± 0.001	ODP 1088	0.012 ± 0.006
DSDP 553	[c]	ODP 1090	0.009 ± 0.001
DSDP 555	[c]	ODP 1171	0.006 ± 0.001
Average[b]	$0.0085^{\pm 0.0009}_{\pm 0.0004}$		

[a] Values are rounded.

[b] Weighted average with external error (superscript) and internal error (subscript).

[c] No result (numerical minimization problem, boundary solution).

Table 4. Results[a], Climate Transition PE-Trend (cf. Figure 5)

Record	Start (Ma)	End (Ma)	Duration (Myr)	Midpoint (Ma)	δ^{18}O Amplitude[b] (‰)
			Low-Latitude Records		
DSDP 577	59.47 ± 0.78	52.95 ± 0.93	6.52 ± 1.40	56.21 ± 0.50	$+0.92 \pm 0.10$
ODP 865	56.18 ± 0.62	55.31 ± 0.49	0.87 ± 1.01	55.74 ± 0.23	$+0.43 \pm 0.07$
ODP 1209	58.16 ± 1.35	53.88 ± 1.07	4.28 ± 2.11	56.02 ± 0.61	$+0.76 \pm 0.12$
Average[c]	$57.54^{\pm 1.08}_{\pm 0.46}$	$54.65^{\pm 0.68}_{\pm 0.41}$	$3.01^{\pm 1.80}_{\pm 0.76}$	$55.86^{\pm 0.13}_{\pm 0.21}$	$+0.62^{\pm 0.15}_{\pm 0.05}$
			High-Latitude Records		
ODP 690	58.09 ± 0.34	53.89 ± 0.27	4.20 ± 0.48	55.99 ± 0.20	$+0.79 \pm 0.08$
ODP 698	56.08 ± 0.84	51.62 ± 0.91	4.46 ± 1.46	53.85 ± 0.48	$+0.90 \pm 0.13$
ODP 702	57.27 ± 1.14	51.31 ± 1.42	5.96 ± 2.18	54.29 ± 0.69	$+0.59 \pm 0.08$
ODP 738	54.99 ± 0.81	53.23 ± 0.59	1.76 ± 1.27	54.11 ± 0.31	$+0.61 \pm 0.07$
Average[c]	$57.39^{\pm 0.66}_{\pm 0.30}$	$53.53^{\pm 0.42}_{\pm 0.25}$	$4.02^{\pm 0.50}_{\pm 0.42}$	$55.15^{\pm 0.55}_{\pm 0.17}$	$+0.68^{\pm 0.06}_{\pm 0.04}$

[a] Values are rounded.

[b] Negative and positive amplitudes indicate glaciation/cooling and deglaciation/warming, respectively.

[c] Weighted average with external error (superscript) and internal error (subscript); start, end, and midpoint averages include dating-error effects.

Table 5. Results[a] Climate Event PETM (cf. Figure 6)

Record	Age (Ma)	Duration (Myr)		δ^{18}O Amplitude[b] (‰)	
		Start	End	Start	End
		Low-Latitude Records			
DSDP 577	55.98 ± 0.06	0.165 ± 0.047	0.036 ± 0.011	$+1.55 \pm 0.17$	-1.20 ± 0.14
ODP 865	55.76 ± 0.02	0.078 ± 0.041	0.139 ± 0.057	$+0.87 \pm 0.25$	-0.84 ± 0.19
ODP 1209	56.70 ± 0.11	0.338 ± 0.057	0.590 ± 0.061	$+0.48 \pm 0.04$	-0.42 ± 0.03
Average[c]	$56.03^{\pm 0.26}_{\pm 0.07}$	$0.165^{\pm 0.071}_{\pm 0.027}$	$0.055^{\pm 0.067}_{\pm 0.010}$	$+0.54^{\pm 0.17}_{\pm 0.04}$	$-0.46^{\pm 0.12}_{\pm 0.03}$
		High-Latitude Records			
DSDP 525	55.69 ± 0.03	0.124 ± 0.030	0.149 ± 0.030	$+1.01 \pm 0.13$	-0.84 ± 0.12
DSDP 527	55.78 ± 0.01	0.036 ± 0.016	0.030 ± 0.008	$+0.89 \pm 0.14$	-0.84 ± 0.08
ODP 689	55.76 ± 0.03	0.165 ± 0.048	0.342 ± 0.047	$+1.16 \pm 0.22$	-0.97 ± 0.21
ODP 690	55.79 ± 0.01	0.014 ± 0.004	0.035 ± 0.016	$+1.08 \pm 0.10$	-0.88 ± 0.11
ODP 1051	55.799 ± 0.002	0.005 ± 0.001	0.020 ± 0.003	$+1.44 \pm 0.07$	-1.11 ± 0.07
Average[c]	$55.76^{\pm 0.02}_{\pm 0.05}$	$0.006^{\pm 0.003}_{\pm 0.001}$	$0.025^{\pm 0.012}_{\pm 0.003}$	$+1.21^{\pm 0.11}_{\pm 0.05}$	$-0.96^{\pm 0.06}_{\pm 0.04}$

[a] Values are rounded.

[b] Negative and positive amplitudes indicate glaciation/cooling and deglaciation/warming, respectively.

[c] Weighted average with external error (superscript) and internal error (subscript); time averages include dating-error effects.

Table 6. Results[a] Climate Transition LTEC-I (cf. Figure 7)

Record	Start (Ma)	End (Ma)	Duration (Myr)	Midpoint (Ma)	δ^{18}O Amplitude[b] (‰)
			Low-Latitude Records		
ODP 865	49.17 ± 0.68	44.44 ± 0.53	4.73 ± 1.02	46.81 ± 0.34	-0.86 ± 0.05
ODP 1209	47.81 ± 1.39	42.51 ± 1.49	5.29 ± 2.47	45.16 ± 0.74	-1.05 ± 0.21
IODP 1258	49.08 ± 0.29	44.94 ± 0.37	4.15 ± 0.54	47.01 ± 0.19	-1.06 ± 0.08
IODP 1260	47.06 ± 0.90	43.76 ± 0.75	3.30 ± 1.48	45.41 ± 0.37	-0.47 ± 0.07
Average[c]	$48.88^{\pm 0.35}_{\pm 0.27}$	$44.55^{\pm 0.33}_{\pm 0.28}$	$4.22^{\pm 0.24}_{\pm 0.45}$	$46.59^{\pm 0.39}_{\pm 0.16}$	$-0.82^{\pm 0.12}_{\pm 0.04}$
			High-Latitude Records		
DSDP 401	49.20 ± 0.26	48.50 ± 0.25	0.71 ± 0.46	48.85 ± 0.11	-0.97 ± 0.10
DSDP 527	47.07 ± 0.57	44.26 ± 0.55	2.81 ± 0.92	45.66 ± 0.31	-0.58 ± 0.11
ODP 690	49.31 ± 0.75	45.58 ± 0.81	3.73 ± 1.34	47.44 ± 0.40	-0.54 ± 0.08
ODP 702	50.49 ± 0.51	44.50 ± 0.31	5.99 ± 0.67	47.50 ± 0.26	-0.97 ± 0.07
ODP 738	49.77 ± 0.94	41.02 ± 0.67	8.75 ± 1.25	45.39 ± 0.52	-1.18 ± 0.11
Average[c]	$49.17^{\pm 0.47}_{\pm 0.21}$	$46.08^{\pm 1.19}_{\pm 0.18}$	$2.96^{\pm 1.33}_{\pm 0.33}$	$47.96^{\pm 0.60}_{\pm 0.12}$	$-0.84^{\pm 0.12}_{\pm 0.04}$

[a] Values are rounded.

[b] Negative and positive amplitudes indicate glaciation/cooling and deglaciation/warming, respectively.

[c] Weighted average with external error (superscript) and internal error (subscript); start, end, and midpoint averages include dating-error effects.

Table 7. Results[a] Climate Transition LTEC-II (cf. Figure 8)

Record	Start (Ma)	End (Ma)	Duration (Myr)	Midpoint (Ma)	δ^{18}O Amplitude[b] (‰)
			Low-Latitude Records		
ODP 1218	38.89 ± 0.37	38.23 ± 0.36	0.66 ± 0.67	38.56 ± 0.15	-0.35 ± 0.04
			High-Latitude Records		
ODP 689	39.55 ± 0.20	38.45 ± 0.26	1.10 ± 0.41	39.00 ± 0.11	-0.74 ± 0.06
ODP 702	39.05 ± 0.18	37.51 ± 0.29	1.54 ± 0.36	38.28 ± 0.16	-0.63 ± 0.04
ODP 738	39.70 ± 0.87	37.10 ± 0.87	2.60 ± 1.47	38.40 ± 0.46	-0.68 ± 0.12
ODP 748	39.58 ± 0.30	37.71 ± 0.54	1.87 ± 0.72	38.65 ± 0.25	-1.04 ± 0.16
Average[c]	$39.34^{\pm 0.15}_{\pm 0.13}$	$38.00^{\pm 0.22}_{\pm 0.17}$	$1.44^{\pm 0.19}_{\pm 0.25}$	$38.70^{\pm 0.19}_{\pm 0.10}$	$-0.68^{\pm 0.05}_{\pm 0.03}$

[a] Values are rounded.

[b] Negative and positive amplitudes indicate glaciation/cooling and deglaciation/warming, respectively.

[c] Weighted average with external error (superscript) and internal error (subscript); start, end, and midpoint averages include dating-error effects.

Table 8. Results[a] Eocene–Oligocene Transition (EOT) (cf. Figure 9)

Record	Start (Ma)	End (Ma)	Duration (Myr)	Midpoint (Ma)	δ^{18}O Amplitude[b] (‰)
			Low-Latitude Records		
DSDP 77	33.99 ± 0.05	33.84 ± 0.09	0.14 ± 0.11	33.92 ± 0.04	-0.75 ± 0.12
DSDP 366	34.13 ± 0.16	33.82 ± 0.14	0.30 ± 0.28	33.97 ± 0.06	-0.84 ± 0.07
DSDP 574	33.69 ± 0.34	33.61 ± 0.49	0.08 ± 0.57	33.65 ± 0.31	-0.48 ± 0.16
ODP 803	34.45 ± 0.04	33.76 ± 0.25	0.69 ± 0.25	34.11 ± 0.12	-1.11 ± 0.18
ODP 1218[c]	33.93 ± 0.06	33.65 ± 0.02	0.28 ± 0.06	33.79 ± 0.03	-0.96 ± 0.04
Average[d]	$34.19^{\pm 0.12}_{\pm 0.03}$	$33.66^{\pm 0.02}_{\pm 0.02}$	$0.27^{\pm 0.05}_{\pm 0.05}$	$33.86^{\pm 0.04}_{\pm 0.02}$	$-0.91^{\pm 0.06}_{\pm 0.03}$
			High-Latitude Records		
DSDP 522	34.33 ± 0.08	33.57 ± 0.05	0.76 ± 0.11	33.95 ± 0.04	-1.16 ± 0.08
DSDP 529	33.93 ± 0.15	33.82 ± 0.11	0.11 ± 0.22	33.88 ± 0.08	-0.90 ± 0.16
DSDP 549	34.15 ± 0.15	33.68 ± 0.37	0.47 ± 0.44	33.92 ± 0.17	-0.45 ± 0.08
ODP 689	33.85 ± 0.05	33.64 ± 0.05	0.21 ± 0.09	33.74 ± 0.02	-0.96 ± 0.04
ODP 703	34.13 ± 0.06	33.98 ± 0.03	0.15 ± 0.08	34.05 ± 0.03	-0.74 ± 0.08
ODP 744	33.91 ± 0.03	33.70 ± 0.02	0.21 ± 0.04	33.81 ± 0.01	-1.08 ± 0.04
ODP 748	33.78 ± 0.04	33.74 ± 0.03	0.05 ± 0.06	33.76 ± 0.02	-1.21 ± 0.11
Average[d]	$33.99^{\pm 0.07}_{\pm 0.05}$	$33.74^{\pm 0.05}_{\pm 0.05}$	$0.21^{\pm 0.07}_{\pm 0.03}$	$33.86^{\pm 0.04}_{\pm 0.04}$	$-0.98^{\pm 0.07}_{\pm 0.02}$

[a] Values are rounded.

[b] Negative and positive amplitudes indicate glaciation/cooling and deglaciation/warming, respectively.

[c] For ODP 1218, the transition is statistically modeled as a two-step change [*Coxall et al.*, 2005]; the earlier step is estimated as from (33.93 ± 0.06 Ma, 0.82 ± 0.03‰) to (33.90 ± 0.02 Ma, 1.22 ± 0.02‰) and the later step as from (33.70 ± 0.03 Ma, 1.20 ± 0.06‰) to (33.65 ± 0.02 Ma, 1.78 ± 0.03‰).

[d] Weighted average with external error (superscript) and internal error (subscript); start, end, and midpoint averages include dating-error effects.

Table 9. Results[a] Oligocene Swinging Trends (O-Swings), Early Part (cf. Figure 10)

Record	Age (Ma)	Slope[b], Start (‰ Myr^{-1})	Slope[b], End (‰ Myr^{-1})
		Low-Latitude Records	
ODP 1218	32.04 ± 0.32	0.23 ± 0.10	-0.06 ± 0.24
		High-Latitude Records	
DSDP 522	32.14 ± 0.17	0.44 ± 0.08	-0.20 ± 0.13
ODP 689	32.58 ± 0.52	0.33 ± 3.50	$+0.03 \pm 2.09$
ODP 744	32.99 ± 0.13	0.70 ± 0.26	-0.00 ± 0.03
ODP 748	32.14 ± 0.20	0.44 ± 0.12	-0.23 ± 0.11
Average[c]	$32.52^{\pm 0.24}_{\pm 0.11}$	$0.46^{\pm 0.04}_{\pm 0.07}$	$-0.03^{\pm 0.04}_{\pm 0.03}$

[a] Values are rounded.

[b] Negative and positive slopes indicate glaciation/cooling and deglaciation/warming, respectively.

[c] Weighted average with external error (superscript) and internal error (subscript); time average includes dating-error effects. Slope is given by amplitude/duration; dating-error effects via duration on slope are negligible against amplitude-error effects.

Table 10. Results[a] Oligocene Swinging Trends (O-Swings), Late Part (cf. Figure 10)

Record	Age (Ma)	Slope[b], Start (‰ Myr^{-1})	Slope[b], End (‰ Myr^{-1})
		Low-Latitude Records	
DSDP 77	25.98 ± 0.77	-0.10 ± 0.03	$+0.27 \pm 0.25$
DSDP 366	28.45 ± 0.51	-0.11 ± 0.04	$+0.13 \pm 0.07$
DSDP 574	29.85 ± 1.15	-0.22 ± 0.25	$+0.08 \pm 0.08$
ODP 667	28.23 ± 1.46	-0.13 ± 2.70	$+0.06 \pm 0.94$
ODP 803	24.68 ± 2.74	-0.08 ± 1.01	$+0.45 \pm 0.48$
ODP 1218	26.92 ± 0.22	-0.07 ± 0.01	$+0.19 \pm 0.03$
Average[c]	$27.19^{\pm 0.37}_{\pm 0.21}$	$-0.07^{\pm 0.01}_{\pm 0.01}$	$+0.17^{\pm 0.02}_{\pm 0.02}$
		High-Latitude Records	
DSDP 522	29.33 ± 1.54	$+0.16 \pm 3.56$	$+0.03 \pm 0.43$
DSDP 529	24.96 ± 2.13	-0.04 ± 6.04	$+0.73 \pm 1.00$
ODP 689	27.56 ± 0.77	-0.09 ± 4.31	$+0.07 \pm 0.06$
ODP 690	28.77 ± 2.12	-0.13 ± 0.69	-0.02 ± 0.39
ODP 703	26.58 ± 1.11	-0.07 ± 0.08	$+0.17 \pm 0.21$
ODP 744	28.34 ± 0.37	-0.14 ± 0.03	$+0.16 \pm 0.02$
ODP 748	26.67 ± 2.04	-0.04 ± 0.37	$+0.08 \pm 0.15$
Average[c]	$28.01^{\pm 0.31}_{\pm 0.31}$	$-0.13^{\pm 0.01}_{\pm 0.03}$	$+0.15^{\pm 0.01}_{\pm 0.02}$

[a] Values are rounded.

[b] Negative and positive slopes indicate glaciation/cooling and deglaciation/warming, respectively.

[c] Weighted average with external error (superscript) and internal error (subscript); time averages include dating-error effects. Slope is given by amplitude/duration; dating-error effects via duration on slope are negligible against amplitude-error effects.

Table 11. Results[a] Oligocene–Miocene Boundary (OMB) (cf. Figure 11)

Record	Start (Ma)	End (Ma)	Duration (Myr)	Midpoint (Ma)	δ^{18}O Amplitude[b] (‰)
			Low-Latitude Records		
DSDP 366	23.46 ± 0.08	22.72 ± 0.03	0.74 ± 0.08	23.09 ± 0.04	-0.59 ± 0.06
ODP 667	23.12 ± 0.18	22.97 ± 0.11	0.15 ± 0.27	23.04 ± 0.07	-0.47 ± 0.07
ODP 803	23.19 ± 0.15	23.00 ± 0.10	0.18 ± 0.22	23.10 ± 0.07	-0.52 ± 0.09
ODP 926	23.28 ± 0.02	23.06 ± 0.03	0.22 ± 0.04	23.17 ± 0.01	-0.67 ± 0.05
ODP 929	23.12 ± 0.04	22.91 ± 0.04	0.20 ± 0.07	23.01 ± 0.02	-0.82 ± 0.08
ODP 1218	23.23 ± 0.04	23.08 ± 0.04	0.14 ± 0.07	23.16 ± 0.02	-0.56 ± 0.07
Average[c]	$23.24^{\pm 0.05}_{\pm 0.05}$	$22.95^{\pm 0.06}_{\pm 0.05}$	$0.27^{\pm 0.08}_{\pm 0.03}$	$23.10^{\pm 0.03}_{\pm 0.04}$	$-0.61^{\pm 0.05}_{\pm 0.03}$
			High-Latitude Records		
DSDP 522	23.42 ± 0.16	23.25 ± 0.14	0.17 ± 0.19	23.33 ± 0.12	-0.70 ± 0.23
DSDP 529	23.62 ± 0.10	23.45 ± 0.08	0.17 ± 0.13	23.53 ± 0.07	-0.57 ± 0.15
DSDP 563	23.68 ± 0.11	23.07 ± 0.02	0.60 ± 0.11	23.38 ± 0.06	-0.83 ± 0.09
DSDP 608	23.53 ± 0.03	23.36 ± 0.02	0.17 ± 0.03	23.44 ± 0.02	-0.51 ± 0.07
ODP 703	24.16 ± 0.18	23.50 ± 0.19	0.66 ± 0.26	23.83 ± 0.13	-0.97 ± 0.25
ODP 704	23.50 ± 0.08	23.02 ± 0.04	0.47 ± 0.09	23.26 ± 0.04	-0.79 ± 0.11
ODP 744	24.14 ± 0.07	23.98 ± 0.10	0.17 ± 0.14	24.06 ± 0.05	-0.37 ± 0.07
ODP 747	23.61 ± 0.22	22.79 ± 0.24	0.81 ± 0.37	23.20 ± 0.14	-0.54 ± 0.13
ODP 1090	23.25 ± 0.05	23.11 ± 0.05	0.14 ± 0.08	23.18 ± 0.02	-0.62 ± 0.08
Average[c]	$23.63^{\pm 0.14}_{\pm 0.06}$	$23.27^{\pm 0.10}_{\pm 0.04}$	$0.22^{\pm 0.05}_{\pm 0.03}$	$23.46^{\pm 0.10}_{\pm 0.04}$	$-0.57^{\pm 0.06}_{\pm 0.03}$

[a] Values are rounded.

[b] Negative and positive amplitudes indicate glaciation/cooling and deglaciation/warming, respectively.

[c] Weighted average with external error (superscript) and internal error (subscript); start, end, and midpoint averages include dating-error effects.

Table 12. Results[a] Climate Transition MMCO-Start (cf. Figure 12)

Record	Start (Ma)	End (Ma)	Duration (Myr)	Midpoint (Ma)	δ^{18}O Amplitude[b] (‰)
			Low-Latitude Records		
DSDP 289	17.05 ± 1.02	16.92 ± 0.95	0.14 ± 0.64	16.98 ± 0.93	$+0.23 \pm 0.14$
DSDP 317	17.01 ± 1.18	16.76 ± 0.77	0.24 ± 0.91	16.89 ± 0.88	$+0.19 \pm 0.14$
DSDP 366	18.93 ± 0.94	18.77 ± 0.86	0.16 ± 1.02	18.85 ± 0.74	$+0.22 \pm 0.11$
ODP 667	17.26 ± 1.25	16.92 ± 0.88	0.35 ± 1.02	17.09 ± 0.95	$+0.19 \pm 0.14$
Average[c]	$17.70^{\pm 0.50}_{\pm 0.54}$	$17.33^{\pm 0.48}_{\pm 0.43}$	$0.20^{\pm 0.05}_{\pm 0.42}$	$17.62^{\pm 0.51}_{\pm 0.43}$	$+0.21^{\pm 0.01}_{\pm 0.07}$
			High-Latitude Records		
DSDP 563	17.92 ± 0.86	16.58 ± 0.73	1.34 ± 1.04	17.25 ± 0.60	$+0.33 \pm 0.10$
DSDP 608	17.19 ± 0.90	16.99 ± 0.84	0.20 ± 0.69	17.09 ± 0.80	$+0.28 \pm 0.10$
ODP 704	20.03 ± 1.10	16.46 ± 0.94	3.56 ± 1.68	18.24 ± 0.58	$+0.36 \pm 0.09$
ODP 744	17.79 ± 0.38	17.14 ± 0.28	0.65 ± 0.59	17.47 ± 0.16	$+0.64 \pm 0.11$
ODP 1090	16.78 ± 0.30	16.75 ± 0.24	0.03 ± 0.47	16.76 ± 0.14	$+0.33 \pm 0.06$
Average[c]	$17.35^{\pm 0.37}_{\pm 0.23}$	$16.89^{\pm 0.11}_{\pm 0.18}$	$0.46^{\pm 0.35}_{\pm 0.30}$	$17.15^{\pm 0.20}_{\pm 0.12}$	$+0.37^{\pm 0.05}_{\pm 0.04}$

[a] Values are rounded.

[b] Negative and positive amplitudes indicate glaciation/cooling and deglaciation/warming, respectively.

[c] Weighted average with external error (superscript) and internal error (subscript); start, end, and midpoint averages include dating-error effects.

Table 13. Results[a], Middle Miocene Climate Transition (MMCT) (cf. Figure 13)

Record	Start (Ma)	End (Ma)	Duration (Myr)	Midpoint (Ma)	δ^{18}O Amplitude[b] (‰)
Low-Latitude Records					
DSDP 77	16.20 ± 0.81	12.37 ± 0.84	3.84 ± 1.47	14.28 ± 0.38	-1.19 ± 0.13
DSDP 289	15.19 ± 0.36	11.99 ± 0.35	3.20 ± 0.62	13.59 ± 0.17	-0.93 ± 0.07
DSDP 317	13.93 ± 0.70	13.78 ± 0.34	0.15 ± 0.98	13.85 ± 0.25	-0.65 ± 0.07
DSDP 366	14.27 ± 0.89	14.13 ± 0.88	0.14 ± 1.40	14.20 ± 0.54	-0.62 ± 0.17
DSDP 574	14.67 ± 0.20	12.57 ± 0.16	2.10 ± 0.31	13.62 ± 0.09	-1.00 ± 0.04
ODP 667	13.78 ± 0.32	13.74 ± 0.22	0.04 ± 0.40	13.76 ± 0.18	-0.55 ± 0.09
ODP 806	15.23 ± 0.61	12.91 ± 0.44	2.32 ± 0.91	14.07 ± 0.28	-0.98 ± 0.13
ODP 926	14.77 ± 0.48	13.81 ± 0.30	0.95 ± 0.59	14.29 ± 0.27	-0.77 ± 0.06
Average[c]	$14.62^{\pm 0.21}_{\pm 0.14}$	$13.08^{\pm 0.25}_{\pm 0.11}$	$1.49^{\pm 0.42}_{\pm 0.20}$	$13.79^{\pm 0.09}_{\pm 0.08}$	$-0.85^{\pm 0.06}_{\pm 0.03}$
High-Latitude Records					
DSDP 281	15.18 ± 0.03	15.17 ± 0.05	0.01 ± 0.08	15.17 ± 0.01	-0.79 ± 0.07
DSDP 357	14.91 ± 0.75	13.01 ± 0.73	1.90 ± 1.27	13.96 ± 0.39	-0.77 ± 0.13
DSDP 516	15.49 ± 0.20	14.07 ± 0.24	1.43 ± 0.36	14.78 ± 0.13	-1.19 ± 0.13
DSDP 555	13.64 ± 0.28	13.35 ± 0.18	0.29 ± 0.40	13.49 ± 0.12	-0.81 ± 0.07
DSDP 563	14.68 ± 0.50	12.81 ± 0.38	1.86 ± 0.78	13.75 ± 0.21	-0.68 ± 0.05
DSDP 608	14.53 ± 0.41	12.88 ± 0.38	1.65 ± 0.71	13.71 ± 0.17	-0.88 ± 0.06
ODP 744	14.31 ± 0.52	12.13 ± 0.67	2.18 ± 1.00	13.22 ± 0.33	-0.99 ± 0.09
ODP 747	14.78 ± 0.26	12.70 ± 0.23	2.08 ± 0.42	13.74 ± 0.12	-1.15 ± 0.07
ODP 1171	14.69 ± 0.12	12.78 ± 0.15	1.91 ± 0.23	13.73 ± 0.07	-1.02 ± 0.05
Average[c]	$14.94^{\pm 0.15}_{\pm 0.07}$	$13.99^{\pm 0.39}_{\pm 0.07}$	$0.36^{\pm 0.25}_{\pm 0.07}$	$14.22^{\pm 0.25}_{\pm 0.05}$	$-0.90^{\pm 0.06}_{\pm 0.02}$

[a] Values are rounded.

[b] Negative and positive amplitudes indicate glaciation/cooling and deglaciation/warming, respectively.

[c] Weighted average with external error (superscript) and internal error (subscript); start, end, and midpoint averages include dating-error effects.

Table 14. Results[a] Climate Transition 4-to-10-Ma (cf. Figure 14)

Record	Slope[b] (‰ Myr^{-1})
Low-Latitude Records	
DSDP 77	-0.046 ± 0.052
DSDP 289	-0.099 ± 0.032
ODP 667	-0.070 ± 0.059
ODP 806	$+0.021 \pm 0.017$
ODP 926	-0.039 ± 0.007
Average[c]	$-0.033^{\pm 0.013}_{\pm 0.006}$
High-Latitude Records	
DSDP 334	-0.085 ± 0.025
DSDP 360	-0.075 ± 0.016
DSDP 397	-0.062 ± 0.037
DSDP 410	-0.112 ± 0.038
DSDP 525	-0.082 ± 0.034
DSDP 552	-0.035 ± 0.009
DSDP 553	-0.028 ± 0.007
DSDP 555	$+0.011 \pm 0.046$
DSDP 608	-0.070 ± 0.011
ODP 704	$+0.005 \pm 0.010$
ODP 747	-0.103 ± 0.013
ODP 1088	$+0.019 \pm 0.022$
Average[c]	$-0.040^{\pm 0.010}_{\pm 0.004}$

[a] Values are rounded.

[b] Negative and positive slopes indicate glaciation/cooling and deglaciation/warming, respectively.

[c] Weighted average with external error (superscript) and internal error (subscript). Slope is given by amplitude/duration; dating-error effects via duration on slope are negligible against amplitude-error effects.

Table 15. Rates of Change[a] of Cenozoic Climate Transitions

Transition	Glaciation/Cooling (‰ Myr^{-1})	Deglaciation/Warming (‰ Myr^{-1})
PE-Trend[b]		$+0.157^{\pm0.016}_{\pm0.018}$
PETM[c]	$-1.465^{\pm0.646}_{\pm0.223}$	$+1.687^{\pm0.776}_{\pm0.262}$
LTEC-I[d]	$-0.166^{\pm0.014}_{\pm0.013}$	
LTEC-II[e]	$-0.415^{\pm0.058}_{\pm0.074}$	
EOT[f]	$-1.874^{\pm0.296}_{\pm0.205}$	
EOT recovery[g]		$+0.520 \pm 0.223$
OMB[h]	$-1.058^{\pm0.163}_{\pm0.097}$	
MMCO-Start[i]		$+0.114^{\pm0.024}_{\pm0.052}$
MMCT[j]	$-0.432^{\pm0.031}_{\pm0.032}$	

[a] Values are rounded; weighted averages of amplitude/duration with external error (superscript) and internal error (subscript). Negative and positive rates indicate glaciation/cooling and deglaciation/warming, respectively.

[b] Table 4.

[c] Table 5.

[d] Table 6.

[e] Table 7.

[f] Table 8.

[g] Section 4.1.3.1; only one record (ODP 1218).

[h] Table 11.

[i] Table 12.

[j] Table 13.